

INFORMATION TO USERS

This manuscript has been reproduced from the microfilm master. UMI films the text directly from the original or copy submitted. Thus, some thesis and dissertation copies are in typewriter face, while others may be from any type of computer printer.

The quality of this reproduction is dependent upon the quality of the copy submitted. Broken or indistinct print, colored or poor quality illustrations and photographs, print bleedthrough, substandard margins, and improper alignment can adversely affect reproduction.

In the unlikely event that the author did not send UMI a complete manuscript and there are missing pages, these will be noted. Also, if unauthorized copyright material had to be removed, a note will indicate the deletion.

Oversize materials (e.g., maps, drawings, charts) are reproduced by sectioning the original, beginning at the upper left-hand corner and continuing from left to right in equal sections with small overlaps. Each original is also photographed in one exposure and is included in reduced form at the back of the book.

Photographs included in the original manuscript have been reproduced xerographically in this copy. Higher quality 6" x 9" black and white photographic prints are available for any photographs or illustrations appearing in this copy for an additional charge. Contact UMI directly to order.



University Microfilms International
A Bell & Howells Information Company
300 North Zeeb Road Ann Arbor MI 48106-1346 USA
313 761-4700 800 521-0600

Order Number 9136723

Nanocrystalline Cu-Ta composites

Savage, Howard Scott, Ph.D.

University of Illinois at Urbana-Champaign, 1991

Copyright ©1991 by Savage, Howard Scott. All rights reserved.

U·M·I
300 N. Zeeb Rd.
Ann Arbor, MI 48106

NANOCRYSTALLINE Cu-Ta COMPOSITES

BY

HOWARD SCOTT SAVAGE

B.S., University of Illinois at Urbana-Champaign, 1984
M.S., University of Illinois at Urbana-Champaign, 1988

THESIS

Submitted in partial fulfillment of the requirements
for the degree of Doctor of Philosophy in Metallurgical Engineering
in the Graduate College of the
University of Illinois at Urbana-Champaign, 1991

Urbana, Illinois

UNIVERSITY OF ILLINOIS AT URBANA-CHAMPAIGN

THE GRADUATE COLLEGE

MARCH 1991

WE HEREBY RECOMMEND THAT THE THESIS BY

HOWARD SCOTT SAVAGE

NANOCRYSTALLINE Cu-Ta COMPOSITES
ENTITLED

BE ACCEPTED IN PARTIAL FULFILLMENT OF THE REQUIREMENTS FOR
DOCTOR OF PHILOSOPHY
THE DEGREE OF

J. M. Rigsbee

Director of Thesis Research

J. Economy

Head of Department

Committee on Final Examination†

J. M. Rigsbee

Chairperson

Paul Attalitter

James H Shabotins

Haydn Chen

† Required for doctor's degree but not for master's.

© Copyright by Howard Scott Savage, 1991

ABSTRACT

This research investigated the physical metallurgy, high temperature coarsening, and processing/structure relationships for Cu_{1-x}Ta_x ($x = \sim 5$ to 20 atomic percent) alloys. These metastable alloys were produced using a plasma assisted physical vapor deposition (PAPVD) process which allowed ion bombardment during alloy deposition. Techniques used for structural and chemical analyses of these alloys include: transmission and scanning electron microscopy, energy dispersive x-ray analysis, x-ray diffraction, microhardness, and sheet resistance. PAPVD processing parameters varied in this study included: ion bombardment, ion to depositing atom ratio, deposition rate, and alloy composition. Thermal processing variations included: annealing at 800 C for up to 100 hours and at 900 C for up to 10 hours and hot isostatic pressing (HIP) at 900 C for 1 hour and 172 MPa.

This research successfully demonstrated that physical vapor deposition processes can "design" the microstructures of metastable Cu_{1-x}Ta_x alloys at the near atomic scale. These alloys consist of an essentially pure Cu matrix with a dispersion of discrete, nanoscale second phase particles. For as-deposited alloys: 1) the Cu matrix morphology was dependent on Ta content and ion bombardment and the film densities increased with decreasing Ta content and increasing ion bombardment and 2) the second phase particles consisted of bcc Ta, fcc Ta, and Ta oxide, the particle size was dependent on Ta content and ion bombardment, and the particles were mainly smaller than 10 nm. For annealed alloys: 1) annealing at 900 C for 10 hours altered only slightly the matrix morphology and showed that the second phase particles are effective at pinning Cu grain boundaries, consistent with the predictions of the Zener model; 2) the second phase particles remained bcc Ta, fcc Ta, and Ta oxide, with sizes still <10 nm; 3) oxygen incorporation into the growing coating stabilized the annealed particle sizes; 4) the matrix and second phase morphologies in HIPped alloys coarsened more in regions which underwent greater plastic strains; and, 5) Ta particle coarsening occurred by the Ostwald mechanism (annealed alloys) as well as collisional coalescence (HIPped alloys).

ACKNOWLEDGEMENT

The author would like to express his gratitude to some of the many people who made this work possible. The author wishes to thank Professor J. M. Rigsbee for his guidance, support, friendship, and the opportunities to explore metallurgy beyond the confines of the thesis topic. The effort of the members of the thesis defense committee (C. J. Altstetter, H. H. Chen, and J. F. Stubbins) is greatly appreciated. Thanks are due to the current and past members of JMR's research group. The U. S. Army Construction Engineering Research Laboratory is acknowledged for their ion plating facility, with special thanks to Mr. V. F. Hock, Mr. R. McCormack, and Dr. W. J. Croisant for their support at USACERL. The Center for Microanalysis of Materials at the University of Illinois is acknowledged for access to their facilities and personnel. The assistance of Mr. John Woodhouse and Mr. Alex Greene is greatly appreciated. Thanks to the faculty, students, and staff of the University of Illinois. Special thanks to my family and friends for their encouragement. The financial support for this research program has been partially provided through the Army Research Office.

TABLE OF CONTENTS

I.	INTRODUCTION	1
II.	BACKGROUND	2
	II.A. COPPER	2
	II.B. TANTALUM	4
	II.C. COMPOSITES	5
	II.D. NANOSCALE MATERIALS	7
	II.E. ION PLATING	8
	II.F. DISPERSION HARDENING	11
	II.G. COARSENING KINETICS OF SECOND PHASE PARTICLES	16
III.	EXPERIMENTAL PROCEDURE	24
	III.A. SPECIMEN PREPARATION	25
	III.B. ANALYTICAL PROCEDURE	28
	III.C. COMPUTER MODELING	31
IV.	RESULTS	37
	IV.A. COATING CHEMISTRY	37
	IV.B. SEM ANALYSES OF COATING MORPHOLOGIES	40
	IV.C. TEM ANALYSES AND PHASE IDENTIFICATION	48
	IV.D. X-RAY DIFFRACTION	80
	IV.E. MICROHARDNESS	87
	IV.F. SHEET RESISTANCE	88
	IV.G. COMPUTER MODELING	88
V.	DISCUSSION OF RESULTS	93
	V.A. ION BOMBARDMENT INDUCED MORPHOLOGY CHANGES	93
	V.B. DEPENDENCE OF SECOND PHASE COARSENING ON MATRIX MORPHOLOGY	99
	V.C. COARSENING MECHANISMS	102
	V.D. VARIATION OF COMPOSITION WITH SUBSTRATE POSITION	105

V.E.	MICROSTRUCTURAL VARIATION WITH COMPOSITION	109
V.F.	MICROSTRUCTURAL RESPONSE TO HEAT TREATMENT	109
V.G.	MICROSTRUCTURAL RESPONSE TO CONSOLIDATION BY HIP	111
V.H.	COMPOSITIONAL SHIFT DUE TO ION BOMBARDMENT	113
V.I.	COMPOSITIONAL INFLUENCE ON COARSENING	114
V.J.	INFLUENCE OF BIAS ON TANTALUM SOLUBILITY	115
V.K.	MECHANICAL PROPERTIES	116
V.L.	STABILITY OF FCC TANTALUM	116
VI.	CONCLUSIONS	117
	APPENDIX	119
	DEPOSITION DATA AND SPANNING COMPOSITIONS	119
	X-RAY DIFFRACTION SCANS	123
	POWDER FILE DATA	150
	COMPUTER PROGRAMS	154
	KINETIC DATA	161
	REFERENCES	163
	VITA	168

I. INTRODUCTION

The research presented in this thesis is an investigation into the physical metallurgy and high temperature coarsening behavior of non-equilibrium Cu_{1-x}Ta_x alloys. These alloys were produced by plasma assisted physical vapor deposition (PAPVD) which allows atomic scale "engineering" of a material's chemistry and structure without the thermodynamic constraints (e.g., solubility limits) usually encountered with solidification processes. Cu-Ta was selected as a model system for this study because of very low mutual solid solubilities and because the face-centered-cubic and body-centered-cubic crystal structures offer the possibility of partial interfacial coherency. The objectives of this study were (1) to determine whether a dispersion of nanoscale Ta particles could be produced in a Cu matrix and (2) to develop an understanding of the coarsening behavior of such a dispersion of the nanoscale Ta particles. From a practical viewpoint, such a dispersion of partially coherent, low-solubility, nanoscale Ta particles in a Cu matrix should provide excellent dispersion strengthening with high resistance to coarsening.

Basic questions which this research addresses include:

- 1) Can a nanoscale dispersion of Ta particles be produced in Cu-Ta alloys using plasma assisted physical vapor deposition (PAPVD)?
- 2) What are the basic structures and phase distributions in PAPVD Cu-Ta alloys?
- 3) What are the effects of the matrix and second phase particle morphologies on coarsening?
- 4) What are the effects of plastic deformation at elevated temperatures (i.e., hot isostatic pressing) on the morphologies of the matrix and second phase?
- 5) By which mechanism(s), diffusional Ostwald ripening or collision and sintering, do the second phase particles coarsen?
- 6) How do the alloy deposition parameters, such as ion bombardment, influence the film morphology and coarsening behavior?

II. BACKGROUND

Recently there has been an interest in developing Cu-based materials with combinations of high strength and high thermal/electrical conductivities for high temperature use. Applications of such materials could include rocket engines (combustor liners), rail guns (gun rails, homopolar generators, inductors), particle beam systems (electromagnets, conductors), and the National Aerospace Plane (engines, aerosurfaces) [1]. Conventional Cu alloys are limited in their ability to meet the performance requirements of the above applications for the following reasons: 1) rapid coarsening and strength loss will occur for precipitation strengthened alloys at the required elevated use temperatures; and, 2) extensive solid solution alloying will have very detrimental effects on the conductivities. These limitations of conventional Cu alloys have led to an interest in the development of advanced Cu-based composites.

This background section reviews the following topics relevant to this thesis: 1) properties of Cu and Cu alloys; 2) properties of Ta; 3) Cu-refactory metal composite materials; 4) synthesis of nanoscale materials; 5) ion plating and plasma assisted physical vapor deposition; 6) dispersion hardening theories; and, 7) coarsening kinetics of second phase particles. Details of these topics, including additional references, are developed as appropriate in the discussion section.

II.A. COPPER

Cu has a face centered cubic (fcc) crystal structure, a density of 8.96 g/cc, a melting point of 1083 Celsius, a boiling point of 2567 Celsius, and is second only to silver in electrical conductivity [2]. The yield strength of annealed pure Cu is about 70 MPa and can be increased to about 360 MPa through cold working [3]. Use of pure Cu at elevated temperatures is limited by its tendency to lose strength due to recovery and recrystallization. The minimum recrystallization temperature, about 200 Celsius, is dependent on purity and degree of cold work [3, 4]. As discussed by Brick, Pense and Gordon: 1) Recrystallization starts at a lower

temperature and is completed within a narrower temperature range for greater prior deformation, a finer prior grain size, a purer metal, and a longer time of annealing. 2) The recrystallized grain size will be smaller for a lower annealing temperature (above the minimum required for recrystallization), for a shorter time at temperature, for a shorter time of heating to temperature, for a heavier prior reduction, and for a larger volume fraction or finer dispersion of insoluble particles.

Cu-based alloys achieve strengthening by cold working, solid solution strengthening, precipitation hardening, and dispersions of insoluble particles. Solid solution strengthened Cu alloys (e.g., brasses (Zn), bronzes (Sn, Al, and Si), and Cu nickels) may have yield strengths of 800 MPa or higher (C63800 (95Cu-2.8Al-1.8Si-0.4Co) [3]. The addition of solid solution elements is often highly detrimental to the conductivity of the alloy (C63800 has about 10% of the electrical conductivity of pure Cu) [3-5]. A good example of solid solution strengthening without damaging conductivity is silver-bearing Cu [3-5]. In this case, room temperature strength is improved only marginally over pure Cu; but the annealing temperature is increased with increasing silver content (silver free, about 280 C; 0.044 Ag, about 350 C; and, 0.114 Ag, about 392 C) [3, 4].

As an example of a precipitation hardening wrought Cu alloy, C18200 (99Cu-1Cr) is solution heat treated for 20 min at 1000 C, water quenched, and aged for 4 hours at 450 to give yield strengths of about 450 MPa and conductivities of about 80% of pure Cu [3]. Zr (C15000, anneal 1 hr at 650 C, age 1 hr at 550 C) and Be (C17200, anneal 1 hr at 790 C, age 1 hr at 425 C) are also used for precipitation hardening [3]. It is clear from this data that the usefulness of these high strength Cu-based alloys would be very limited for temperatures exceeding 550 C.

C15735 (99.3Cu-0.7Al₂O₃), a dispersion hardened wrought Cu alloy made by consolidation of internally oxidized alloy powder, loses its cold worked strength when it is exposed to a temperatures above 650 C. This medium strength alloy is attractive because its low solid solution strengthening level allows it to retain 85% of the electrical conductivity of

pure Cu [3]. Of the Cu-based alloys discussed in this subsection, C15735 would be the least affected by elevated temperatures but this alloy is still not suitable for long term exposure to temperatures exceeding 600 C.

II.B. TANTALUM.

Pure Ta has a body centered cubic (bcc) crystal structure, a density of 16.6 g/cc, a melting point of 2996 Celsius, a boiling point of 5427 C, an electrical conductivity 13% that of Cu, a thermal expansion coefficient (6.5 $\mu\text{m}/\text{m}/\text{K}$ near 20 C) 39% that of Cu (16.5 $\mu\text{m}/\text{m}/\text{K}$ near 20 C), and a thermal conductivity (54.4 W/m/K at 20 C) 14% that of Cu (398 W/m/K at 27 C) [3]. Pure Ta is very ductile (it reduced 95% between anneals); the yield and ultimate tensile strengths are increased and ductility is decreased with increasing interstitial content (oxygen, nitrogen, carbon, and hydrogen) [3]. Although the recrystallization of pure Ta occurs at temperatures above 1000 C, above 300 C it oxidizes in air and is therefore unsuitable for high temperature use in oxidizing environments [3, 4]. The solubility of oxygen in Ta decreases from 5.1 at. percent at 1500 C to 3 at. percent at 1100 C and less than that at lower temperatures. The equilibrium Ta oxide is alpha Ta_2O_5 which occurs at temperatures below 1550 C [6]. Work by Terao [7] indicates that nonequilibrium oxides form when Ta powder is heated in oxygen.

Although detailed diffusivity and phase diagram information are not available, it is well known that Ta and Cu have very limited mutual solubilities. Butrymowicz, Manning, and Read [8] have stated that "The very limited mutual solubility of this system and the disparity in melting points has discouraged diffusion experiments, although the joining of Ta to Cu has been the subject of several attempts to fabricate composite materials for nose-cone applications." The activation energy and frequency factor (D_0) for self diffusion in Ta are 98.7 Kcal/mole and 1.24 cm^2/sec , respectively. For comparison, the same data for self diffusion in Cu are 50.5 Kcal/mole and 0.78 cm^2/sec [8].

Thin, vapor deposited films of bcc metals have been observed to have fcc structures when deposited at low temperatures [9-11]. Fcc Ta films have been observed for thicknesses on the order of 50 nm and substrate temperatures during deposition up to 400 C. [10, 11].

II.C. COMPOSITES

The strength deficiency of conventionally strengthened Cu-based alloys at elevated temperatures has led to an interest in the development of Cu matrix-refractory metal composites combining the high thermal and electrical conductivity, toughness, and thermal shock resistance of a Cu matrix with high temperature strength. Composites achieve strength and toughness from several factors: The simple rule of mixtures strengthening mechanism assumes that the strain in the matrix is the same as the strain in the strengthening phase (no discontinuities at the interface) so that the strength of the composite is given summing the strengths of the components weighted by their respective volume fractions. Toughening in composites is often attributed to a mechanism involving crack blunting; that is, a crack in a brittle strengthening phase may be arrested by localized plastic deformation at the interface of the matrix/strengthening phase. In this way, the failure of a few individual pieces of the strengthening phase does not mean failure of the entire composite. Strengthening may also occur by a Hall-Petch mechanism where strengthening of the matrix and/or strengthening phase arises due to pinning of grain boundaries at the interphase boundaries. This results in matrix grain sizes on the order of the strengthening phase spacing and a strengthening phase grain size on the order of the strengthening phase dimension. In most ordinary composites Hall-Petch strengthening is not significant because the strengthening phase spacing is equal to or larger than the grain size for the conventionally processed matrix. However, in cases where the strengthening phase spacing is very small, as in ultrafine (nanoscale) microcomposites which may have strengthening phase spacings below 100 nm, Hall-Petch strengthening becomes significant and results in strengths above that predicted by the rule of mixtures [1, 12]. Stabilization of matrix grain size by a dispersion of second phase particles, an added

strengthening benefit, is described by the Zener model [13] as discussed in a later section of this background.

Examples of Cu-refractory metal composites include: 1) Cu infiltrated composites fabricated by presintering compacts of Cr, Fe, Mo, or W powders to form a refractory skeleton with continuous porosity and then infiltrating the skeleton with Cu to fill the porosity. The infiltrated composites have elevated temperature strength due to the support given by the refractory metal skeleton; good conductivity due to the presence of Cu and the low refractory metal solubility in Cu; and, resistance to melting by an electrical arc due to the refractory metal skeleton [14]. 2) Refractory oxide composites such as those produced by controlled internal oxidation of Cu-Al alloy powders are strengthened by a dispersion of very fine (less than 10 nm) alumina particles [3, 15]. 3) Filament wound composites which are strengthened by refractory fibers (e.g., W) at elevated temperatures [16]. These composites may be produced by thermally spraying Cu continuously over refractory metal filaments which are themselves continuously wound around a mandrel. The final composite is then hot isostatic pressed to full density and the mandrel is then removed. 4) In-situ, ultrafine nanoscale composites are produced by co-arccasting Cu and an insoluble refractory metal into a water cooled crucible to form fine dendrites of the refractory metal in a Cu matrix. Heavy deformation of the as-cast ingot (true strain of 10 or more) transforms the refractory metal dendrites into filaments, normally with submicron scale widths and spacings. The in-situ composite strengths start near the rule of mixtures values, in the as cast form, and increase with processing strain to eventually approach the theoretical strength of Cu. The strength of the in-situ composites has been attributed to Hall-Petch strengthening of the Cu matrix, whisker-like behavior of the filaments, and densely spaced interfaces (less than 100 nm spacing) which inhibit dynamic recovery of the Cu matrix) [1, 12].

II.D. NANOSCALE MATERIALS

From the above discussion it is evident that there are benefits to producing composites with nanoscale (<100 nm) strengthening particles and nanoscale spacings between the particles. There exists currently considerable interest in the preparation and characterization of materials with nanoscale microstructures because results suggest that significant beneficial changes in the properties of materials may be realized [17]. The preparation and properties of materials with nanoscale structures have recently (1989) been reviewed in a report by the National Material Advisory Board Committee on Materials with Submicron-Sized Microstructures [17]. Examples of methods for the synthesis of nanoscale structures include:

- 1) Molecular synthesis of polymers with controlled structure and chain lengths.
- 2) Reductive pyrolysis of cobalt-tungsten salts in hydrogen to form a Co-W nanocomposite which can be further processed in a controlled carbon-activity environment to form ultrafine WC in a Co matrix.
- 3) Sol-gel processing of organometallic precursors to form nanocrystalline ceramics including aerogels and infiltration of porous sol-gel ceramics to form composites.
- 4) Laser pyrolysis of mixed gases to form ultrafine powders.
- 5) Colloidal synthesis for processing of ceramics with submicron structures.
- 6) Reactive sputtering of multilayer thin films.
- 7) Cryochemical synthesis of metal or ceramic powders which involves flash freezing of a solution containing the cations of interest, sublimation of the solvent, and conversion to the desired product.
- 8) Chemical vapor synthesis of oxides from volatile metal chlorides or fluorides using flame or plasma torch reactors.
- 9) Ion beam processing to produce near surface nanoscale microstructures by implantation and/or mixing.
- 10) Mechanical processing as described above for the in-situ composites.
- 11) Gas condensation synthesis of ultrafine metal powders in an inert gas atmosphere.
- 12) Rapid solidification processing to form ultrafine microstructures by rapid quenching from the molten state.

Morphologies reviewed in [17] include: filamentary structures, multilayer structures, dispersed phase structures, macromolecular composite structures, heterogeneous nanocomposites, high surface area materials, and membranes.

Properties of nanophase materials reviewed in [17] include: magnetic properties, densification

and sintering, diffusion and solid state reactions, mechanical properties (elastic, plastic, supermodulus effect, brittle to ductile transitions), catalytic properties, and microstructural stability. Application areas for nanophase materials reviewed in [17] include: electroceramics, ultrastructured ceramics, permanent magnets, polymer-silica microcomposites, catalysts, cermets, and multilayer coatings.

Regarding nanocrystalline Cu, work by Ganapathi and co-workers [18] on nanocrystalline Cu particles prepared by sliding wear and by inert gas condensation indicates that the grain boundary structures in the nanocrystalline material as observed using transmission electron microscopy are similar to those observed in materials with larger grain sizes. Mechanical properties, as evaluated by a nanoindenter (nanoscale microhardness testing), are also consistent with those expected from polycrystalline Cu with a fine grain size. As discussed in an earlier section, the nanocrystalline Cu in the in-situ composites is strengthened in accordance to the Hall-Petch relation [1, 12].

In the present work, we concentrate on physical vapor deposition as a method of producing a dispersion of nanoscale particles in a fine grained Cu matrix. The nature of the physical vapor deposition process effectively provides rapid quenching, at the atomic scale, from vapor to solid. At low substrate temperatures, adatoms become thermally equilibrated within a few atomic distances from their point of impact thus there is the opportunity to form nonequilibrium configurations of otherwise insoluble components. Physical vapor deposition processes effectively allow a material to be chemically and structurally engineered at the atomic scale.

II.E. ION PLATING

Ion plating is a plasma-assisted physical vapor deposition process which combines elements of evaporation and sputtering to produce dense, adherent coatings of virtually any material on any substrate. Physically, energetic ions and neutrals generated by a glow discharge (plasma) strike the surface of the substrate (sputter cleaning) and growing film to

affect film nucleation, film growth, compound formation and interfacial width by enhanced adatom mobility and pseudo-diffusion associated with defect structures created by the impacting particles. We can use ion plating to produce atomic scale "alloys" of normally immiscible elements. Development of the basic ion plating process is generally credited to Mattox of Sandia Labs in the early 1960's [19]. A schematic of an ion plating system is shown in figure 1. The ion plating process involves making the substrate the cathode of a glow discharge in order to subject it to bombardment with energetic ions and neutrals which can cause sputter erosion and then exposing it to a coating vapor flux while maintaining the discharge. For coating growth to occur, it is necessary that the condensation rate of the coating vapor be greater than its sputter removal rate. Ion plating provides improved coating adhesion due to sputter removal of surface contaminants prior to deposition and physical mixing of coating and substrate atoms at the interface by ion bombardment. Coating vapor sources for the ion plating process may include metal bearing gases, magnetron sputter sources, and evaporation sources. Ion plating is typically carried out in a vacuum of several dPa (0.1 Pa = 0.75 mtorr), which is achieved by evacuating to a pressure of 1.33×10^{-4} Pa or better and then backfilling with an inert gas such as argon to the working pressure; the purpose of the backfilling is to provide adequate pressure to support the glow discharge [20]. DC substrate biases are typically on the order of several kilovolts, with substrate current densities on the order of 0.1 mA/cm^2 during sputter cleaning and coating deposition. Radio frequency (RF) substrate biases (power densities) are on the order of several tenths of a watt per square centimeter. Physically, DC and RF biases need to be sufficient to provide sputter removal of surface contaminants at a rate that is faster than they can be reformed by impinging contaminant precursors (such as oxygen, water vapor and diffusion pump oil) present in the vacuum system. The ion plating process has been extensively reviewed elsewhere [20-23]. The processes in the glow discharge have been extensively reviewed by Chapman in reference [24].

Single element film morphologies attainable by the ion plating process are essentially the same as those described by the structure zone model diagram developed by Thornton for

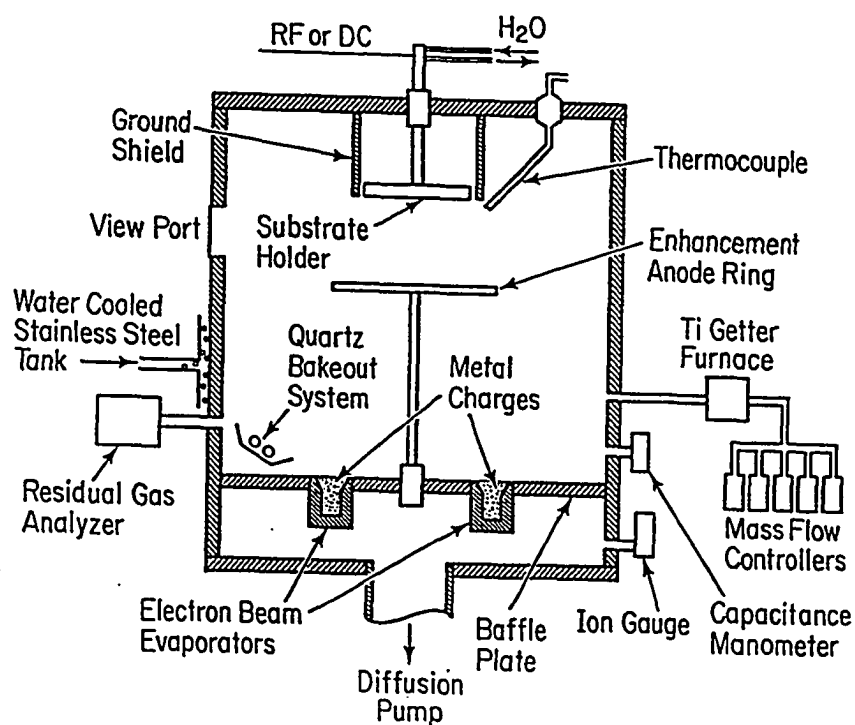


Figure 1. Schematic of the USA-CERL ion plating system.

sputter deposited coatings, figure 2 [25]. The effect of increasing substrate bias on coating structure is to generate elevated temperature structures at reduced substrate temperatures due to the effects of ion and energetic neutral bombardment on adatom mobility; more specifically, it is an increase in the ratio of bombarding ions and energetic neutrals to depositing atoms that produces the structural shift due to increased adatom mobility; this mechanism is well documented in the literature [20, 26-34]. Thickness distributions for vapor deposited films and thus the important ratio of bombarding ions to depositing atoms are dependent on system geometry and can be approximated by the well known cosine law [35-37]. The conditions present during the ion plating process may cause some deviation from the ideal cosine law due to gas scattering. This is most pronounced when the source to substrate distance exceeds the mean free path length of the support gas atoms. This gas scattering effect has been investigated and modelled by Bessaoudou, Machet, and Weissmantel [38, 39].

II.F. DISPERSION HARDENING

Dispersion hardening is produced by a finely dispersed, usually insoluble second phase produced by precipitation (as in internally oxidized Cu-alumina) or by mechanical mixing (as in thoria dispersed nickel) [40]. Strengthening of a material by a dispersion of particles arises largely from two mechanisms; the first being the barrier the particles present to dislocation motion and the second being the inhibiting effect that the particles have on matrix grain growth. Dispersion hardened materials typically have mechanical properties superior to precipitation hardened alloys at elevated temperatures due to the resistance of the dispersed phase to coarsening and their influence on grain size stability. However, at low temperatures the dispersion hardened materials are comparatively weak due to a larger particle spacing than that normally achieved by conventional precipitation hardening.

The barrier that the dispersed particles present to dislocation motion is described by the following relationship:

$$t = 2T/(I \cdot b) \quad (1)$$

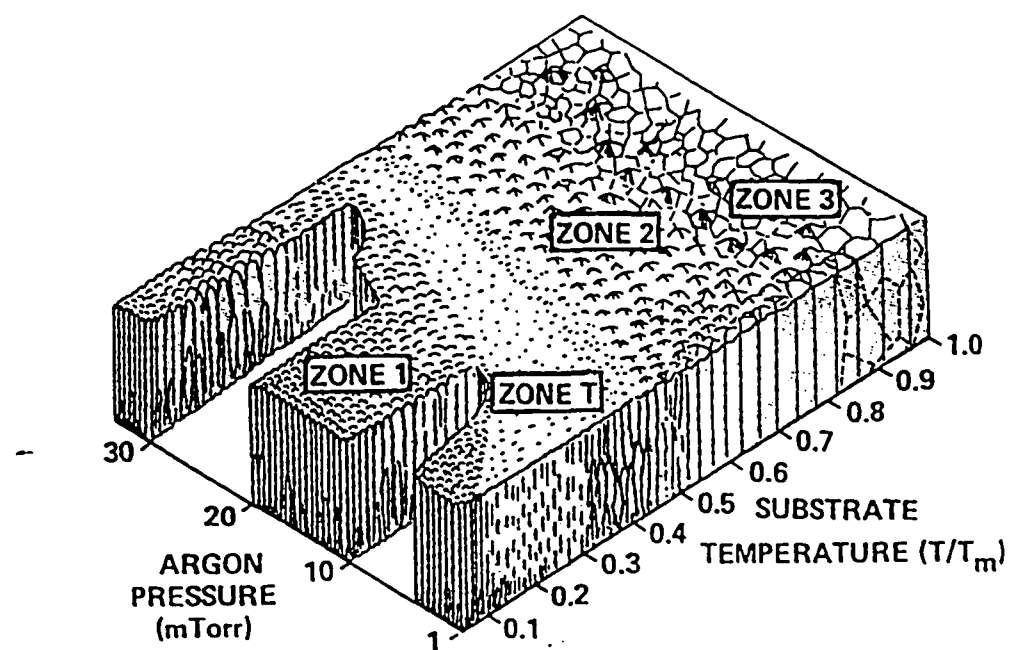


Figure 2. Schematic representation of the influence of substrate temperature and argon working pressure on the structure of metal coatings deposited by sputtering using cylindrical magnetron sources. From Thornton [25].

where t is the shear stress required to pass the obstacle, T is the dislocation line tension, I is the distance between pinning points in the slip plane, and \mathbf{b} is the Burgers vector of the dislocation. Since T and \mathbf{b} are characteristic of the slip system, the modifiable microstructural parameter is I . As indicated by the above equation, a dispersion hardened material can be strengthened by decreasing the interparticle distance. At a constant dispersed phase volume fraction, this mean that the separation distance may be reduced by reducing the size of the second phase particles. This strengthening effect may not be linear with particle size because coherency stresses, which arise when the particle/matrix interface is fully or partially coherent, effectively increase the second phase volume fraction and thereby increase the strengthening effect per unit volume fraction of second phase. Conversely, limitations in the strength of the second phase can reduce strengthening by allowing dislocations to "cut" through particles smaller than some critical size. Dislocations passing the particles may leave dislocation loops around the particles thus further reducing the effective interparticle spacing and increasing the shear stress necessary for passage of the next dislocation (Orowan strengthening). Microstructural parameters affecting dispersion hardening are briefly discussed in a later section.

The second major dispersion strengthening mechanism involves the effect of these particles for limiting grain growth. This leads to Hall-Petch [41] strengthening which is usually shown as:

$$s = s_0 + kd^{-1/2} \quad (2)$$

where s is a flow (yield) stress, k is the slope of a plot of flow stress versus square root of grain size, s_0 is the y-intercept of the plot of flow stress versus square root of grain size and d is the grain size. This is due to the limitation on the possible slip length in any given grain constrained by surrounding grains. Solving the Hall-Petch equation for C10100 Cu (oxygen free electronic Cu) with a 100 nm grain size gives a yield stress of 430 MPa (strength/grain size data for solution of the above equation was obtained from [3]). Obviously, from the Hall-Petch equation, grain growth from exposure to elevated temperature will reduce the strength of

the material. According to the Zener model, which is discussed in a later section, grain growth is limited in the presence of second phase particles which suitably interact with the grain boundaries.

Strengthening phenomena in dispersion hardened systems are very similar to those in precipitation hardening systems, with the primary difference being the origin of the second phase particles [40]. Detailed reviews of theories on particulate and polycrystalline strengthening may be found in references [40-48].

II.F.1. MICROSTRUCTURAL PARAMETERS

Critical microstructural parameters which control the strengthening effectiveness of a dispersion of particles include particle distribution, size, shape, volume fraction, particle strength, and the coherency of the particle/matrix interface. The microstructural characteristics of second phase particles and the mechanisms by which they affect plastic deformation, as summarized by Embury [47], include: 1) the particle size, which controls the dislocation by-pass mechanisms; 2) the strength of the particle/matrix interface, which controls the strain required for void nucleation; 3) the intrinsic particle strength, which determines the local stress required for particle shearing or fracture; 4) the particle shape, which controls the processes of plastic zone formation and the magnitude of the elastic back stresses; and, 5) the localized clustering of particles, which controls the strain for particle/matrix decohesion and the role of the particles in nucleation of recrystallized grains.

Particle size is of obvious importance from the previous discussion since a smaller particle size results in a larger number of particles per unit volume and thus smaller interparticle spacing for a fixed volume fraction. Strengthening increases with decreasing interparticle spacing according to equation (1) and if the smaller particles stabilize a smaller grain size, Hall-Petch strengthening occurs according to equation (2). Particle size also affects the way that the particle interacts with approaching dislocations. For example, consider individual 10 nm and 100 nm spherical particles each centered on an active slip plane for

which an available cross slip system lies at 45 degrees to the active slip plane. If glissile dislocations begin to strongly interact with particles when they get within 5 nm of the interface and cannot cut the particles, then dislocations approaching the smaller particle can cross slip around the particle while dislocations approaching the larger particle would intersect the particle.

Tensile failure for a ductile material typically occurs by nucleation, growth and coalescence of voids, which gives rise to the characteristic dimpled appearance of the fracture surface. In dispersion hardened materials, the strength of the particle/matrix interface is an important factor in controlling void nucleation. To a first approximation, a void may be nucleated when the stress locally exceeds the interfacial strength and the strain energy relieved by creating the void exceeds the energy of the newly created void surfaces [47]. The concept of local stress is important since a nonuniform distribution of particles may lead to nonuniform dislocation densities. The local stress for void nucleation may thus be exceeded even while the macroscopic stress remains lower than the critical value for interface fracture.

Similarly, a void will be nucleated if the particle fractures under the local stress. For energy considerations in this example, the newly created void surfaces would be the fracture surfaces of the particle. Intrinsic particle strength and shape will influence the conditions required for particle fracture or decohesion from the matrix. For example, comparing rod shaped and spherically shaped particles of the same volume under the same tensile stress, the rod shaped particle would generally be more susceptible to particle fracture because of its large interfacial area to volume ratio. The spherical particle would be more susceptible to void nucleation at the particle/matrix interface due to its smaller relative interfacial area.

II.F.2. ZENER MODEL FOR GRAIN SIZE

Normal grain growth in the absence of second phase particles has been shown experimentally to proceed according to the equation

$$D = kt^n \quad (3)$$

where, D is the grain dimension (diameter); k , a constant, is equal to the grain size at time = 0; t is time; and, n is an exponent with value of 0.5 for pure metals at high temperatures and <0.5 for less pure metals [41, 47-49]. The ideal exponent value of 0.5, as derived by Reed-Hill [41], simply indicates that the process is diffusion controlled and proceeds as the square root of time. The exponent value of less than 0.5 for impure metals is due to the drag that impurities and second phase particles exert on the grain boundary motion. It is generally found that those elements which distort most the lattice structure have the largest effect on grain growth [41].

According to the Zener model [13], the grain size of the matrix in a dispersion of second phase particles will be stabilized at a value, D , as given by the equation

$$D = 4r/(3f) \quad (4)$$

where r is the particle dimension (corrected for shape effects) and f is the volume fraction of the particles [47]. For example, for 40 nm Ta particles in Cu, the calculated stabilized matrix grain size at 6 atomic percent Ta is 600 nm and at 18 atomic % Ta is 212 nm; for 10 nm particles, the matrix grain sizes are reduced to 150 nm and 53 nm, respectively. The physical basis for the stabilization of grain size is the drag (pinning effect) that the particles exert on the migrating grain boundaries. This mechanism is applied commercially in the control of grain size in steels [47, 50].

II.G. COARSENING KINETICS OF SECOND PHASE PARTICLES

Coarsening occurs as multiphase systems reduce the interphase surface area per unit volume with time of exposure at elevated temperatures, with or without stress. The driving force for coarsening is the reduction of total chemical potential associated with curvature of the interface between the matrix and second phase. Specifically, the system coarsens to minimize the energy associated with the interfacial surface by reducing the surface area per unit volume of the second phase. Coarsening occurs by some combination of diffusion and/or coalescence as discussed below. The first mechanism, Ostwald Ripening [51], occurs by diffusion of mass from

the smaller to the larger particles. The smaller radius of curvature and hence high chemical potential for the smaller particles increases the solute equilibrium solubility in the matrix thus creating a concentration gradient between the smaller and larger particles. This net result of this diffusion rate controlled process is an overall increase in the average particle size and spacing. The second mechanism, coalescence, occurs when dispersed particles are mobile in the matrix (as in a liquid or when a solid matrix undergoes plastic deformation under an applied stress such as during consolidation by hot isostatic pressing, as done in this study) and two or more particles make contact and coalesce by sintering.

Coarsening by either of these mechanisms may be affected by factors such as stress, strain rate, changes in particle coherency, and changes in particle shape. Stress, for example, may result in enhanced anisotropy of diffusion and/or may interact with interfacial tensions to result in second phase particle shape changes. Strain rate may influence whether a pair of colliding particles can coalesce before they are separated by matrix motion. A change in particle coherency may result in a change in the interfacial energy (chemical potential) and thus a change in the driving force for coarsening. This could also be the case in a system with a limited amount of a contaminant that segregates to the phase boundary. In a system of small particles, the interfaces would not be saturated with the contaminant but as the particles grow the interfaces would gradually become saturated with the contaminant as the interface area per unit volume of the material is reduced. Changes in particle shape, specifically, deviation from a spherical particle, would reduce the separation distance between particles and thus influence the coarsening rate.

II.G.1. LIFSHITZ, SLYOSOV, AND WAGNER

The first major advance in the development of a theory to explain the phenomena of Ostwald ripening [51] was made independently by Lifshitz and Slyozov [52] and Wagner [53] more than 50 years after Ostwald's discovery of the phenomena in 1900 in the red and yellow mercury oxide system. The LSW theory made quantitative predictions of the long time behavior

of diffusion controlled coarsening systems. The LSW theory has been extensively reviewed and experimentally verified in the literature [54-58]. According to LSW theory [56], particle coarsening kinetics proceeds according to the equation

$$R_{ct}^3 - R_{co}^3 = kt \quad (5)$$

where R_{ct} is the mean particle radius of the coarsening particles at time t , and R_{co} is the starting mean particle radius of the coarsening particles at the onset of coarsening ($t = 0$).

The rate constant k is given by

$$k = 2gDcV^2/(d^2RT) \quad (6)$$

where g is the particle/matrix interfacial energy, c is the concentration of the particle atoms in the matrix in equilibrium with a particle of infinite size, V is the molar volume of the precipitate, d is a numerical constant related to the distribution of particle sizes which in LSW theory for spherical particles has value 3/2 (The maximum particle size is 3/2 times the "critical" dimension.), R is the gas constant, and T is the absolute temperature [57].

Unfortunately for the Cu-Ta system, values of g , D , and c could not be located. As discussed in a later section, since d can vary from the ideal value in experimental systems, a value for k cannot be calculated.

Based on the summary of Lifshitz and Slyozov for a system of uniformly distributed (size and spacing) spherical particles [52]:

1) During coarsening, a critical dimension (particle size) is determined such that particles of size greater than the critical dimension grow at the expense of particles of size less than the critical dimension. This is in agreement with the concept that larger particles grow at the expense of smaller particles. However, L and S further state that, on average, all particles greater than some critical size in the distribution of sizes will grow at the expense of particles smaller than the critical size. This mean field approach does not predict the behavior of individual particles in response to their local environment but does predict the behavior of the distribution of particles as a whole.

2) At long times the critical dimension asymptotically approaches the $t^{1/3}$ dependence from the initial transient prior to steady state coarsening. Correspondingly, the degree of supersaturation of the matrix correspondingly falls as $t^{-1/3}$ and the number of particles falls as t^{-1} . The critical dimension is a particle size and so at long times, past the initial transient conditions prior to the onset of steady state coarsening, it should have the form of equation (5). Since the supersaturation of the matrix is coupled to the chemical potential $1/R$, it follows that supersaturation of the matrix should fall as $t^{-1/3}$. Conservation of volume and the R^3 dependence of volume of individual particles indicate that the number of particles should fall as t^{-1} .

3) The distribution of particle sizes with time approaches a certain universal function such that the maximum sized particle has a dimension 3/2 times the critical dimension. Derivation of the predicted asymptotic distribution by L and S is presented in references [52] and [59]. The initial transient is the growth of second phase particles from solid solution and goes on until the degree of supersaturation has fallen enough for the critical size to catch up with the average particle size after which the average particle size is approximately equal to the critical particle size. The initial approach to the steady state distribution function is the reason for the asymptotic approach to steady state behavior of critical dimension, degree of supersaturation of the matrix, and the number of particles.

4) The effects of strain and anisotropy can be taken into account by the use of "effective" parameters in the calculation of the critical size and the form of the distribution function is unaffected by these considerations. L and S [52] indicate that the distribution function is not affected if the growing particle produces an elastic deformation of its surroundings. However, they do not make allowances for variations in elastic deformation which may depend on particle size such as those associated with coherency stresses or elastic interactions with other nearby particles. This again is due to the mean field nature of equation (5).

The major limitation of LSW theory is the mean field nature of the kinetic equation (5) which assumes that the coarsening of an individual particle is independent of its surroundings. This gives the implausible conclusion that a particle with larger nearest neighbors would coarsen at the same rate as a particle of the same size with smaller nearest neighbors. This limitation gives rise to disagreements between theoretical and experimentally observed particle size distributions when the second phase volume fractions are such that the diffusion fields of individual particles overlap and individual particles interact more strongly with their immediate environment (clustering effects) than with the average environment of the material [54, 55]. It has been observed that at volume fractions as low as 3% individual particle coarsening rates are not a smooth function of particle radius but instead vary according to the particle's local environment [55]. In the limit, the LSW theory is only valid for very small (near zero) second phase volume fractions and may not be valid at the relatively high second phase volume fractions of present interest in this current work on the Cu-Ta system.

Classical particle coarsening theory states that the initial particle size distribution will evolve into the LSW distribution [60]. Recent theoretical and computer modelling work by Brown [60] indicates that many particle size distributions are possible and the one that develops will be that which most closely resembles the tail of the initial distribution once nucleation and diffusion controlled growth is complete. Experimental work by Morris and Morris [61] on heat treated (700 - 800 C), melt spun Cu-Cr alloys indicated a bimodal Cr particle size distribution with larger Cr particles on grain boundaries and triple points and smaller Cr particles in the grain interiors. Other experimental work by Morris and Morris [61, 62] on melt spun Cu-Cr alloys indicated a trimodal Cr particle size distribution with the largest Cr particles being primary Cr particles formed uniformly throughout the liquid, the medium sized Cr particles on grain boundaries and triple points, and the smaller Cr particles formed as precipitates in the grain interiors. From these studies it is evident that matrix morphology and processing influence the particle size distribution, causing significant deviations from the monomodal particle size distribution predicted by LSW theory.

Fundamentally, this is to be expected when the initial particle size distribution is nonuniform and diffusion is strongly coupled to matrix morphology.

II.G.2. OTHER RECENT MODELS

In order to circumvent the assumptions and limitations of the LSW theory, recent coarsening models have been proposed to account for the diffusional interaction between particles. Models of the coarsening process for finite volume fractions of the coarsening phase have been reviewed in the literature by Courtney [54], Voorhees [55], and Li and Oriani [63]. Models reviewed include those proposed by Brailsford and Wynblatt (chemical rate theory to determining statistically averaged growth rate of a particle) [64], Voorhees and Glicksman (V-G, computer simulation to produce statistical averaging) [55], Glicksman and Voorhees (uses simulation data of V-G to construct an effective medium to reproduce rate constant data derived from the simulations) [55], Marquesee and Ross (determine statistically averaged kinetic equations by writing the microscopic equations in the form of a multiple scattering series and averaging the resulting particle positions, assuming the particle positions are independent) [65], Tokuyama and Kawasaki (three characteristic length and time scales for first order phase transformation process: one characteristic of a nucleation stage, a second pertaining to an intermediated growth stage where the second phase volume fraction is a function of time, and a third characteristic of a late or ripening stage where the second phase volume fraction is constant [55]) [66], and Davies, Nash, and Stevens (analyze coalescence and the shape of the remaining particle [54]) [67].

Recent work by Johnson and co-workers incorporates the effects of particle-particle interactions, elastic stress, and lattice anisotropy on the kinetics of Ostwald ripening and particle shape transitions during coarsening. One of the more interesting results of this work is that in elastically controlled systems, properly oriented smaller particles may grow at the expense of larger particles [68-73]. Based on the conclusions of Johnson and co-workers: 1) The growth rates of two elastically and diffusionaly interacting particles may be significantly

different and even of opposite sign than the calculated growth rates for systems in which the coarsening process is driven solely by interfacial curvature [68]. Thus, the classical (LSW theory) expectation of larger particles growing at the expense of smaller particles may not always be correct. 2) Since the particle growth rate depends on whether the system is elastically or capillarity controlled, general coarsening kinetics laws will be different than those predicted by Lifshitz and Slyozov [68]. 3) There may be a transition from capillary controlled growth to elastically controlled growth as the particles coarsen. This has been experimentally observed in the Ni-Al system [73]. 4) Size and stress induced precipitate shape transitions can occur in materials possessing cubic symmetry [70]. The size induced transition occurs during growth of the precipitate under constant or zero applied external stress and is due to the changing contributions of the interfacial and elastic energies to the total system energy with precipitate size [70]. Stress induced transitions occur at constant precipitate size in response to a change in the external stress and are due to changes in the relative contributions of the interfacial and elastic energies to the total system energy with changes in the external stress [70] 5) Size induced shape transitions in the absence of external stress may be first-order, involving a jump to a different precipitate shape or second-order, involving a smooth transition between precipitate shapes with growth of the precipitate [70].

With the many models available, several points emerge that are of relevance to the present work on the Cu-Ta system: 1) If the LSW theory does apply, there should be an initial transient in the particle size distribution before the "universal" monomodal distribution emerges for steady state coarsening. 2) Apparently stable multimodal particle size distributions have been observed in the Cu-Cr system, which is anticipated to be similar to the Cu-Ta system. 3) The coarsening behavior of an individual particle is dependent on its local composition and stress environment, including elastic coupling to nearby particles and response to applied external stress. The elastic factors may even cause smaller particles to grow at the expense of larger particles; which is the reverse of the classical coarsening process driven by interfacial curvature. This has been observed experimentally in systems with cubic symmetry.

- 4) Particle shape transitions may occur due to changes in the relative contributions of the interfacial and elastic energies to the total system energy with changes in the external stress or particle size.

II.G.3. COARSENING IN NON-IDEAL SYSTEMS

The coarsening of particles in real systems may be influenced by combinations of the following factors which may cause deviation from the idealized models: 1) Nonuniform particle distributions may lead to coarsening dependent on the local particle density [55]. 2) Stress, electric, or magnetic fields may influence the preferred diffusion direction [35, 55, 68, 70, 72, 74, 75]. 3) Crystallography may influence diffusion through lattice anisotropy, especially in a single crystal or large grained (a large grain size relative to particle spacing) matrix [69, 70, 72, 73]. 4) Grain size in relation to particle spacing will influence the effects of rapid grain boundary diffusion on coarsening [74]. 5) The particle/matrix interface may undergo a transition from coherent to incoherent, changing the strain field in the surrounding matrix. 6) Real particles are not necessarily spherical but may have faceted shapes in response to elastic and surface tension effects [63]. 7) The matrix may be unstable while undergoing hot working, recrystallization, or recovery [56]. 8) Temperature gradients may influence diffusion [54]. 9) Impurities and multicomponent particles may strongly influence coarsening behavior [56]. Some of the recent models account for some of the above factors. However, as of yet, no truly universal coarsening theory has been developed.

III. EXPERIMENTAL PROCEDURE

The experimental procedure is discussed in the following order: specimen preparation, specimen analysis, and computer modelling. The section on Specimen Preparation is divided into subsections on materials description, a description of the coating facilities, the deposition procedure used to make the alloy coatings, heat treatments, and hot isostatic pressing. The Analytical Procedure section discusses analyses including coating chemistry, scanning electron microscopy, transmission electron microscopy, x-ray diffraction, microhardness, and sheet resistance. The Computer Modeling section describes the application of Mathematica, a computer language developed by Stephen Wolfram [76], used on an Apple Macintosh II to write programming to generate theoretical mass and composition profiles for the ion plating system used in this study, to draw iso-composition and iso-sheet resistance contours from collected data, and to fit a Gaussian curve to x-ray data. A listing of the computer programs can be found in the Appendix.

III.A. SPECIMEN PREPARATION

III.A.1. MATERIALS DESCRIPTION

Alloy deposition was done using independently controlled electron beam evaporation sources with one source containing Cu (99.95 wt. %) and the other Ta (99.95 wt. %). The substrates were 25 mm square by 0.25 mm thick oxygen free high conductivity (OFHC 99.95% Cu) Cu foils and 25 mm square by 1.2 mm thick glass microscope slides. The Cu substrates were chemically polished prior to alloy deposition with a mixture of 6 parts by volume nitric acid : 27 parts by volume phosphoric acid : 65 parts by volume acetic acid. After chemical polishing, the Cu substrates were rinsed in deionized water, then ethanol, and dried with hot air. The glass substrates were rinsed with ethanol and dried with a lint free cloth. The substrates were prepared within 48 hours prior to coating and stored in a desiccator with silica gel both before and after coating to minimize the effects of humidity.

III.A.2. DESCRIPTION OF COATING FACILITIES

The films used for this study were grown in the ion plating facility at USA-CERL (United States Army Construction Engineering Research Laboratory) located in Champaign, Illinois. The basic ion plating system was built by Torr Vacuum, Inc and a schematic of the current configuration of the system is shown in figure 1. The system is a split chamber design which allows easy access for substrate holder mounting and for loading the source materials into the electron beam evaporators. Ultimate vacuum in this diffusion pumped system is better than 10^{-4} Pa. Details of system design have been presented elsewhere [20] and are briefly reviewed in the following paragraphs.

The upper chamber is a water cooled 0.66 m diameter stainless steel cylinder topped with a circular stainless steel plate. The top plate is bolted to the cylinder and sealing is accomplished with rubber o-rings. The water cooled substrate holder is held by an insulating Teflon feedthrough; the combination of which is designed to allow the source to substrate distance to be varied by raising and lowering the substrate holder. Water and electrical connections to the substrate holder are made outside the vacuum at the top of the pipe that feeds through to the substrate holder. Inside the chamber, the substrate holder is surrounded by a ground shield which is attached to the lid. The ground shield extinguishes the glow discharge on the back surfaces of the substrate holder thus allowing a more direct calculation of discharge power density. For this study, the stainless steel substrate holder was mounted onto a universal fixture that was threaded onto the water cooled feedthrough. Observation of the sources and substrates during deposition is accommodated by two viewports in the upper chamber. There are various other ports in the upper chamber to accommodate accessories to the system such as the capacitance pressure manometer and a thermocouple.

The lower chamber, also a water cooled 0.66 m diameter stainless steel cylinder, contains a 15 cm diameter oil diffusion pump, which opens into the side of the lower chamber, and a 25 cm diameter oil diffusion pump, which opens into the bottom of the lower chamber. Both diffusion pumps are backed by a single mechanical rotary pump. Electrical and water

feedthroughs for the electron beam evaporation sources mounted in the lower chamber also come through the bottom of the lower chamber. A baffle plate at the level of the evaporation sources provides a limited conductance between the upper and lower chambers allowing processing in the upper chamber at pressures above 10^{-3} torr (0.13 Pa) while maintaining the lower chamber at pressures below 10^{-3} torr (0.13 Pa) for extended life of the electron beam source filaments. Pressure in the lower chamber (below the baffle plate) is monitored by an ionization gauge. Various other ports in the lower chamber accommodate system accessories to such as a residual gas analyzer (RGA), a gas inlet from the mass flow controllers, and a chamber vent valve.

The electron beam evaporation sources are powered by a 14 kilowatt Airco Temescal CV14 power supply. A system of interlocks shut down the power supply under conditions such as inadequate vacuum and inadequate cooling water flow rates. The sources are composed of a thermionic emission filament, a magnetic beam deflection system and a water cooled Cu crucible to contain the coating source material. The beam is deflected 270 degrees to allow the electron source to be remotely located (below the baffle plate) from the crucible to minimize coating of the filament assembly and maximize the filament life.

Power to the substrate holder to sustain the glow discharge is supplied by an RF Plasma Products 1.2 kW RF generator and tuning network. The system is interlocked and shielded to eliminate electric shock hazard and to allow use of other instrumentation on the deposition system while the RF power supply is operating.

III.A.3. DEPOSITION PROCEDURE

Prior to coating deposition, the interior of the ion plater chamber was cleaned and covered with aluminum. The system was then evacuated and Cu was evaporated to coat all exposed surfaces of the inside of the chamber and the substrate holder thus ensuring that any surfaces which may be prone to sputtering during the ion plating process would produce a minimum of contamination.

In preparation for coating deposition, appropriately identified glass (12) and Cu (23) substrates were mounted in a predetermined arrangement in the indexed substrate holder. The substrate holder was then mounted in the deposition chamber and the evaporation sources loaded. The chamber was then evacuated to better than 5×10^{-4} Pa (3.75×10^{-6} torr). Research grade argon gas was then let in through a mass flow controller to maintain a support gas pressure of about 7 Pa and an RF bias was applied to the substrate holder to create a glow discharge of 1.2 W/cm^2 . The substrates were thus sputter cleaned for approximately 10 minutes prior to coating deposition. After 8 minutes of sputter cleaning the evaporation sources were activated and after 9 minutes of sputter cleaning the evaporation sources were brought slowly to the desired power level. For runs made with no ion bombardment (evaporation in the presence of a support gas), the RF power supply was shut off after 10 minutes of sputter cleaning, or when the evaporation sources reached the desired power level. For runs made with ion bombardment (ion assisted deposition in the presence of a glow discharge support gas), the RF power supply was set at the desired power density when the evaporation sources reached the desired power level. After deposition for a specified time, the evaporation sources and the RF power were shut off and the system was allowed to cool ($T_{\max} < \sim 350\text{C}$) to near room temperature before venting. Coated substrates were stored in individual plastic boxes labeled with the run number and indexed sample holder position number; labels were given of the form **XXYY** where **XX** is the two digit substrate holder position index and **YY** is the run number.

III.A.4. COARSENING HEAT TREATMENTS

Selected coatings on Cu substrates were vacuum encapsulated in quartz tubing (to minimize oxidation during heat treatment) and heat treated for 1, 10, and 100 hours at 800 Celsius and 10 and 1 hours at 900 Celsius. Specimens were selected to be representative of low (about 5 atomic %) and high (about 20 atomic %) Ta contents from runs deposited with (biased) and without (unbiased) substrate bias. Since the amount of material for a given

composition was limited, successive heat treatments were carried out only after it was known how the material responded to the previous heat treatment.

At this point it was necessary to modify the specimen labelling format to keep track of the heat treated specimens. Labels were given of the form **XXYYZZ** where **XX** and **YY** have the same meaning as above and **ZZ** has value 01 for as-deposited material and 02 through 06 correspond to the heat treatments in the order discussed above.

III.A.5. HOT ISOSTATIC PRESSING

Selected coatings on Cu substrates were mounted face to face between OFHC Cu half-rounds in 9.7 mm inside diameter annealed Cu tubing which was then evacuated, pinched-shut, and sealed by welding. The encapsulated samples were hot isostatic pressed for 1 hour at 900 Celsius and 172 MPa to determine the effects of consolidation on the composite microstructure and for comparison with a specimen identically heat treatment in the absence of applied stress.

III.B. ANALYTICAL PROCEDURE

III.B.1. CHEMISTRY

Coating chemistries were evaluated at the centers of coatings on glass slides using energy dispersive x-ray analysis (EDX). The equipment consisted of an EDAX unit mounted on an AMRAY 1610 Turbo SEM (located at USA-CERL). EDX data collection was done at a magnification of 500x (collection area was approximately 0.18 mm x 0.23 mm). EDX chemical analysis was done using the Cu K α 1 (8.048 keV) and the Ta M α 1 (1.710 keV), the Ta L α 1 (8.146 keV) was not used because of its proximity to the Cu K α 1. Data reduction was done using the semiquantitative (standardless) mode. Although the composition values that this method gives may not be exact, this approach is internally consistent and adequately determines variations in coating chemistries and identifies coatings with comparable (+ or - 2 atomic %) Ta contents.

III.B.2. SCANNING ELECTRON MICROSCOPY

Scanning electron microscopy (SEM) was used to determine coating morphologies and the response of morphology to processing for selected samples. Specimens observed with SEM included sharply bent samples (to examine coating fracture and qualitatively determine adhesion), polished cross sections of hot isostatic pressed samples (to analyze particle sizes and distribution), and microhardness-indented, polished HIP cross sections (to qualitatively determine plastic deformation behavior). SEM studies were done on both the AMRAY 1610 located at USA-CERL and on the Hitachi S800 located in the University of Illinois Center for Microanalysis of Materials in the Materials Research Laboratory.

III.B.3. TRANSMISSION ELECTRON MICROSCOPY

Transmission Electron Microscopy (TEM) was used for analysis of coating structures such as matrix grain size, second phase particle size and distribution, and dislocations. Bright and dark field imaging, selected area diffraction, and EDX TEM techniques were utilized in this study. TEM work was done on Phillips models 400, 420, and 430 microscopes located in the Center for Microanalysis of Materials.

Broad face TEM specimens were prepared by punching 3mm diameter disks such that the coating was on the concave surface, diamond honing the edges of the disks to make them uniform in height (typically 300 to 400 microns), mounting the disks on a metal block in the centers of number 4 stainless steel washers with crystalbond and then polishing to remove the substrate to within a few microns of the coating substrate interface before ion milling to penetration. Material removal was done such that the damaged region created by coarser papers was removed by the finer papers and all polishing stages were done wet. A typical polishing routine consisted of: 1) Sand on 180 or 220 grit until the polishing plane touches the backs (substrate side) of the specimens. From this point the distance to the coating substrate interface is known to be approximately 250 microns and the total sample plus block thickness is then measured with a micrometer and checked frequently throughout the polishing up to the second to last wheel. 2)

The sample is sanded successively on 320 grit paper down to about 150 microns, 400 grit to about 50 microns, and 600 grit to about 15 microns of substrate thickness. 3) Polishing on a 600 grit wheel randomizes the scratches and removes about 10 microns of substrate thickness, leaving about 5 microns of substrate thickness. 4) Polishing is next done with 0.3 micron alumina to remove about 3 microns of substrate thickness and this is followed by polishing with 0.05 micron alumina to remove most of the remaining substrate material. Ideally, the coating is not visible on the final polish; but the specimen should rumple slightly when released from the crystalbond.

Tips for best results: 1) Use an aluminum polishing block in the shape of an equilateral triangle about 7 cm on edge and at least 2 cm thick. 2) Mount four samples at a time; one near each corner and one near the center. Since three points determine a plane, varying the pressure at each of the corners of this configuration allows good control of material removal. 3) Index the corners to keep track of how much material is removed from each specimen and appropriately vary the pressure to each corner during polishing. 4) Pre-sand sets of washers to 320⁰ grit so that they have a flat surface in contact with the polishing block. 5) Using the lowest temperature possible to melt the crystalbond to avoid sample oxidation, remove all bubbles from the crystalbond before mounting the samples. Mount the washers first, then mount the specimens, making sure that no bubbles become trapped. 6) Rinse the specimens in clean acetone to remove all crystal bond after polishing/demounting and before ion milling. 7) Ion mill only from the substrate side of the sample and stop after first penetration.

III.B.4. X-RAY DIFFRACTION

X-ray diffraction was done on a Rigaku D-Max diffractometer located in the Center for Microanalysis of Materials. Using a Cu x-ray source operated typically at 45 Kv and 20 millamps to generate Cu k α ($\lambda = 1.54056 \text{ \AA}$) radiation, diffraction analyses of these relatively thin films required summing the results of 30 passes from 5 to 100 degrees 2 Θ at 8 degrees per minute and with a resolution of 0.02 degrees per step. Specimens were mounted onto glass

slides with double-stick tape and a blank substrate was mounted in the grip region of the diffractometer mounting stage to ensure that the specimen was in the goniometer plane. Care was given to ensure that the specimens were not stuck so well as to be deformed when removed from the mounting glass slide. X-ray data was acquired by computer and stored on disks for later processing. X-ray data was used for phase identification and to quantify particle coarsening.

III.B.5. MICROHARDNESS

Microhardness data was acquired using a Leitz microhardness tester with a Knoop indenter and loads of 10 and 25 P. The Knoop hardness is given by

$$H_K = 14230 \frac{P}{l^2} \quad (7)$$

where H_K is the Knoop hardness, P is the load in ponds, and l is the indent length in microns. Hardnesses were calculated from the average length of at least 5 indents.

III.B.6. SHEET RESISTANCE

Sheet resistance measurements were done using a VEECO four point probe located in the undergraduate semiconductor processing laboratory in the Department of Electrical and Computer Engineering at the University of Illinois. Measurements were made on as-deposited coatings on glass substrates. Sheet resistance was calculated as the average of at least 5 measurements near the center of each specimen.

III.C. COMPUTER MODELING

III.C.1. MASS PROFILES

The following section describes the development of a computer program to generate vapor deposited mass (thickness) profiles for a PVD coating in the absence of sputtering. Mass profiles were calculated based on the well known cosine law [35],

$$\delta M_r(\Phi, \Theta)/\delta A_r = (M_e \cos\Phi \cos\Theta)/(\pi r^2) \quad (8)$$

where δM_r is the incremental mass, δA_r is the incremental area, M_e is the mass of material evaporated, Φ is the angle between the source point plane normal and the vector to the substrate, Θ is the angle between the substrate normal and the vector to the substrate from the source, and r is the source to substrate distance. For the system geometry in the present study the source plane is parallel to the substrate plane so $\Phi = \Theta$. From geometry it can be shown that at a point (x, y, z) on the substrate holder the incremental mass per incremental area is given by

$$M_e (\Delta z)^2 / (\pi ((\Delta x)^2 + (\Delta y)^2 + (\Delta z)^2)^2) \quad (9)$$

where the deltas are the coordinate axis distances from point (x, y, z) to the point source location. For deposition from two sources, the net deposition at a point on the substrate holder is the sum of the contributions from each source. Since uniformity (thickness, deposited mass) of the deposit was the observation of concern, the data is best displayed as a value relative to a reference point, which was chosen as the center point of the substrate holder which lies directly above the midpoint of the line connecting the point sources. Approximating the electron beam evaporation sources as point sources is reasonable as long as the source to substrate distance is at least 10 times the source dimension [35]. Data is displayed as a color code on a scale ranging from 0 to 2 times the deposit at the reference point. Since the line that connects the sources is a mirror line in the profiles, the sources are set up to lie along the line $y = 0$ and half the needed values for the graphic are calculated with the other half inferred by "reflecting" through the mirror line. The computation was set up to calculate values at the center of one centimeter square elements on a square substrate holder with a thirty centimeter edge. In principle, any desired resolution could be calculated, keeping in mind that the computing time increases as the square of the reciprocal of the resolution.

III.C.2. COMPOSITION PROFILES

A computer program was developed to calculate and display vapor deposited composition profiles for a PVD coating in the absence of sputtering. If we substitute the number of atoms evaporated for the mass evaporated in the equations developed in the preceding section, these equations can generate the number of atoms deposited at a point on the substrate from each of the sources. If A is the number of component "a" atoms from one source, and B is the number of component "b" atoms from the other source, then the "a" content of the coating at any point is $A/(A+B)$. This is implemented similarly to the mass calculations and the composition results are presented with a color scale corresponding to 0 - 100% of one of the components.

III.C.3. SPUTTERING EFFECTS

The following section describes the incorporation of sputtering effects into the previously described thickness and composition computer calculations. When incorporating sputtering effects into the above calculations, the following assumptions are made: 1) The cosine law still holds for primary deposition so than at the limit of no sputtering, the result is the same as for the previously described calculations. 2) The flux density of bombarding ions is constant across the entire substrate holder. 3) The absolute sputter yield of a given component is independent of the surface composition (component "a" atoms always have sputter yield S_a and component "b" atoms always have sputter yield S_b). However, based on simple probability the observed sputter yield is linearly dependent on the atom fraction of that component in the surface. 4) Atoms that are sputtered off the substrate holder are lost; the only sources of depositing atoms to the substrate holder are the two "point" evaporation sources.

From the calculated mass profiles in III.C.1. and assumption number 2 described above, it is apparent that the ratio of bombarding ions to depositing atoms is not constant across the substrate holder. A correction for this was made by considering the ratio of bombarding ions to depositing atoms at a reference point and then scaling that value appropriately to apply at other points on the substrate holder. The reference point is the same as that described previously for

the mass profiles. Keeping in mind that mass and number of atoms are interchangeable in the equations developed for the mass profiles, the reference mass (**refm**) is the sum of the number of atoms from each of the sources at the reference point (**refm = A_{ref} + B_{ref}**). The origin ratio is defined as the ratio of bombarding ions to depositing atoms at the reference point. The ratio of bombarding ions to depositing atoms at the point of interest, **Irat**, is given by the origin ratio times the reference mass divided by the sum of the contributions from the two sources at the point of interest, **A + B**. The number of "a" atoms deposited in the presence of sputtering, **A_s**, is proportional to the sputter yield and the flux of "a" atoms as a fraction of the total flux of atoms to the substrate at the point of interest and is given as

$$A_s = A - Irat S_a \quad A/(A+B). \quad (10)$$

Parallel development for **B_s** yields

$$B_s = B - Irat S_b \quad B/(A+B). \quad (11)$$

It then follows that the total number deposited of deposited atoms (or thickness or mass, whichever the reader prefers) at the point of interest is given by **A_s + B_s**. The program uses this to scale the value to the reference value in the absence of sputtering and plots an "a" color scale between 0 and 2 times the reference value. For composition calculations, the "a" content of the coating is given simply as **A_s/(A_s+B_s)**. This was implemented to generate composition profiles in the same way as the previous composition profiles. Note that it is possible for **A_s** and/or **B_s** to have negative values which would give a nonphysical result; the programs look for this condition and color code those locations as black. Also, the program for mass profiles color codes locations white if the deposited mass exceeds twice the reference value in the absence of sputtering.

III.C.4. X-RAY DIFFRACTION PEAK FITTING

The following describes the development of a computer program to fit x-ray diffraction peak data to a Gaussian curve of the form

$$I[x] = (c/s) \quad Exp[-(x-u)^2/(2s^2)] \quad (12)$$

where x is the two theta angle on the x-ray scan, I is the intensity, c is a scaling constant, s is a standardized peak width which has the same value as the standard deviation in a Gaussian data set, and u is the average value of x (ideally the point of maximum intensity). Since the term s appears both inside and outside the exponential, standard least squares fitting is not applicable. Treating the s value as a standard deviation for the data set, which it is if the data set is large enough, always underestimated the value of s needed to give a good fit to the data in the present work.

Another approach is to fit the data pair-wise and use the average values of the solved for variables. In this approach, data points are input as ordered pairs of form $\{x_i, I[x_i]\}$. The value of u is calculated as $\text{Sum}[x_i I[x_i]]/\text{Sum}[I[x_i]]$ and is used to calculate values of s for all possible pairs of data points according to the relation

$$s_{1,2} = \text{Sqrt}[\text{Abs}[(x_2 - u)^2 - (x_1 - u)^2] / (2 \ln[I[x_1]/I[x_2]])]. \quad (13)$$

It should be noted that for conditions where $I[x_1]$ approaches $I[x_2]$, division by zero will cause an error, so, pairs of points of near the same intensity are not used. An average value of s is calculated from the generated values of s , and this average s is used to calculate values of c according to the relation

$$c = I[x_i] s \text{ Exp}[(x_i - u)^2 / (2s^2)]. \quad (14)$$

An average value of c is calculated from the generated values of c . A fitted curve using u and the average values of s and c is then plotted on the same graph with the data points for visual comparison and values for u , s , and c are output along with a list of the data points and a label.

The value of s is the term of most interest from the calculation since it is independent of total peak intensity and proportional to the breadth of the peak. From Cullity [77], in the absence of nonuniform strain the breadth of the x-ray peak, B (the width of the x-ray peak at one half maximum intensity), is proportional to the spherical particle size by the relation

$$B = 1.33 \lambda / (t \cos \theta), \quad (15)$$

where λ is the x-ray wavelength, t is the diameter of the crystal particle, and Θ is the Bragg angle. The value for B needs to be corrected for instrumental broadening according to the relationship

$$B^2 = B_m^2 - B_s^2 \quad (16)$$

where B_m is the measured breadth of the peak of interest on the specimen of interest and B_s is the measured breadth of a standard with a peak near the peak of interest and a grain size greater than 200 nm. Using this and solving the peak fitting equation presented above for the width at half maximum intensity, we can derive an expression for the grain size in terms of s to be:

$$t = 1.33 I / (\text{Sqrt}[s_m^2 - s_s^2] \cdot 2\text{Sqrt}[2\ln[2]]\cos\Theta) \quad (17)$$

where s_m is the s (determined by peak fitting as described previously) for the peak of interest on the sample of interest and s_s is the s (determined by peak fitting as described previously) for the peak of interest on a sample of the material (Ta) with a grain size much greater than 200 nm. Annealed Ta wires with a grain size of about 0.5 mm were used as a standard for comparison of s values in this study.

~

IV. RESULTS

A number of Cu-Ta, Cu-Cr, and Cu-Nb alloys (coatings) were produced in conjunction with this work (49 runs at 35 substrates per run for a total of 1715 coatings, deposition conditions for each run are listed in the Appendix). Initially, nine runs were done to identify deposition parameters that would give "suitable" alloy compositions, with "suitable" being a "low" refractory content of about 5 atomic % and a "high" refractory content of about 20 atomic %. The Cu-Nb and Cu-Cr systems were dropped from consideration because of difficulties in controlling Cr levels (due to Cr sublimation) and because of the relatively high Nb diffusivity in Cu. The approximately 20 Cu-Ta runs consisted of codeposited and layered depositions, with and without substrate bias. Nonuniformity in layer thickness and inadequate amounts of "identical" material for subsequent heat treatments eliminated the layered materials from this study. Success with the codeposited Cu-Ta alloys thus made these materials the focus of this study.

From the codeposited Cu-Ta coatings it was desired to select coatings with high and low Ta contents deposited with and without substrate bias. To avoid run-to-run deposition variations, high and low Ta alloys were obtained from the same run and biased/unbiased runs were selected such that they had about the same composition ranges. Runs 18 (4.3 to 21.2 at. % Ta, biased) and 23 (5.7 to 22.8 at. % Ta, unbiased) were selected for the majority of the results presented in this thesis.

This section presents the results of an investigation into the physical metallurgy and high temperature coarsening behavior of non-equilibrium $\text{Cu}_{1-x}\text{Ta}_x$ alloys. The following sections present data regarding the basic nature of a dispersion of a nanoscale Ta particles in a Cu matrix and the coarsening behavior of such a dispersion of nanoscale Ta particles.

IV.A. COATING CHEMISTRY

Spanning values for coating chemistry were determined for the codeposited coatings made for this work to determine the range of coating chemistries accessible for each deposition run.

The extreme values for Ta contents for the deposition runs studied in detail in this work are shown in table 1. A complete tabulation of deposition parameters and composition data for all the coatings made in conjunction with this thesis are shown in the Appendix. From the ranges of coating chemistries it was desired to choose biased and unbiased runs that had nearly the same composition ranges for further study; runs 18 and 23 were chosen as previously discussed. Run 18 was deposited with 100 W RF (0.12 W/cm²) on the substrate holder during deposition and run 23 was deposited without bias.

Table 1. TABLE OF COATING TANTALUM CONTENTS IN ATOMIC PERCENTS

<u>Run#</u>	<u>Condition</u>	<u>Min. Ta</u>	<u>Max. Ta</u>	<u>Comments</u>
18	biased	4.3	21.2	
19	biased	8.3	34.8	material for HIP
20	unbiased	7.9	30.5	material for HIP
23	unbiased	5.7	22.8	
<hr/>				

After selection of the runs for further study from the spanning compositions, composition data from coatings on all the glass substrates in the chosen runs was then acquired. Composition contour maps were then generated by linear interpolation between pairs of glass substrates to give an indication of the composition on the Cu substrates between them. Composition contour maps for runs 18 and 23 are shown in figures 3 and 4 respectively; these contour maps assume only Cu and Ta are present and do not account for possible incorporation of residual gasses. The positions of all the substrates are indicated in the figures; the glass slides were at positions with double odd indices {{1,3}, {1,5}, {3,1}, {3,3}, {3,5}, {3,7}, {5,1}, {5,3}, {5,5}, {5,7}, {7,3}, {7,5}} and the Cu substrates were in the remaining positions. From the contours in figures 3 and 4 it can be seen than composition varies strongly as a function of position on the substrate holder. Specimens were selected for further study to be representative of low Ta content {{2,2}, {3,2}, {4,2}, {5,2}, {6,2}} (about 5 to 9 atomic

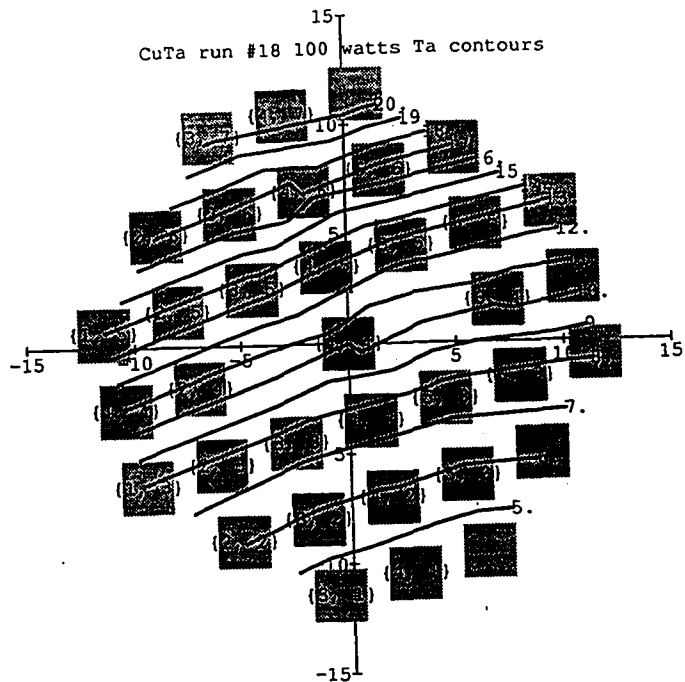


Figure 3. Composition contour map for run 18 (deposition with substrate bias) showing Ta content (atomic %) varying with position on the substrate holder (axes in cm). The Ta source was located ~below position {4,7} and the Cu source was located ~below position {4,1}.

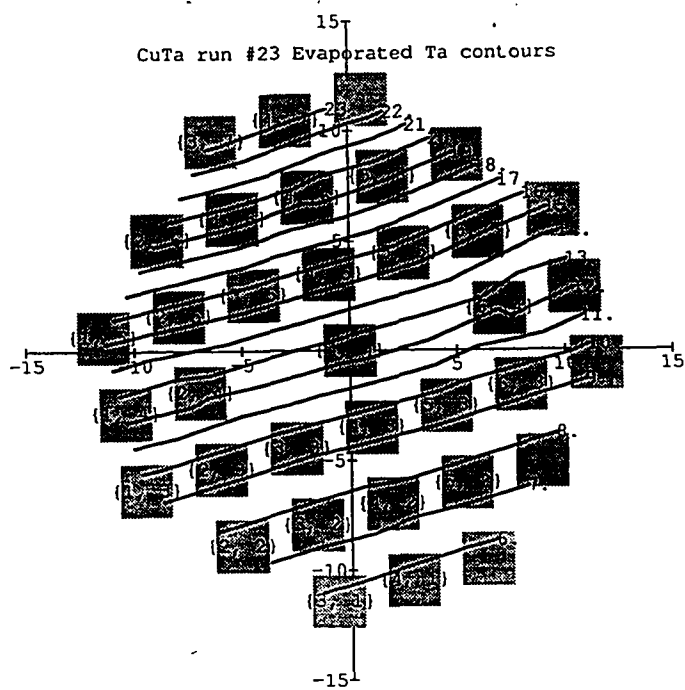


Figure 4. Composition contour map for run 23 (deposition without substrate bias) showing Ta content varying with position on the substrate holder (axes in cm). The Ta source was located ~below position {4,7} and the Cu source was located ~below position {4,1}.

percent Ta) and high Ta content {{2,6}, {3,6}, {4,6}, {5,6}, {6,6}} (about 15 to 21 atomic percent Ta) such that the specimens lay along isocomposition lines of approximately the same value for deposition with and without substrate bias. Specimens for hot isostatic pressing came from the same positions from runs 19 (biased 100 W RF) and 20 (unbiased); in this case, the low Ta content was in the range 9 to 15 atomic percent and the high Ta content was in the range 25 to 34 atomic percent.

IV.B. SEM ANALYSES OF COATING MORPHOLOGIES

Scanning electron microscopy (SEM) was used to investigate the effects of processing and composition on coating morphology. SEM investigations of fractured as-deposited coatings indicated that the coating morphology is dependent on both composition and RF bias during deposition. SEM micrographs of the structures observed for the as-deposited coatings are shown in figures 5 (biased, low Ta), 6 (biased, high Ta), 7 (unbiased, low Ta), and 8 (unbiased, high Ta).

~ Significant morphological features of the as-deposited alloys include: 1) The unbiased, low Ta alloy (figure 7) appears to consist of small, uniformly sized (approximately 300 nm), partially faceted grains, with little evidence of a columnar coating structure and the lowest apparent void content, compare figure 7 with figures 5 - 8. The fracture surface appearance of the low Ta alloy, figure 7, suggests greater ductility than for the biased or higher Ta specimens (figures 5, 6, and 8). 2) The unbiased, high Ta alloy (figure 8) appears to consist of a mixture of faceted particles, with a grain size about the same as that for the unbiased, low Ta alloy, and "powdery" (few tens of nm) grains. This specimen also has a more columnar coating structure and a higher visible void content than does the unbiased, low Ta alloy. 3) The unbiased, low Ta alloy (figure 5) appears to have a well defined columnar structure with well developed facets at the column tops. The grain size at the top of the columns appears to be on the order of the column width (approximately 1 micron) and the material at the column boundaries has a grain size approaching that of the powdery material observed in the unbiased, high Ta material. The

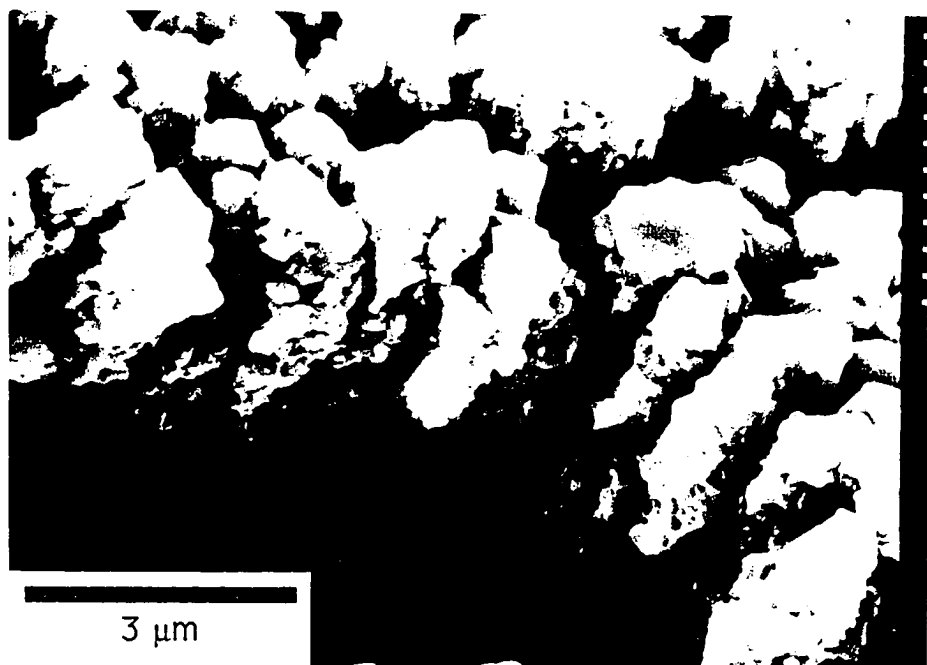


Figure 5. SEM micrograph of fractured specimen {2,2} from run 18 (bias deposited, low Ta), as-deposited, showing faceted columnar coating morphology.

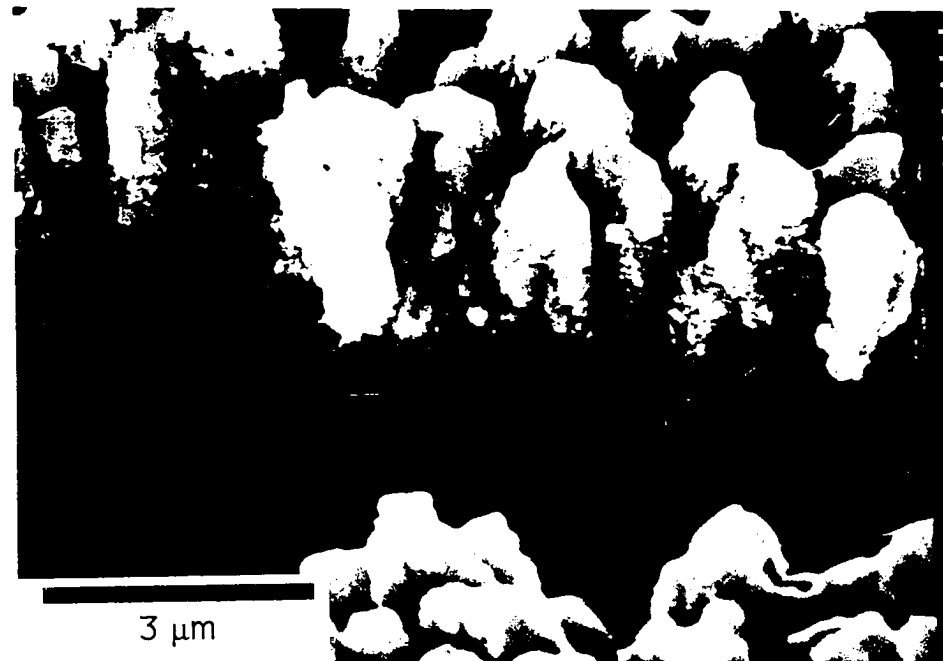


Figure 6. SEM micrograph of fractured specimen {2,6} from run 18 (bias deposited, high Ta), as-deposited, showing faceted columnar coating morphology.

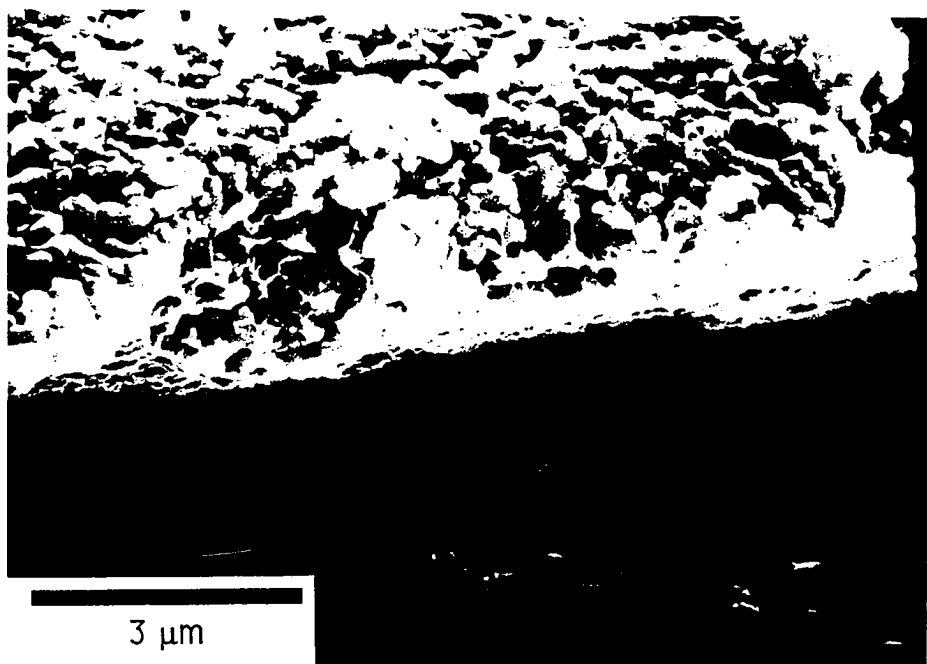


Figure 7. SEM micrograph of fractured specimen {2,2} from run 23 (unbiased, low Ta), as-deposited, showing granular noncolumnar coating morphology.

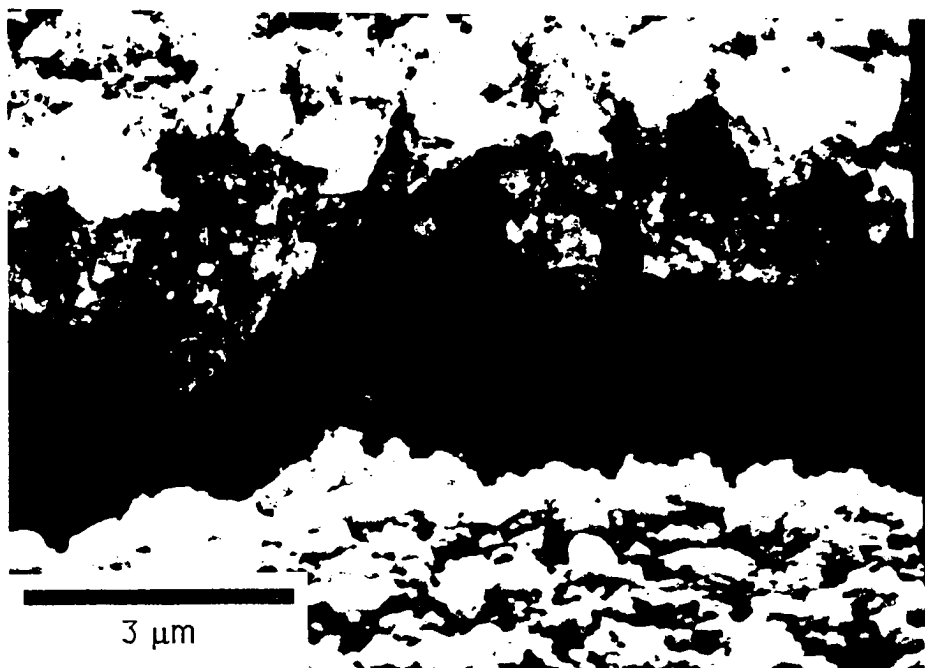


Figure 8. SEM micrograph of fractured specimen {2,6} from run 23 (unbiased, high Ta), as-deposited, showing powder-like, voided, weakly columnar coating morphology.

column widths in this material (poorly defined but approximately 2 microns) are larger than those for the biased, high Ta material (well defined, about 1 micron). The material appears to be weakly bonded at the column boundaries since fracture during bending for the sample preparation occurred with little evidence for ductile tearing at the column boundaries. Although there is more evidence for ductile tearing in this material than in the biased, high Ta material, the ductility is still lower than that for the unbiased, low Ta material. 4) The biased, high Ta material (figure 6) has a structure similar to that of the biased, low Ta material, except that the column size is smaller (approximately 0.5 microns) and the fracture appears to have less ductility. 5) For deposition with and without substrate bias, the high Ta material is thinner than the low Ta material; this is a consequence of system geometry during deposition and is in agreement with the results of computer modeling calculations discussed later. 6) Individual Ta particles in the codeposited alloys were not visible using secondary electron imaging; in a related study of layered microstructures, the Ta layers were distinguishable from the Cu layers due to their higher secondary electron output.

SEM observations of fracture cross-sections of the heat treated coatings indicated that the material responses are dependent on the coating morphology prior to heat treatment and, hence, on the composition and bias during deposition. Representative micrographs of the structures observed for the heat treated coatings are presented for the most extreme heat treatment (900 C, 10 hours) and are shown in figures 9 (biased, low Ta), 10 (biased, high Ta), 11 (unbiased, low Ta), and 12 (biased, high Ta). Significant microstructural features observed by SEM in the heat treated coatings include: 1) For the heat treated, unbiased, low Ta alloy (figure 11), individual grains visible in the as-deposited material are less well defined and the ductility appears to have increased relative to the as-deposited material. 2) For the heat treated, unbiased, high Ta alloy (figure 12), the larger grains on the surface have taken on a nearly spherical shape, although facets are still visible, and based on the fracture surface appearance the ductility of the material has increased after heat treating. The fact that the fracture surface has small regions which appear very ductile while others regions have the

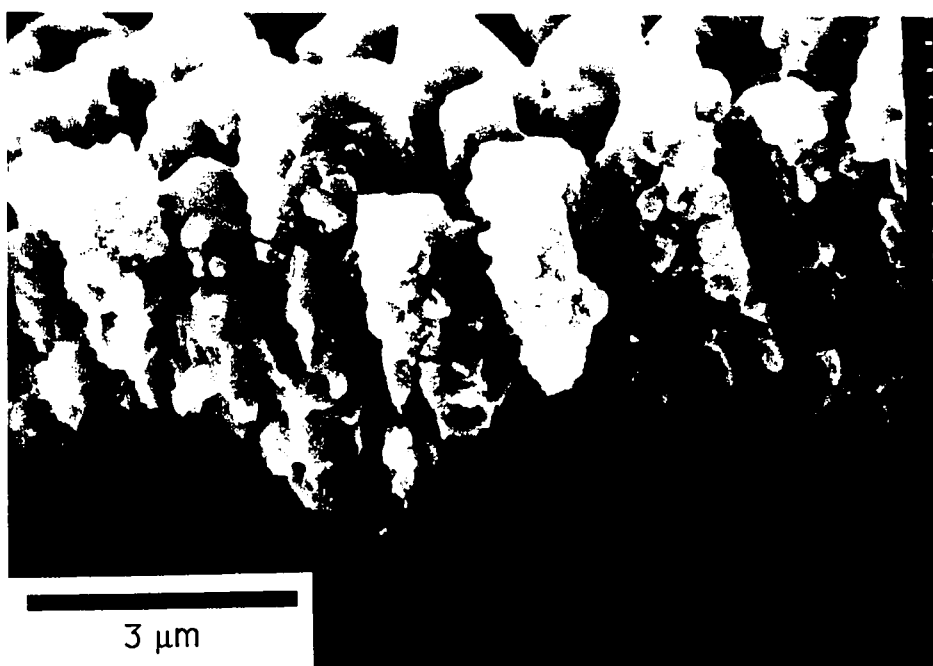


Figure 9. SEM micrograph of fractured specimen {5,2} from run 18 (bias deposited, low Ta), after heat treatment for 10 hours at 900 C, for comparison with figure 5.



Figure 10. SEM micrograph of fractured specimen {5,6} from run 18 (bias deposited, high Ta), after heat treatment for 10 hours at 900 C, for comparison with figure 6.

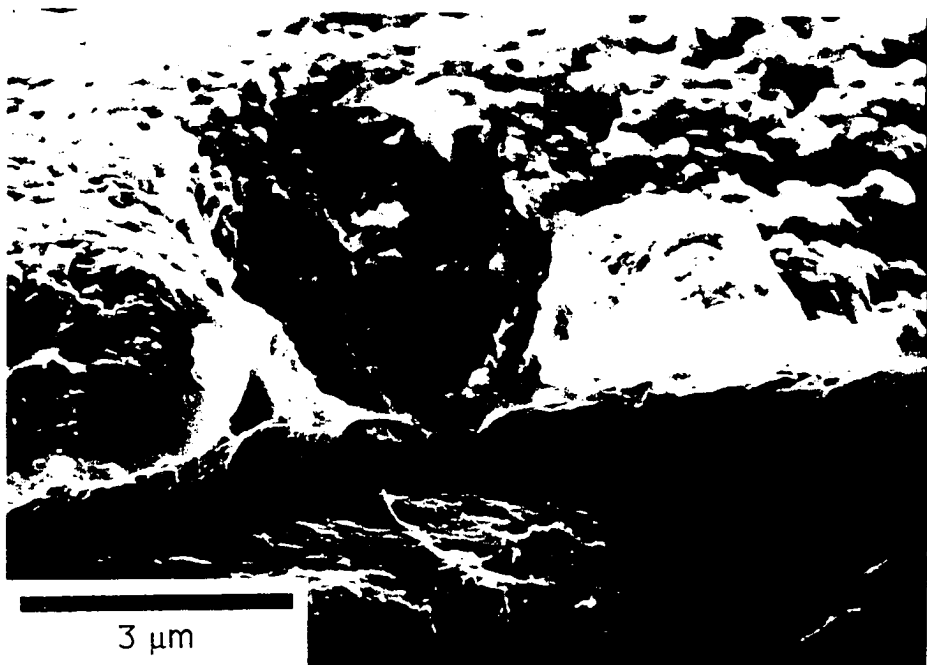


Figure 11. SEM micrograph of fractured specimen {5,2} from run 23 (unbiased, low Ta), after heat treatment for 10 hours at 900 C, for comparison with figure 7.

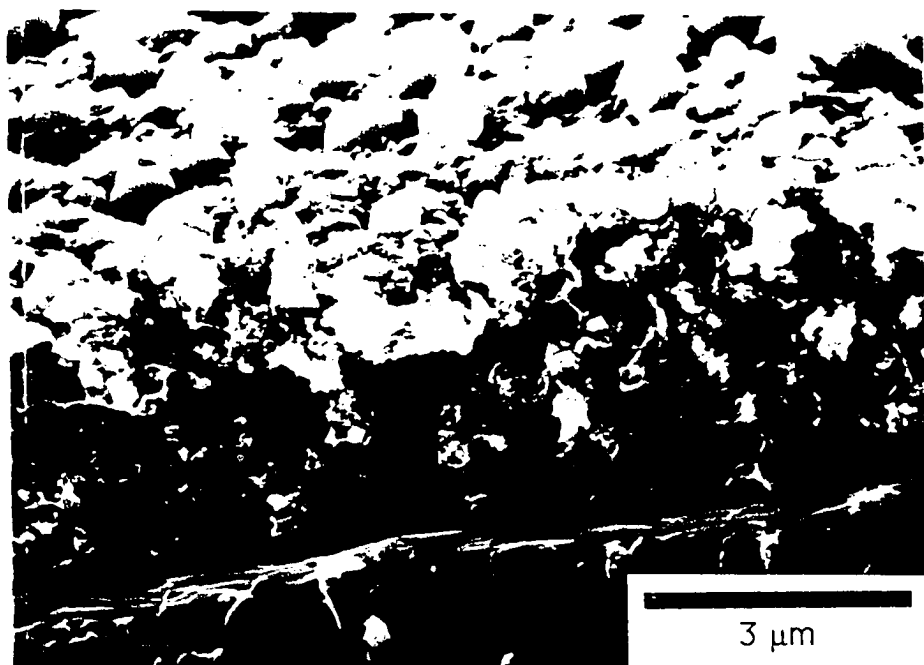


Figure 12. SEM micrograph of fractured specimen {5,6} from run 23 (unbiased, high Ta), after heat treatment for 10 hours at 900 C, for comparison with figure 8.

same appearance as the as-deposited material suggests that the coating contains voids. Interestingly, the fracture appears more ductile in the region adjacent to the substrate than in the region near the surface, suggesting possible reaction with residual oxygen in the deposition system or during heat treatment or between the coating and substrate during heat treatment. 3) For the heat treated, biased, low Ta material (figure 9), ductile tearing of the less voided region of the coating at the base of the columns appears to be increased after relative to that for the as-deposited material. Aside from this point, the fracture cross sections of the as-deposited and heat treated materials are indistinguishable. 4) The heat treated, biased, high Ta alloy (figure 10) is indistinguishable in its surface and fracture cross section appearance from the as-deposited alloy. 5) Individual Ta particles were not visible by SEM on the fracture surfaces of the heat treated specimens. 6) As observed by SEM, the responses of all alloys to the heat treatments were subtle and were less pronounced for the heat treatments intermediate to those presented above as the extremes.

SEM observations of polished cross sections of hot isostatic pressed (HIPped) specimens indicated that the consolidated morphology is dependent on the processing parameters during alloy deposition, particularly substrate bias. Representative micrographs of the HIPped specimens are shown in figures 13 (biased) and 14 (unbiased). The compositions of the coatings in these figures, about 15 atomic % Ta, are intermediate to those for the as-deposited and heat treated specimens discussed above. Significant features observed in the HIPped coatings include: 1) The second phase particles are easily visible by SEM through their higher secondary electron output relative to the Cu matrix. 2) The bias deposited material appears to have retained its columnar morphology, as indicated by outlining of the individual column boundaries by the second phase particles. 3) Alloys deposited with and without bias appear to have the same range of second phase particle sizes (few tens of nm to about 400 nm). However, the material deposited without substrate bias appears to have a much larger number and a much more uniform spatial distribution of the larger second phase particles. 4) The larger second phase particles in the material deposited with substrate bias appear to be concentrated in the

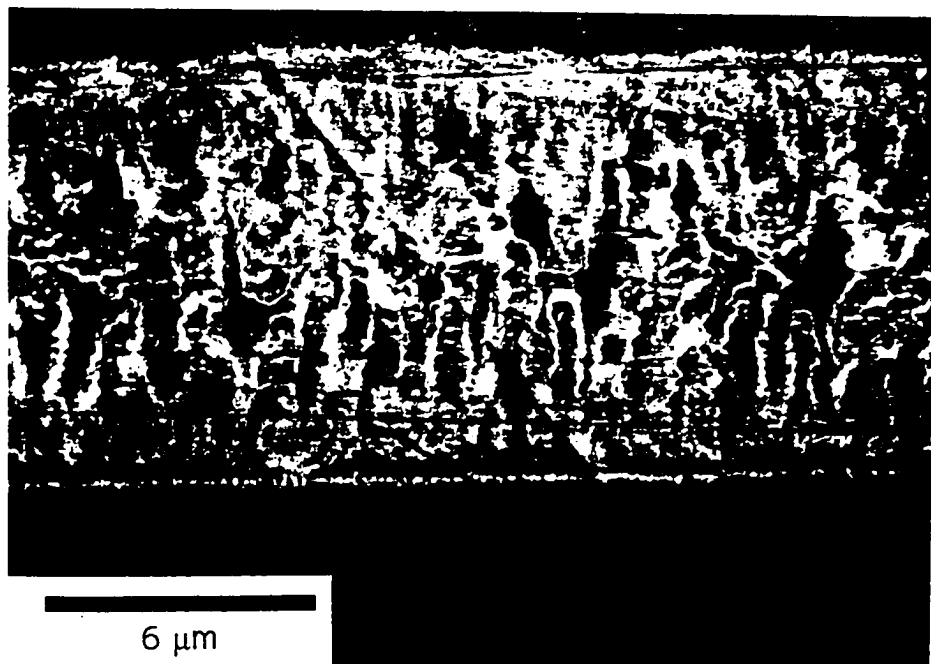


Figure 13. SEM micrograph of polished cross section of specimen {3,2} from run 19 (biased), after hot isostatic pressing for 1 hour at 900 C and 172 MPa, showing distribution of second phase particles in white.

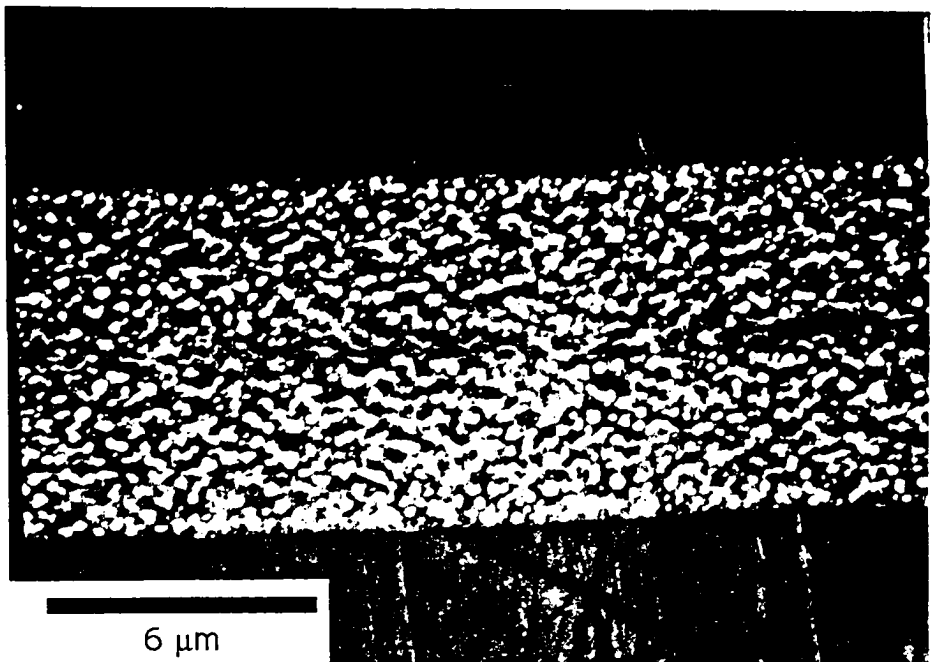


Figure 14. SEM micrograph of polished cross section of specimen {3,2} from run 20 (unbiased), after hot isostatic pressing for 1 hour at 900 C and 172 MPa, showing distribution of second phase particles in white.

center region of the consolidated structure corresponding to the upper portions of the columns on the coatings that were HIPped face to face. 5) The remains of the original interface between the original coatings is more distinct in the unbiased material than in the biased material. 6) There is a visible zone (about 100 nm thick) of small (few tens of nm) second phase particles at the coating/substrate interface; this is much more visible in the alloy deposited with a substrate bias. 7) Second phase particles are more uniformly distributed throughout the unbiased material than for the biased material.

SEM observations of microhardness indentations in the hot isostatic pressed material indicated that the material deforms plastically under compressive loading without cracking. There is also evidence that there is discontinuity in the yielding at the coating/substrate interface as evidenced by the rumpled appearance (caused by the slip lines) of the surface in this region. This type of distortion did not occur near all indents; so it is probably dependent on the local substrate grain orientation.

IV.C. TEM ANALYSES AND PHASE IDENTIFICATION

IV.C.1. AS-DEPOSITED SPECIMENS

Broad face TEM analyses of the as-deposited coatings indicated that the matrix and second phase morphologies are dependent on alloy composition and deposition bias. Representative micrographs of the structures observed for the as-deposited coatings are shown in figures 15-17] (biased, low Ta), 18-20 (biased, high Ta), 21 (unbiased, low Ta), and 22 and 23 (unbiased, high Ta). Microstructural details for the as-deposited alloys are discussed in the following paragraphs.

IV.C.1.a. BIAS DEPOSITED, LOW TANTALUM

For the microstructure of the bias deposited, low Ta alloys, significant features include:

- 1) The second phase particle sizes range from <10 nm to about 20 nm, as shown in figures 15

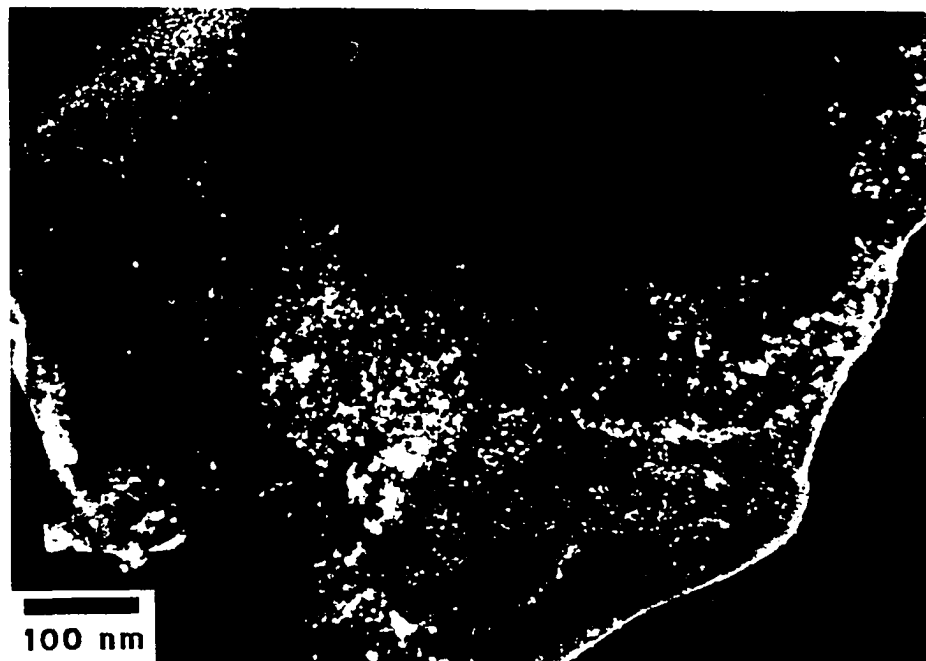


Figure 15. TEM dark field micrograph showing >10 nm second phase particles in as-deposited specimen {3,2} from run 18 (biased, low Ta).

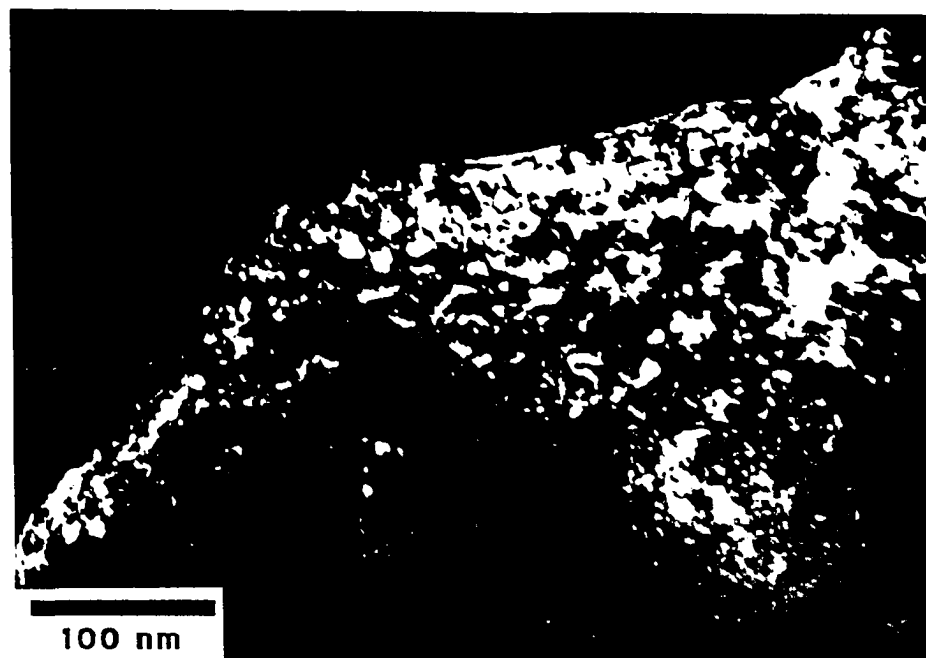


Figure 16. TEM dark field micrograph showing >10 nm second phase particles in as-deposited specimen {3,2} from run 18 (biased, low Ta).

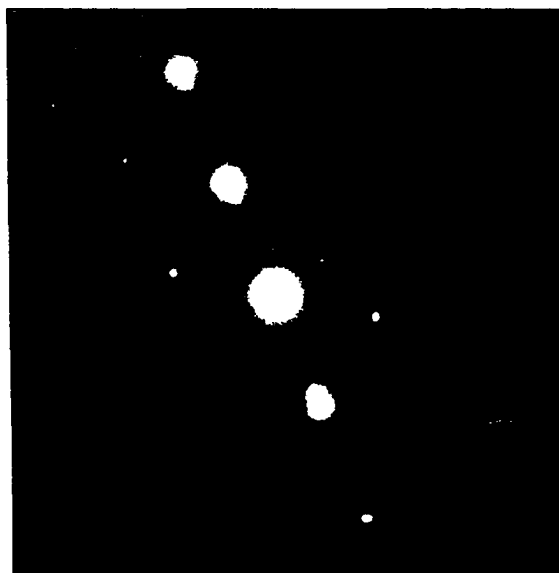
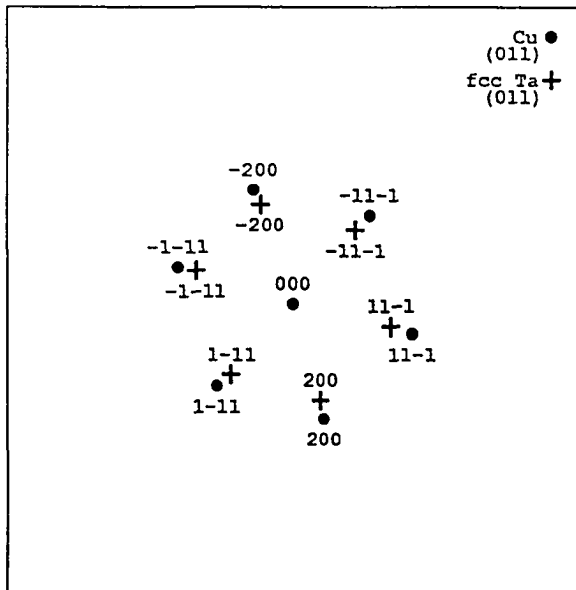


Figure 17. TEM electron diffraction pattern near Cu [011] zone and fcc Ta [011] zone of as-deposited specimen {3,2} from run 18 (biased, low Ta).

and 16. Most of the second phase particles are <10 nm in diameter and are clearly visible in these dark field TEM diffraction contrast images. The fraction of second phase particles in this bias deposited alloy which are larger than 10 nm is greater than that for the unbiased, low Ta alloys. 2) The electron diffraction pattern shown in figure 17 indicates the presence of fcc Ta. Other electron diffraction analyses show that bcc Ta and Ta-oxide are also present as part of the "second phase" in this biased, low Ta alloy. 3) The Cu matrix grains range in size from <100 nm to about a micron. The Cu grains are about the same size as the features observed in the SEM, indicating that each apparent grain viewed in the SEM (figure 5) is a single Cu grain, except for the large (about 1 micron) columnar structures where multiple matrix grains in a single column were often observed. 4) Second phase particle size varied randomly with location on the specimen and the magnitude of this variation, between 10 and 20 nm, was greater than that observed in figure 15. 5) The large numbers of second phase particles visible in the dark field images of individual Cu grains indicates a clear orientation relationship between the matrix and second phase.

IV.C.1.b. BIAS DEPOSITED, HIGH TANTALUM

The bias deposited, high Ta alloys have the following features: 1) The second phase particle dimensions range from <5 nm to >50 nm; the size distribution is large (essentially bimodal) and is spatially nonuniform, as shown in figure 18, a TEM dark field micrograph showing the second phase particles as white against the darker background of the matrix grains, and by comparing figures 18 and 19, a TEM dark field micrograph also showing white second phase particles. 2) The larger second phase particles have irregular shapes, figures 18 and 19. Contrast variations within individual particles suggest that the particles are heavily defected, although individual dislocations were not observed. 3) The second phase particles in this biased, high Ta alloy are generally larger than those in any of the other as-deposited materials. 4) Selected area electron diffraction analyses, figure 20, indicate that Ta is present in both the fcc and bcc forms in this alloy in the as-deposited condition. Electron diffraction

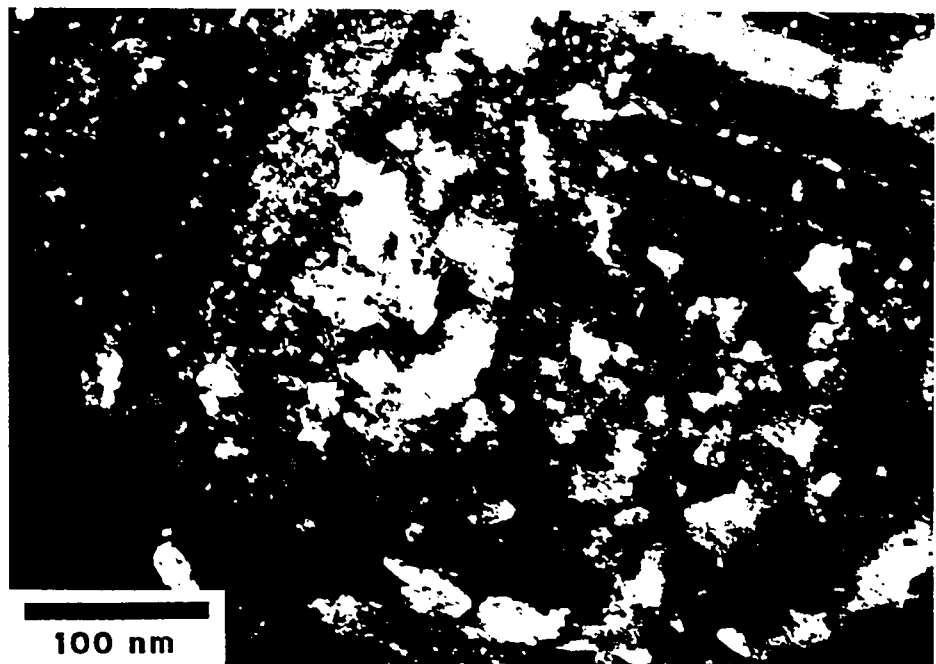


Figure 18. TEM dark field micrograph showing <20 nm second phase particles in as-deposited specimen {3,6} from run 18 (biased, high Ta).

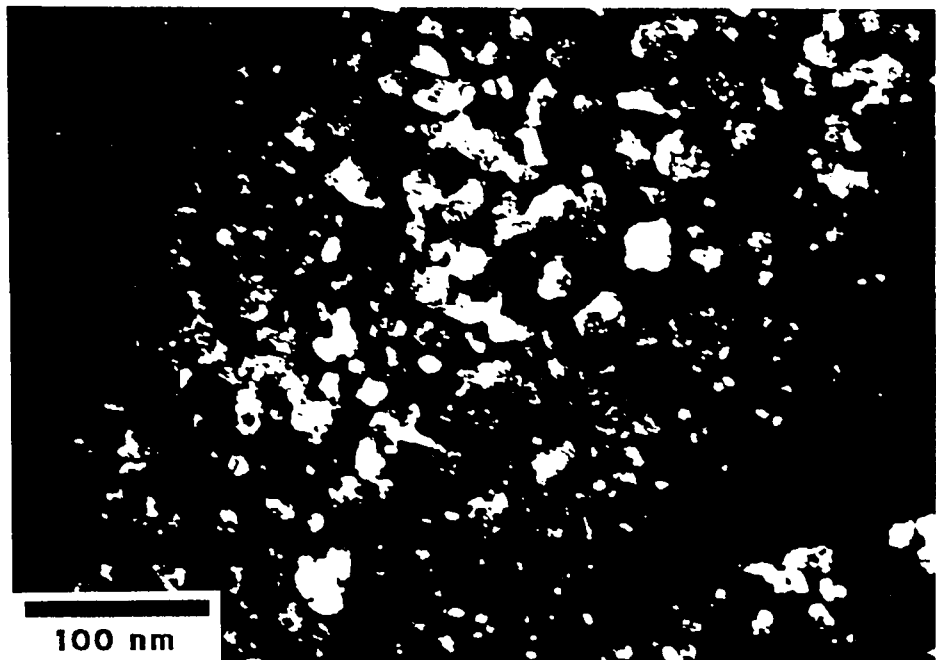


Figure 19. TEM dark field micrograph showing ~20 nm and <10 nm second phase particles in as-deposited specimen {3,6} from run 18 (biased, high Ta).

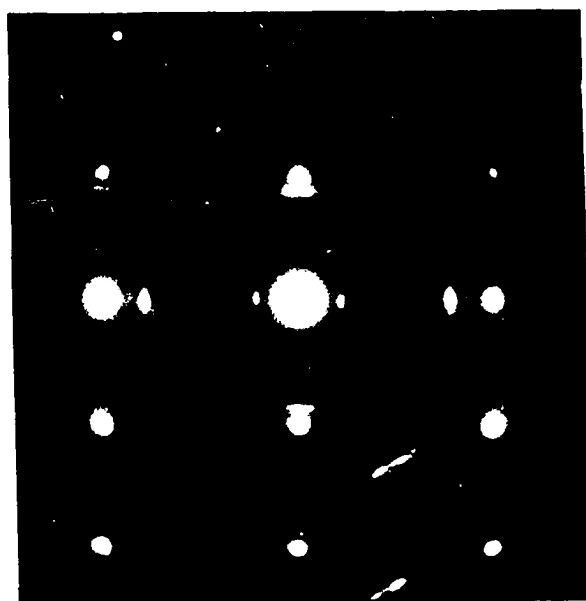
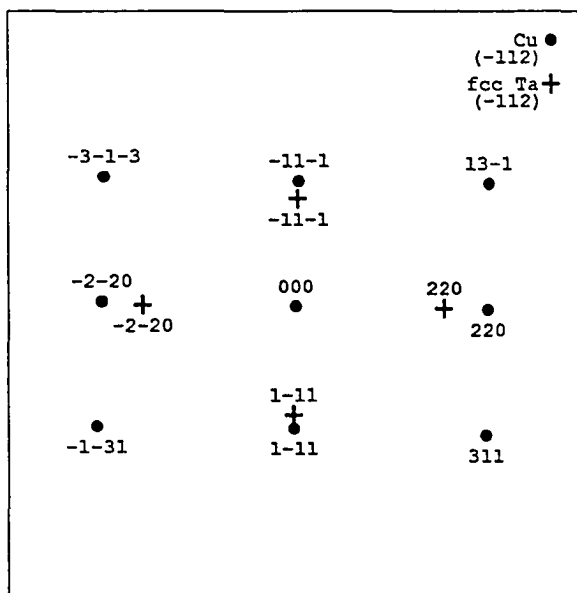


Figure 20. TEM electron diffraction pattern near Cu [-112] zone and fcc Ta [-112] zone of as-deposited specimen {3,6} from run 18 (biased, high Ta).

evidence for Ta oxide was found in other diffraction patterns. 5) The large number of second phase particles visible in the dark field image of this biased, high Ta alloy indicates that, as was found for the biased, low Ta alloy, a orientation relationships exists between the Cu matrix and the second phase particles. 6) As found for the biased, low Ta alloy, the Cu matrix grain size ranges from about 0.1 to 1 micron. These matrix grain sizes are also about the same as the feature dimensions observed in the SEM (figure 6), indicating that apparent individual grains viewed in the SEM are indeed single grains.

IV.C.1.c. UNBIASED, LOW TANTALUM

Features for the low Ta alloys deposited without substrate bias include: 1) The second phase particles in this alloy are, on average, smaller than those in the biased, low Ta alloy and the unbiased, high Ta alloy. 2) Matrix grain sizes ranged between approximately 40 and 350 nm. Figure 21 shows the dark field image of a grain about 150 nm in length. Under the imaging condition used, individual second phase particles are defined by Moire fringe patterns and are about ~10 nm in size. The approximate 300 nm upper limit in the matrix grain size is in agreement with the SEM results (figure 7). As shown by the TEM results, the granular structures observed in the SEM (figure 7) contain more than one grain. 3) The nonuniformity of second phase particle size and spatial distribution appears to be less in the unbiased, low Ta alloy than in the other as-deposited alloys. 4) The Moire fringe images of the second phase particles visible in figure 21 are consistent with a second phase/matrix orientation relationship. 5) Electron diffraction patterns indicate that fcc Ta, bcc Ta and Ta oxide are present.

IV.C.1.d. UNBIASED, HIGH TANTALUM

Microstructure features for the high Ta alloys deposited without substrate bias include: 1) The large (>15 nm) second phase particles found (figures 22 and 23) in this material were more numerous than in the unbiased, low Ta alloy (figure 21), about equal to the biased, low Ta

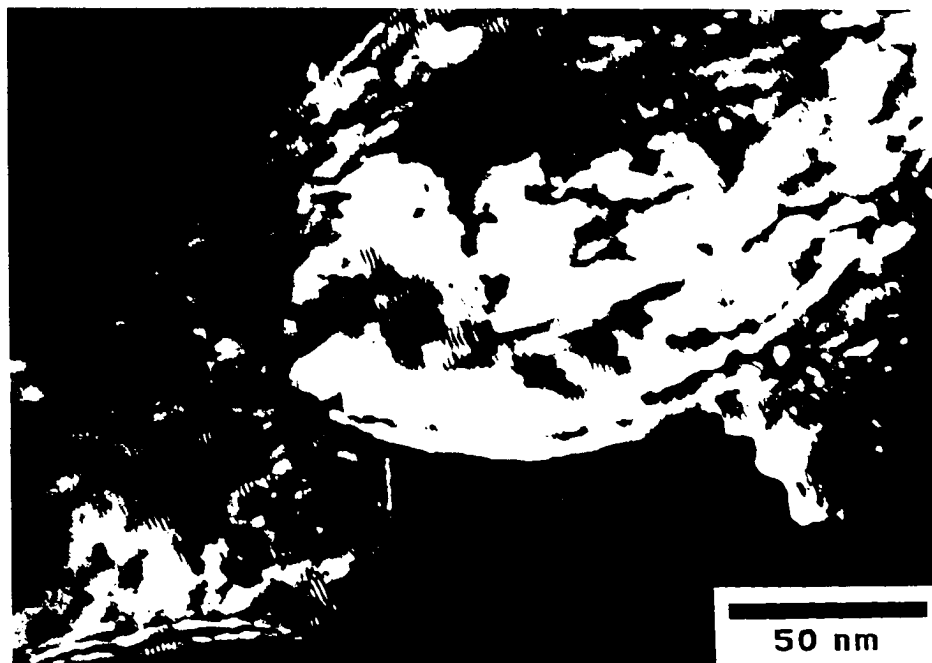


Figure 21. TEM dark field micrograph showing ~10 nm second phase particles visible by Moire fringes in as-deposited specimen {3,2} from run 23 (unbiased, low Ta).

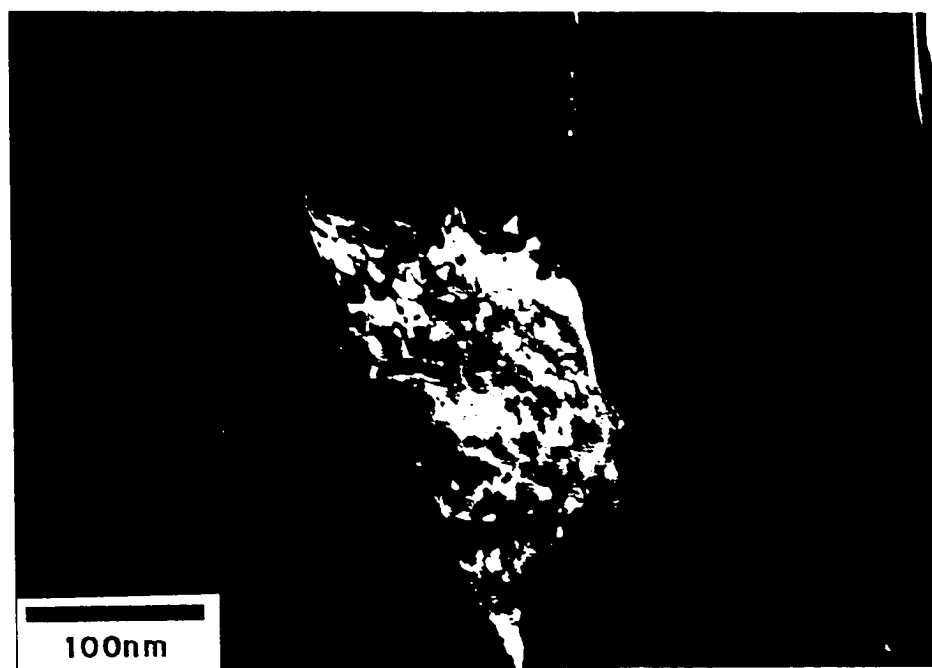


Figure 22. TEM dark field micrograph showing 10 - 20 nm second phase particles visible by Moire fringes in as-deposited specimen {3,6} from run 23 (unbiased, high Ta).

alloy (figures 15 and 16), and fewer than the biased, high Ta alloy (figures 19 and 18). In figure 22, a dark field TEM micrograph formed using both matrix and second phase diffracted beams, the second phase particles are defined by Moire fringes. The dark field micrograph in figure 23 shows the second phase particles as white spots on the darker matrix background. 2) Electron diffraction patterns indicate that fcc Ta, bcc Ta and Ta oxide are present. 3) The spatial nonuniformity of second phase particle sizes in the unbiased, high Ta alloy appears to be less than that in the biased, high Ta alloy. 4) The Cu matrix grain size for the unbiased, high Ta alloy agrees with that observed using SEM (figure 8) (50 to 300 nm).

Summarizing, significant microstructural features observed in the as-deposited coatings include: 1) All coatings exhibited some nanoscale second phase particles; in agreement with the x-ray results presented in a following section. 2) The second phase particles were more developed (a greater volume fraction of larger particles) in the coatings deposited with an rf substrate bias. 3) Increasing the Ta content of the alloys also caused the volume fraction of larger second phase particles to increase. 4) The sizes and spatial distribution of sizes of the second phase particles was nonuniform, with the greatest nonuniformities being for coatings deposited with a substrate bias. 5) Individual columnar structures visible in the SEM consist of assemblies of small, highly textured grains. 6) Electron diffraction patterns indicate that fcc Ta, bcc Ta, and Ta oxide are present. The relative proportions of these phases and the effects of processing on their respective existences are discussed later. 7) The Cu matrix grain size varied widely both within a single sample (point-to-point as well as top-to-bottom) as well as for samples with different compositions and deposition parameters. As a general trend and in agreement with the SEM results, with increasing Ta content the grain size variation increased for coatings deposited without a substrate bias and decreased for coatings deposited with a substrate bias.

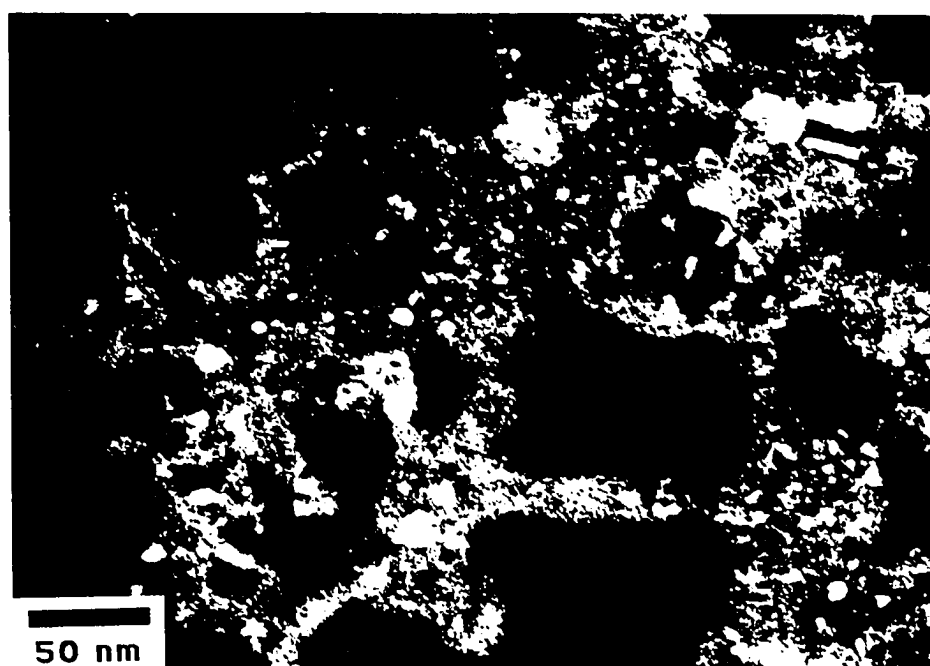


Figure 23. TEM dark field micrograph showing <10 nm second phase particles in as-deposited specimen {3,6} from run 23 (unbiased, high Ta).

IV.C.2. HEAT TREATED SPECIMENS

Broad face TEM analyses of the alloys after heat treatment indicated that the effects of heat treating on the matrix and second phase morphologies are strongly influenced by alloy composition and deposition bias. Micrographs of the structures observed for the heat treated coatings are shown in figures 24 -34 (biased, low Ta), 35 (biased, high Ta), 36 and 37 (unbiased, low Ta), and 38 (unbiased, high Ta). The microstructures for these heat treated alloys are discussed in the following paragraphs.

IV.C.2.a. BIAS DEPOSITED, LOW TANTALUM

Characteristics of the biased, low Ta alloys after heat treatment include: 1) The second phase particle diameters range from <10 nm to about 80 nm. Figure 24, annealed at 800 C for 1 hour, is a dark field micrograph which shows white second phase particles against the dark background of the Cu matrix. This figure shows particle sizes ranging from <10 nm to about 40 nm. It is important to note that individual second phase particles in the heat treated materials are more clearly defined than were particles in the as-deposited material. Annealing for longer times (up to 100 hours at 800 C, figure 25) or at higher temperatures generally increases the particle sizes, although point-to-point variations in particle size were commonly observed (figure 26). Figure 27, 900 C for 10 hours, shows mainly <10 nm particles in the outer portion of the grain and 20 nm particles in the grain center. This small outside/large inside particle size distribution was most frequently observed in the larger grains of the biased alloys after heat treatment. 2) The range in particle sizes from region-to-region within a single sample is increased by heat treating. As an example of this nonuniformity, large second phase particles were found on the Cu grain boundaries and small particles were found in the grain interiors after annealing a biased, low Ta alloy at 900 C for 1 hour, figure 28. 3) Faceted and rounded second phase particles were observed across the range of particle sizes, with no well defined size for transition from one form to the other. 4) The second phase particles in this annealed material consisted of fcc Ta, bcc Ta, and Ta oxide. The selected area electron diffraction

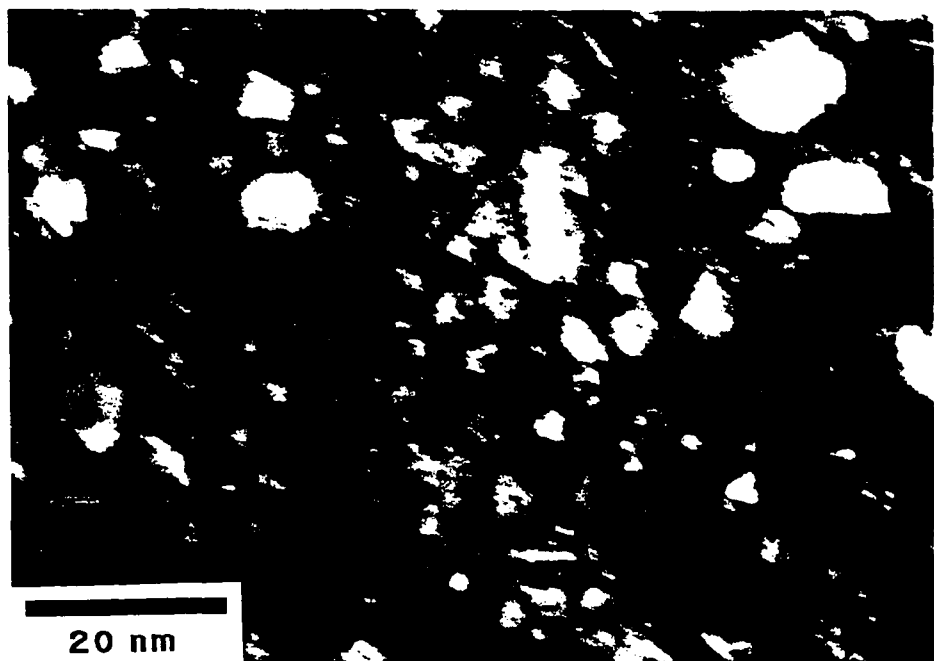


Figure 24. TEM dark field micrograph showing <10 nm second phase particles in specimen {2,2} from run 18 (biased, low Ta) after 1 hour at 800 C.

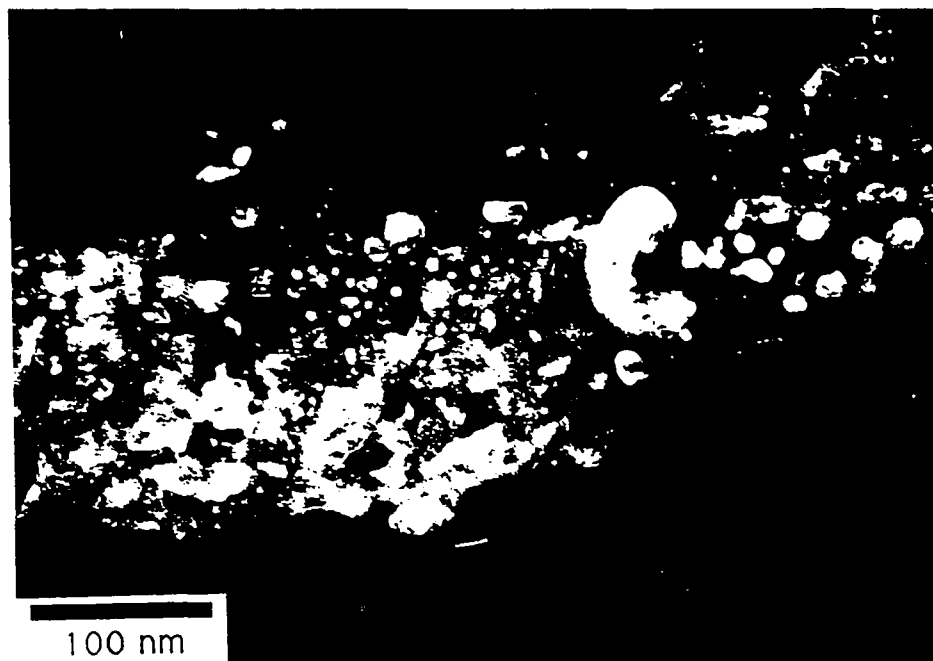


Figure 25. TEM dark field micrograph showing second phase particles in specimen {6,2} from run 18 (biased, low Ta) after 100 hours at 800 C.

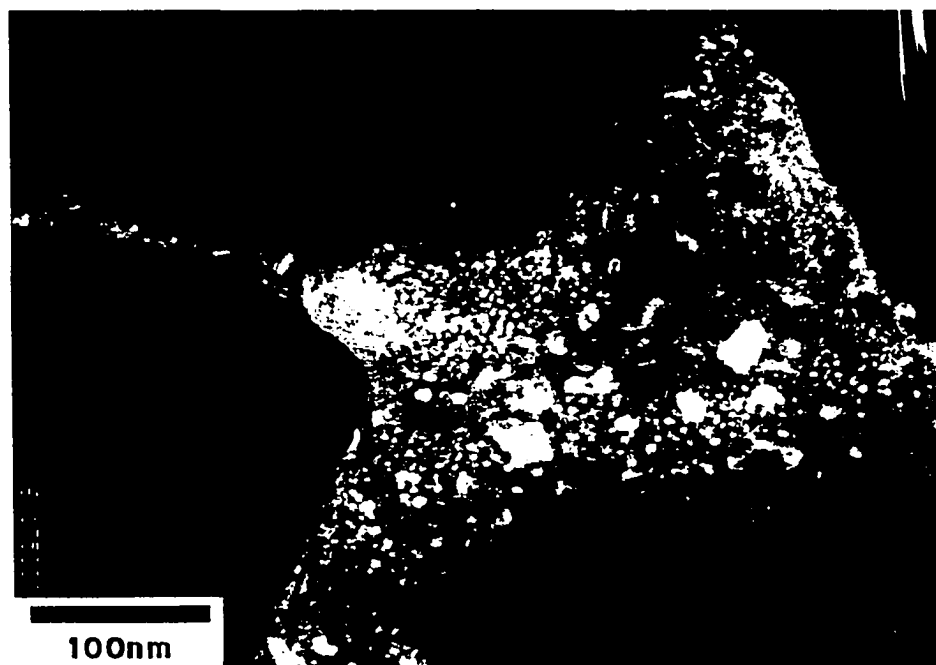


Figure 26. TEM dark field micrograph showing larger second phase particles superimposed on a background of >10 nm second phase particles in specimen {6,2} from run 18 (biased, low Ta) after 100 hours at 800 C.

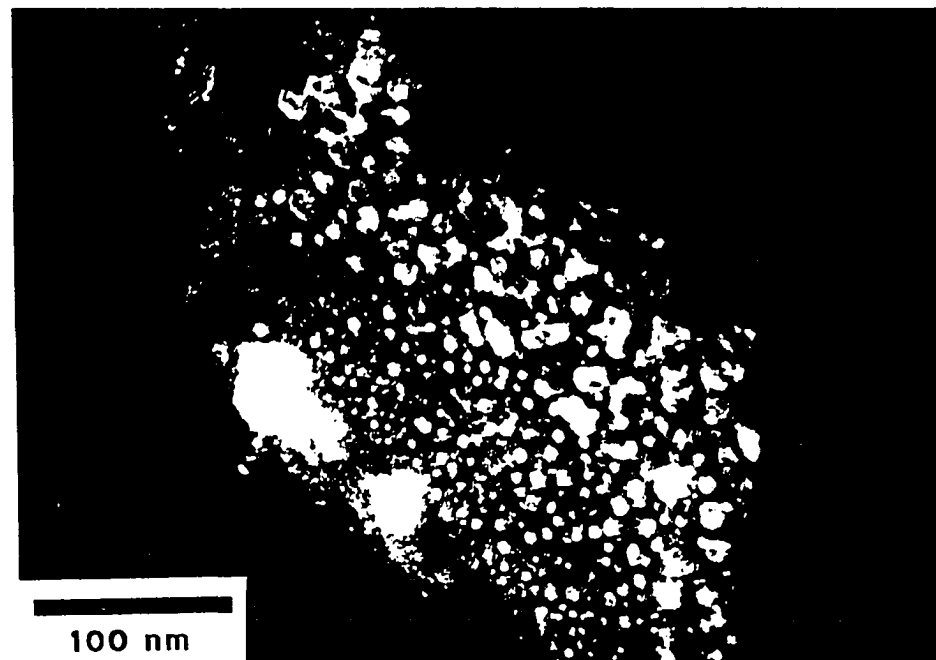


Figure 27. TEM dark field micrograph showing >10 nm second phase particles near the matrix edge and ~20 nm second phase particles in the matrix interior in specimen {5,2} from run 18 (biased, low Ta) after 10 hours at 900 C.

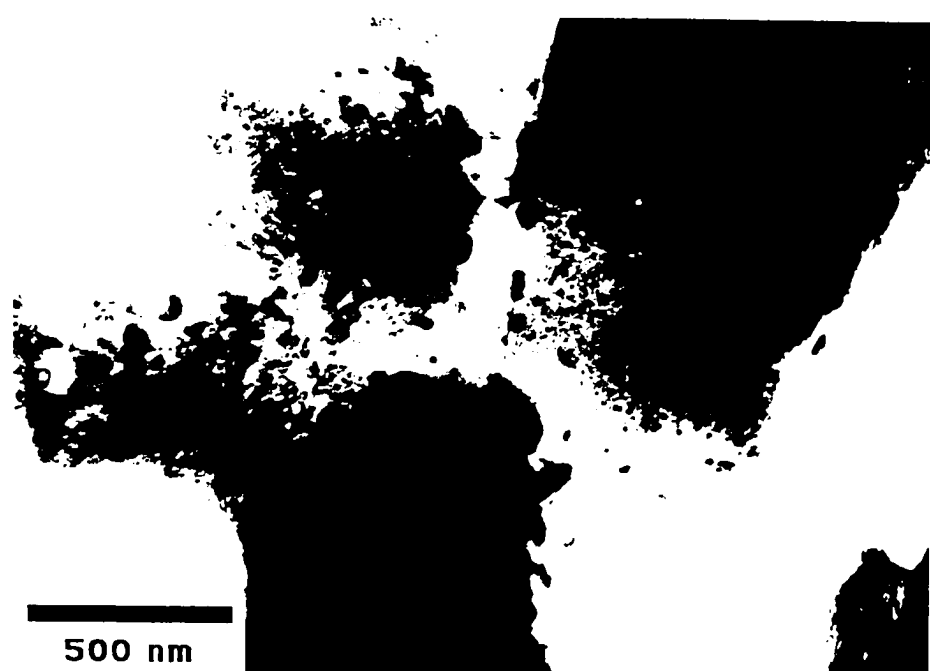


Figure 28. TEM bright field micrograph showing variations in second phase particle (visible as dark spots <120 nm) size between individual matrix grains and between the grain interiors and the grain boundaries in specimen {5,2} from run 18 (biased, low Ta) after 1 hour at 900 C.

pattern in figure 29 (800 C, 1 hour) shows a (112) Cu matrix foil orientation parallel to a (112) fcc Ta foil orientation. This and data to follow established clearly that much of the Ta exists in the fcc form and is oriented identically with the Cu matrix. In addition to fcc Ta, the (111) bcc spot pattern visible in this figure appears to indicate the presence of bcc Ta. Based on the indexing of figure 29, the orientation relationships are (11-1) fcc Cu // (11-1) fcc Ta // (01-1) bcc Ta and (2-20) fcc Cu // (2-20) fcc Ta // (2-1-1) bcc Ta. The (111) bcc Ta spot pattern does not follow the established fcc/bcc orientation relations of Nishiyama [78] and Wasserman [79] or Kurdjumov-Sachs [80]. Similar electron diffraction results are found in figure 30 (800 C, 1 hour), which shows the fcc Cu (-111) foil orientation parallel to the fcc Ta (-111) foil orientation, and in figure 31 (900 C, 1 hour), which shows (011) fcc Cu parallel to (011) fcc Ta. 5) The matrix grain sizes range from a few tens of nm to about a micron. The grain sizes are about the same as the feature dimensions observed by SEM indicating that each apparent grain as viewed in the SEM (figures 5 and 9) is a single grain. Large (~1 micron) columnar structures consisting of multiple matrix grains in a single column were often observed. 6) The TEM analyses were hindered with artifacts (nonuniform thinning and redepositing of sputtered material) created by interaction between the atom milling beam and the rough coating surfaces and voids. Figures 32 and 33 show an image and corresponding diffraction pattern for the polycrystalline material deposited in the recess between columns during atom milling of a biased, heat treated (800 C, 100 hours) low Ta alloy. Artifacts were avoided by working near the main hole and by recognition of redeposited material from the diffraction ring patterns. 7) The second phase particles were observed to interact with Cu matrix grain boundaries during heat treating. Figure 34, a dark field TEM micrograph using overlapping Cu and Ta reflections, provides an example of how the second phase particles inhibit boundary mobility. Careful examination of this 30 by 100 nm recrystallized Cu grain reveals a "stepped" grain boundary with sub-10 nm Ta particles at each step riser.

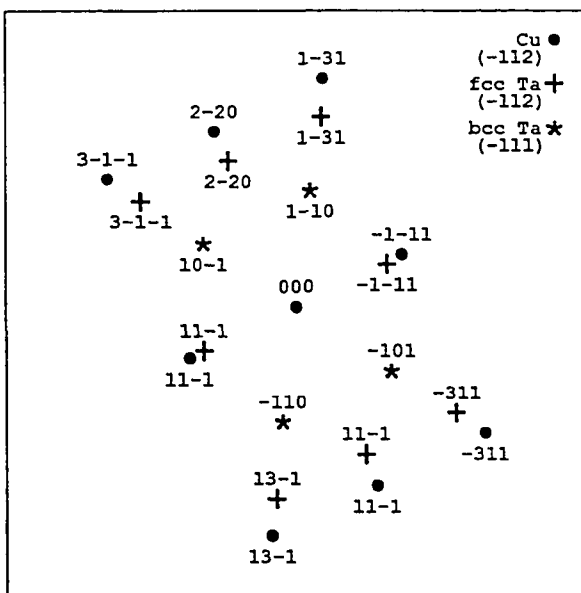


Figure 29. TEM electron diffraction pattern near Cu [-112] zone, fcc Ta [-112] zone and [-111] bcc Ta zone in specimen {2,2} from run 18 (biased, low Ta) after 1 hour at 800 C.

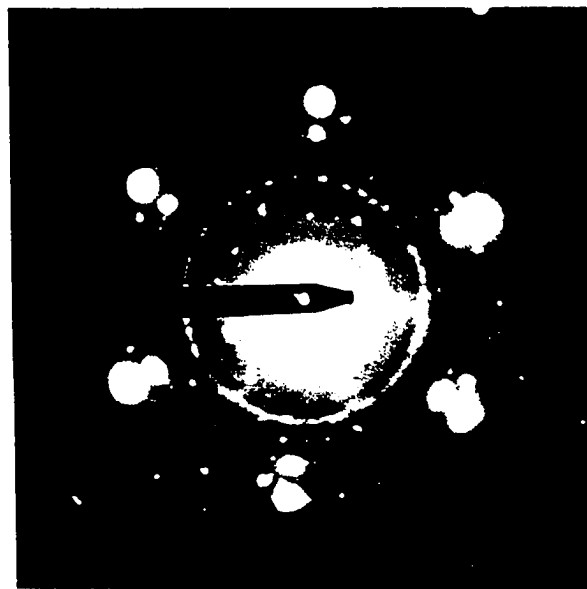
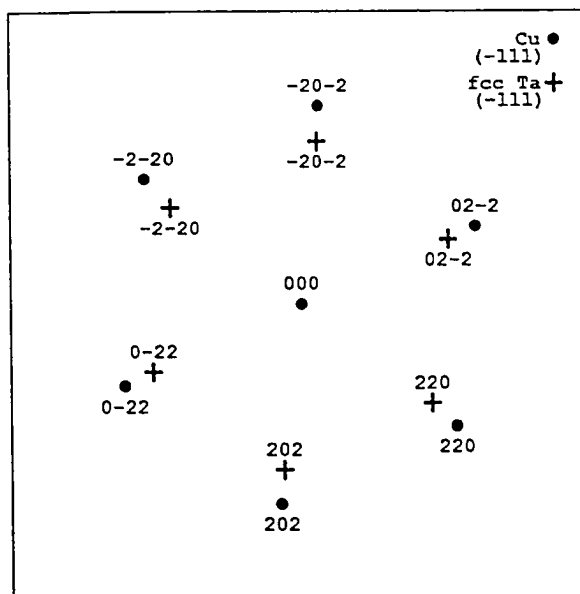


Figure 30. TEM electron diffraction pattern near Cu [-111] zone and fcc Ta [-111] zone in specimen {2,2} from run 18 (biased, low Ta) after 1 hour at 800 C.

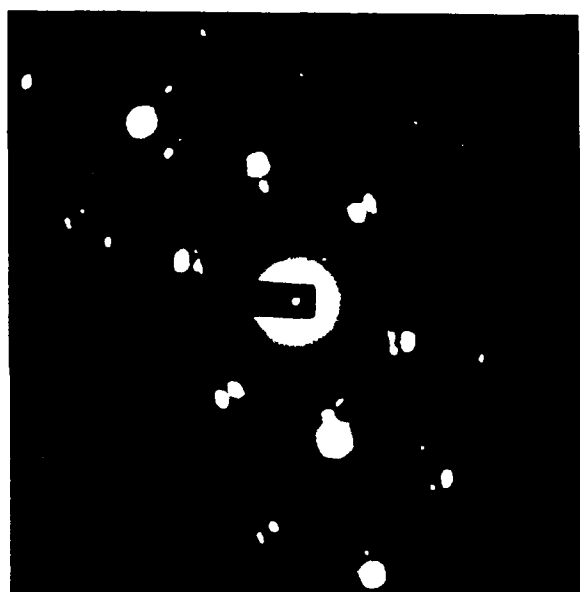
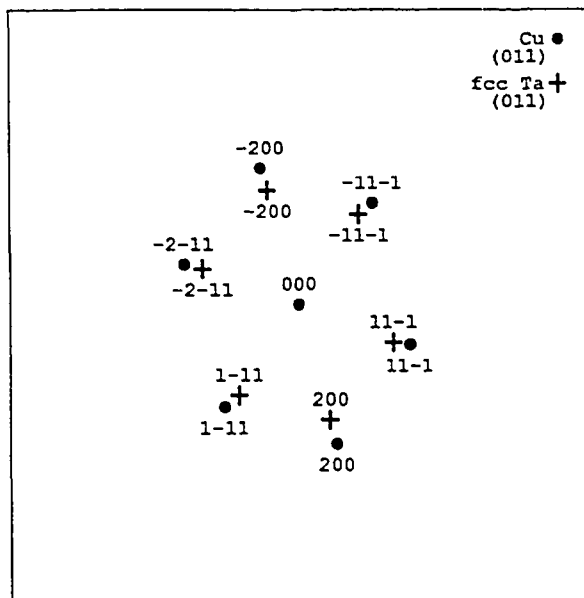


Figure 31. TEM electron diffraction pattern near Cu [011] zone and fcc Ta [011] zone in specimen {5,2} from run 18 (biased low Ta) after 10 hours at 900 C.

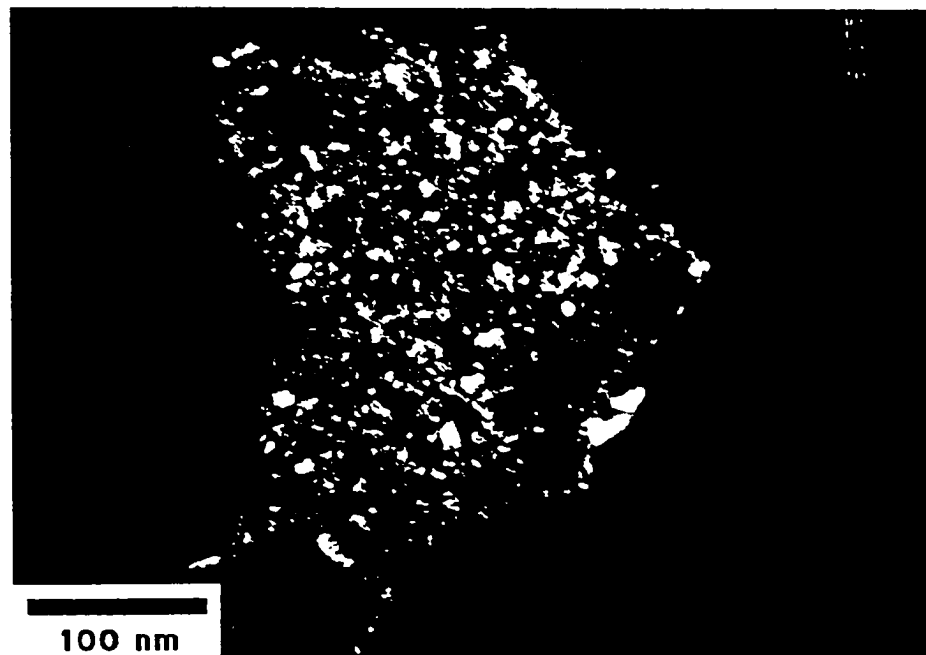


Figure 32. TEM dark field micrograph showing fine grained material redeposited in the shadowed recesses between columns during atom milling in specimen {6,2} from run 18 (biased, low Ta) after 100 hours at 800 C.



Figure 33. TEM electron diffraction pattern showing polycrystalline rings characteristic of the redeposited material shown in figure 32 from specimen {6,2} from run 18 (biased, low Ta) after 100 hours at 800 C. The numbered rings are: 1) (111) fcc Ta; 2) (200) fcc Ta; 3) (111) Cu; 4) (200) 200 Cu; 5) (220) fcc Ta; 6) (311) fcc Ta; 7) (220) Cu; 8) (311) Cu; and, 9) (222) Cu.



Figure 34. TEM dark field micrograph showing a recrystallized matrix grain with surface steps associated with several <10 nm second phase particles in specimen {6,2} from run 18 (biased, low Ta) after 10 hours at 800 C.

IV.C.2.b. BIAS DEPOSITED, HIGH TANTALUM

The microstructures of the heat treated, biased, high Ta alloys were similar to those for the heat treated, biased, low Ta alloys discussed above. Significant features include: 1) The second phase particle diameters range from <10 nm to about 80 nm with both faceted and rounded particle shapes. The primary difference between the low and high Ta heat treated alloys is that the high Ta alloys have a larger second phase volume fraction and particles at the large end of the distribution are more frequently observed. 2) The range of second phase particle sizes is again broader after heat treatment. Nonuniformity in second phase particle sizes, very few of the large (greater than 20 nm) second phase particles are observed at the outer edges of the grains, was observed in these alloys after heat treatment. 3) Both faceted and rounded second phase particles were observed, with approximately equal frequency, across the range of particle sizes. The tendency for forming faceted particles in the biased alloys appeared to decrease with increasing Ta. 4) Structure analyses using selected area electron diffraction indicated that the second phases consisted of fcc and bcc forms of Ta. Diffraction patterns showing these phases were presented in the previous section. As previously stated for the biased, low Ta alloy, the fcc Ta is oriented identically with the fcc Cu matrix. 5) The Cu matrix grain sizes observed using TEM range from a few tens of nm to about a micron. This result agrees with the SEM results (figures 6 and 10) for the as-deposited, heat treated materials. TEM results on the Cu matrix show that what appears as individual grains in the SEM are indeed individual grain. TEM results further show that the large, columnar structures observed in the SEM micrographs consist of multiple matrix grains in a single column. 6) Thickness variations associated with the columnar morphology of the as-deposited alloy coating lead to nonuniform specimen thicknesses after atom milling. Figure 35 shows a low magnification bright field TEM image of one of the heat treated, biased, high Ta alloys after atom milling from the substrate side. The dark regions are the remnants of the columnar structures observed for the biased alloys in the SEM. From the appearance of the narrow necks joining the individual columns, it is evident that the individual columnar structures generally detach themselves from the

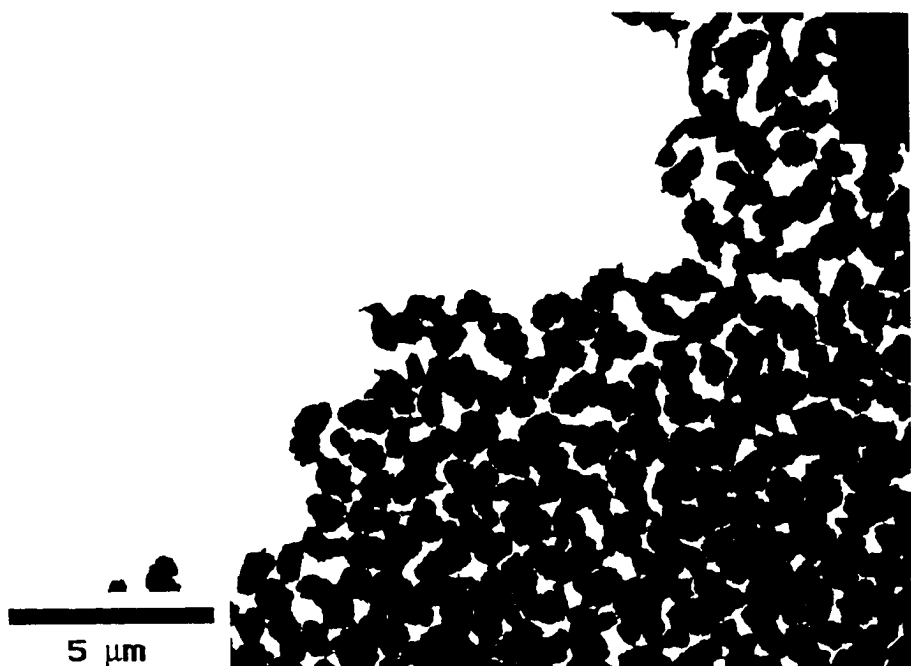


Figure 35. TEM low magnification bright field micrograph showing the lace like appearance of the columnar structure after atom milling in specimen {5,6} from run 18 (biased, high Ta) after 1 hour at 900 C.

specimen during atom milling as the supporting substrate and coating at the base of the columns is milled away. Unfortunately, this often occurs before the columnar structures themselves are thinned sufficiently for electron transparency. This "lacy" appearance of the alloy coating was apparent to some degree in all of the atom milled, nonconsolidated alloy coatings but was most prominent for alloys deposited with substrate bias because of their more columnar nature.

IV.C.2.c. UNBIASED, LOW TANTALUM

The microstructure of the heat treated, unbiased, low Ta alloys was very similar to that of the heat treated, biased alloys, with the only major difference being that this material appeared to have more of the larger (greater than 20 nm) and fewer of the smaller (less than 10 nm) second phase particles in some regions. Significant features of the heat treated, unbiased, low Ta alloys determined using TEM include: 1) The second phase particle diameters range from <10 nm to about 80 nm, as shown in figures 36 and 37. Figure 36 (800 C, 10 hours) is a dark field micrograph showing high densities of large (>20 nm) and small (<10 nm) second phase particles. Figure 37 (800 C, 100 hours), also a dark field micrograph, showing rounded, faceted, and irregularly shaped nature of the larger second phase particles. The imaging conditions used for figure 37 less effectively showed the very small second phase particles but it is noted that the density of these sub-10 nm particles had decreased as a result of the 10x increase in annealing time. Figure 37 also shows an artifact arising from the difference in sputter yield between the Cu matrix and the Ta-rich second phase particles. The higher sputter yield matrix has been milled away, leaving a hole (~80 nm diameter) most of the way around one of the larger (~25 nm diameter) low sputter yield Ta-rich particle. In figure 37, also note the projections associated with the near edge second phase particles further indicating preferential milling of the Cu matrix. 2) Similar to the biased alloys, the range of second phase particle sizes in this material increases as a consequence of heat treatment. Variations in the second phase particle sizes between the interior and exterior regions of the larger grains in this annealed, unbiased, low Ta alloy were not as pronounced as in the annealed,

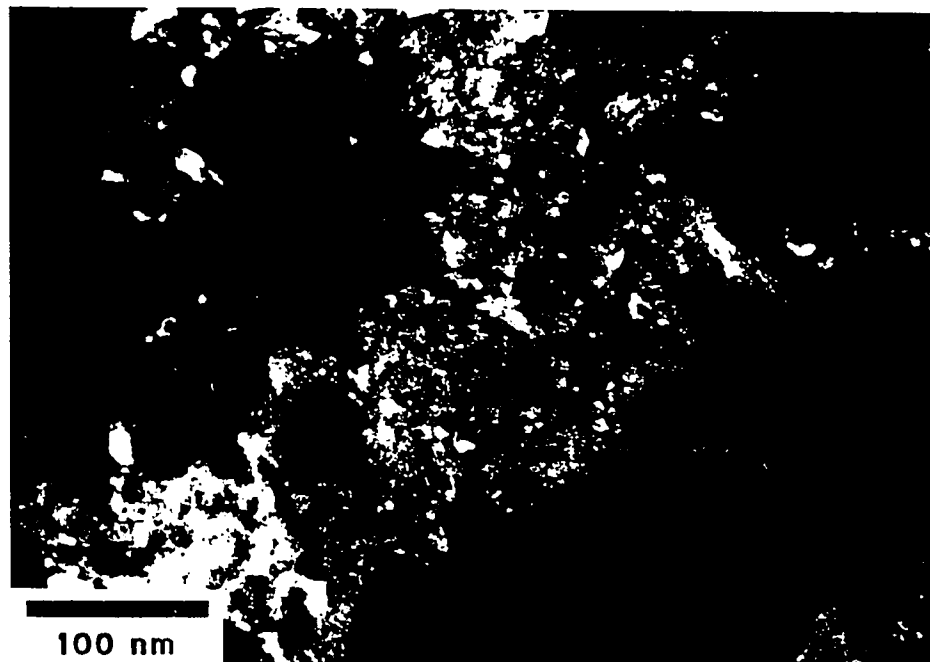


Figure 36. TEM dark field micrograph showing <10 nm second phase particles in specimen {6,2} from run 23 (unbiased, low Ta) after 10 hours at 800 C.

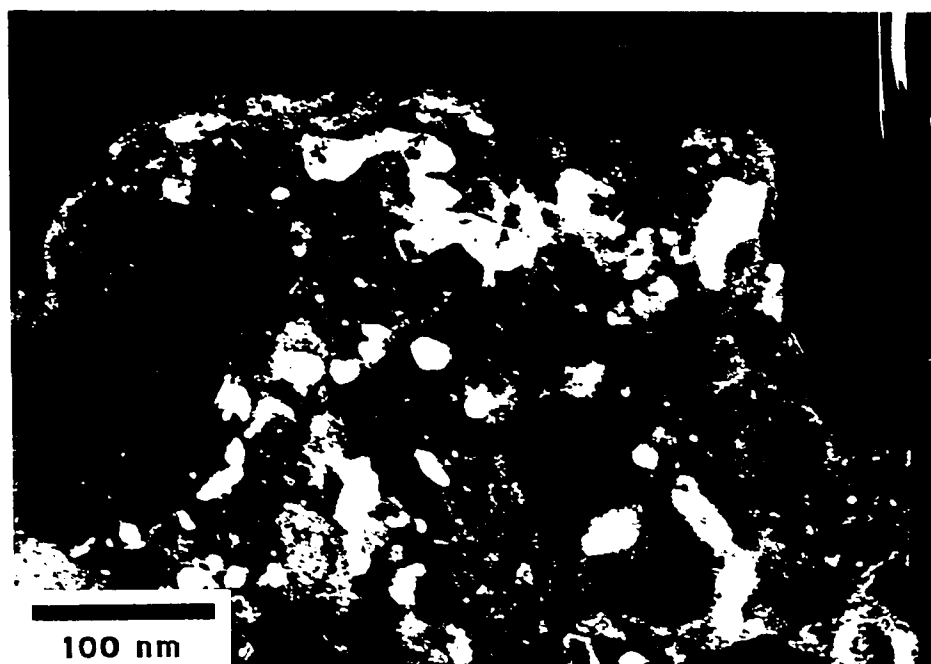


Figure 37. TEM dark field micrograph showing rounded, faceted, and irregularly shaped ~20 nm Ta particles in specimen {6,2} from run 23 (unbiased, low Ta) after 100 hours at 800 C.

biased alloys. 3) Both faceted and rounded second phase particles were observed across the range of particle sizes, with no well defined size for transition from one form to the other. Considering identically annealed biased/unbiased and high/low Ta alloys, this alloy had a largest volume fraction of faceted particles. 4) Electron diffraction analyses indicate that the second phase is fcc Ta. (Note that the x-ray diffraction results presented in a later section indicate that bcc Ta and Ta oxide are also present.) The fcc Cu matrix and fcc Ta particles are also identically oriented for this annealed alloy. 5) The Cu matrix grain sizes range from a few tens of nm to about a 500 nm, in agreement with SEM observations as shown in figures 7 and 11. The maximum Cu grain size in this material is smaller than that of the identically annealed, biased alloys. TEM and SEM results show that the contact areas between individual grains in the as-deposited alloy increased as a result of annealing, e.g., some sintering occurred. This increased bonding between individual grains resulted in improved ductility for the fractured specimens. 6) This unbiased, low Ta alloy appeared to have the smallest amount of atom milling-induced surface artifacts, probably because this alloy and deposition condition (no bias) produced the smoothest and most dense coating.

IV.C.2.d. UNBIASED, HIGH TANTALUM

The unique microstructural feature for the heat treated, unbiased, high Ta alloys was its small second phase particle size. In contrast with the biased alloys where increasing Ta content produced larger particles, increasing Ta in the unbiased alloys was found to decrease the second phase particle size. Significant features of the TEM analyses of the heat treated, unbiased alloys include: 1) The second phase particle diameters range from less <10 nm to ~60 nm. This heat treated, unbiased, high Ta alloy appeared to have fewer second phase particles in the upper half of the size range than did any of the other heat treated alloys. 2) Similar to the other heat treated alloys, the range of second phase particle sizes is again broader after heat treatment than in the as-deposited material. Variations in the second phase particle sizes between the interior and exterior of the larger grains in this heat treated, unbiased, high Ta alloy were not

as pronounced as in the heat treated alloys deposited with substrate bias. 3) Both faceted and rounded second phase particles were observed across the range of particle sizes with no well defined size for transition from one form to the other, in agreement with the other heat treated alloys. 4) Selected area electron diffraction analyses indicate the presence of fcc Ta, with this phase oriented identically with the Cu matrix. 5) TEM observations gave Cu matrix grain sizes in agreement with the SEM results (figures 8 and 12), with a maximum grain size of about 500 nm and some grains as small as a few tens of nm. TEM examinations of small polycrystalline features, such as shown in figure 38, suggests that SEM analyses may not be able to identify the actual grain size of nanocrystalline particles.

In summary, significant features of the structures observed in the heat treated coatings include: 1) The particle size distribution is very nonuniform, with the greatest nonuniformity being for biased alloys. 2) Both faceted and nonfaceted second phase particles were observed for the full range of second phase particle sizes. The tendency for particle faceting may be an effect of the oxygen content of the coatings and will be considered in the discussion section. 3) The larger second phase particles observed for the longer heat treatments coexist with a background of smaller particles, especially in biased coatings. This situation is visible in figure 26. 4) The largest second phase particles were most often seen in large, less voided Cu matrix grains. In these large Cu grains, the small second phase particles were more numerous near the grain edges while the large second phase particles were more numerous near the grain centers. This effect, visible in figure 27, was most often associated with grains in the large columnar structures for biased alloys. 5) The second phase particles appeared able to "pin" recrystallized Cu matrix grains, as seen in figure 34. 6) There is evidence for the formation of artifacts during ion milling due to surface roughness, which causes the redeposition of sputtered material into shadowed areas, and differences in the sputter yield between the matrix and second phase, which results in preferential removal of the matrix material near the larger second phase particles. The surface roughness also gives rise to a lace-like appearance of the thinned specimens as seen in figure 35. These artifacts were avoided by working close to the

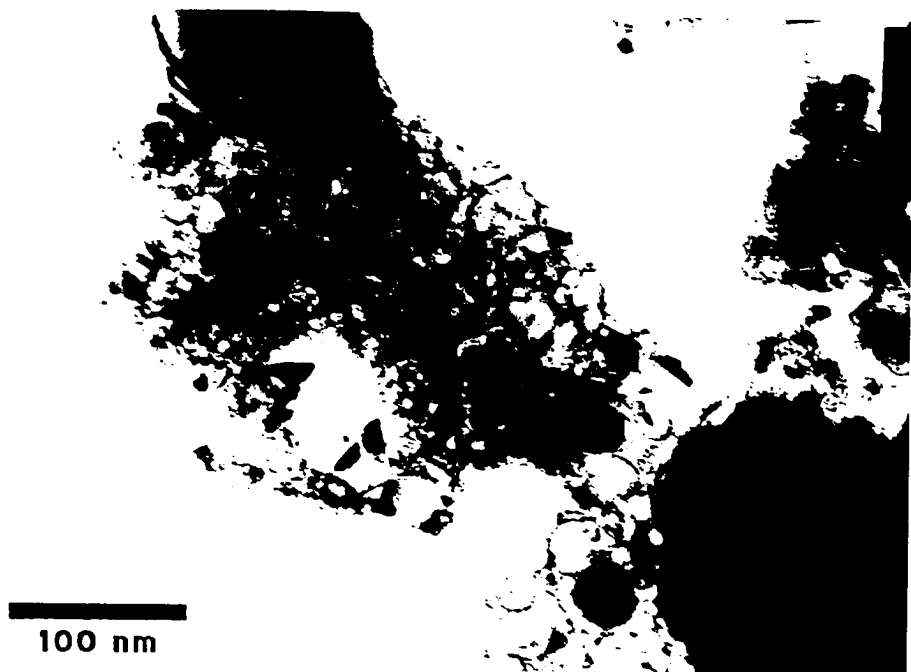


Figure 38. TEM bright field micrograph showing polycrystalline nature of small (<100 nm) matrix features in specimen {2,6} from run 23 (unbiased, high Ta) after 1 hour at 800 C.

main hole and away from thick regions which could cause redeposition of sputtered material due to "shadowing". The problem of redeposited material is recognizable by its characteristic diffraction ring pattern.

IV.C.3. HOT ISOSTATIC PRESSED SPECIMENS

Cross section TEM analyses of hot isostatic pressed specimens indicated that the consolidated microstructure is dependent on the coating deposition parameters. Representative micrographs for the structures observed in the HIPped specimens are shown in figures 39 and 40 (unbiased, high Ta) and figures 41 - 43 (biased, high Ta). Details for the HIPped alloys are discussed in the next few paragraphs.

For the microstructures of the HIPped, unbiased alloy: 1) The second phase particle sizes range from <20 nm to ~400 nm, in agreement with the SEM results for the same material as shown in figure 14. Figure 39 is a dark field micrograph of the HIPped, unbiased alloy with several Cu matrix grains about 400 nm in size illuminated. Several of the ~100 nm Ta particles are visible at the specimen edges where the surrounding higher sputter yield Cu matrix has been preferentially removed by atom milling. A large number of small (<20 nm) second phase particles are visible as white specks in the moderately illuminated matrix grains. Figure 40, a bright field micrograph of the same specimen shown in figure 39, displays the large (~100 nm) Ta particles as dark shapes against a light background. This particle contrast results from both diffraction contrast and the lower electron transparency of Ta relative to Cu. 2) This HIPped alloy has more large second phase particles (>100 nm) and fewer small second phase particles (<50 nm) than the HIPped, biased alloy. 3) The large second phase particles were rounded with some facets. The small second phase particles had shapes like those in the material heat treated without applied stress. 4) The Cu matrix grain size is typically between 300 to 600 nm and corresponds strongly to the local spacing between the large second phase particles. The large second phase particles appear effective at inhibiting matrix grain growth. 5) Preferential sputter removal of the higher sputter yield Cu matrix is visible in figures 39

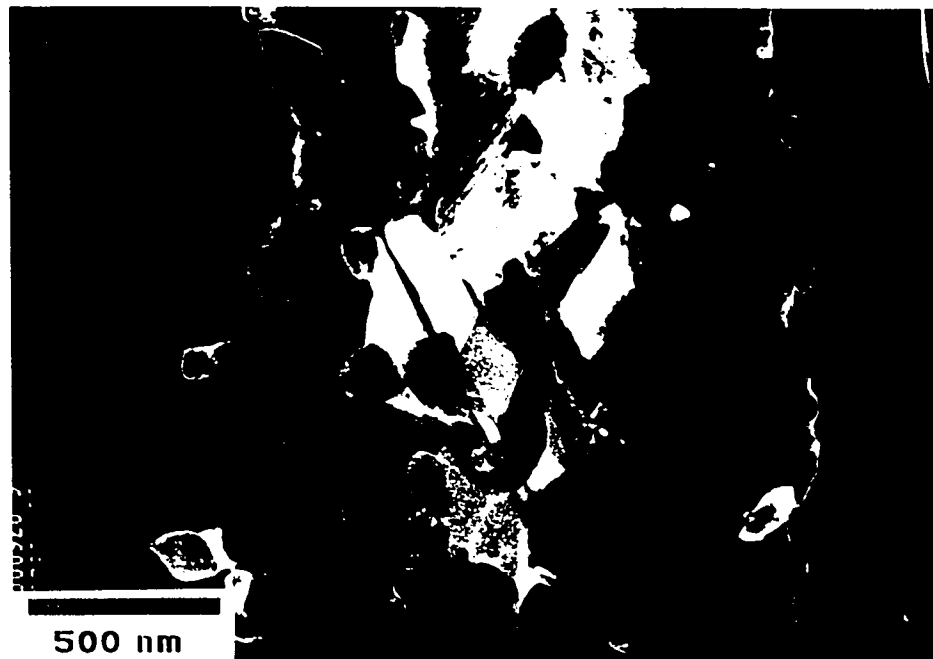


Figure 39. TEM dark field micrograph showing ~400 nm faceted matrix grains and ~100 - 200 nm rounded Ta particles in specimen {3,2} from run 20 (unbiased, high Ta) after HIP 1 hour at 900 C and 172 MPa.

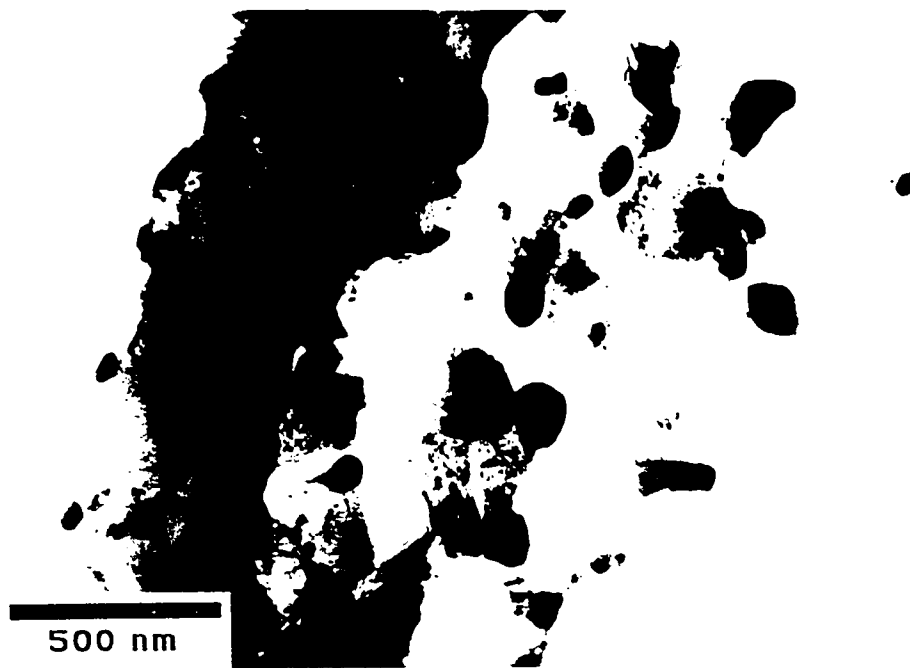


Figure 40. TEM bright field micrograph showing ~100 - 200 nm Ta particles, as dark due to diffraction contrast and the lower electron transparency of Ta relative to Cu, in specimen {3,2} from run 20 (unbiased, high Ta) after HIP 1 hour at 900 C and 172 MPa.

and 40 by the second phase particles extending from the specimen edge. 6) The difference between this HIPped alloy and the encapsulated and heat treated alloys is due to the mechanical nature of the HIP process. A sample of this alloy was encapsulated and heat treated for 1 hour at 900 C and the structures were indistinguishable from the previously presented annealed alloys.

For the microstructures of the HIPped, biased alloy , significant features include: 1) The second phase particle sizes range between 10 and 300 nm, in reasonable agreement with the SEM observation (figure 13) of a maximum second phase particle size of ~400 nm for the same material. Figure 41, a TEM dark field micrograph, shows a number of ~20 nm second phase particles with a background of sub-10 nm particles. This is very similar to the particles observed for the annealed alloys. Figure 42, a bright field TEM micrograph, shows 20 -50 nm second phase particles along 50 - 300 nm Cu matrix grain boundaries. In addition, the grain interiors contain many small (<10 nm) second phase particles. 2) This HIPped alloy has fewer of the large second phase particles (>100 nm) and more small second phase particles (<50 nm) than did the HIPped, unbiased alloy. 3) This HIPped alloy has a large number of ~20 nm second phase particles at the Cu grain boundaries, as discussed above for figure 42. 4) The Cu matrix grain size ranges from ~50 to >300 nm, with a typical size of about 250 nm. The 20-50 nm second phase particles occur largely at the Cu grain boundaries and appear effective at inhibiting matrix grain growth. 5) The HIPped alloy has a lower average sputter yield than the Cu substrate. This is dramatically shown in figure 43, a very low magnification TEM image, where the slower milling consolidated coating projects into the void where the Cu substrate was milled away. 6) The difference between this HIPped alloy and the encapsulated and annealed alloys is, again, due to the HIP process. Annealing a sample at 900 C for 1 hour, the structures were indistinguishable from the other correspondingly encapsulated and annealed alloys; this result is identical to the comparison made for the HIPped, unbiased alloy.

Significant microstructural features of the HIPped specimens may be summarized as follows. 1) The largest second phase particles in the HIPped specimens were larger than those observed for any of the other heat treated specimens. Correspondingly, the Cu grain size was

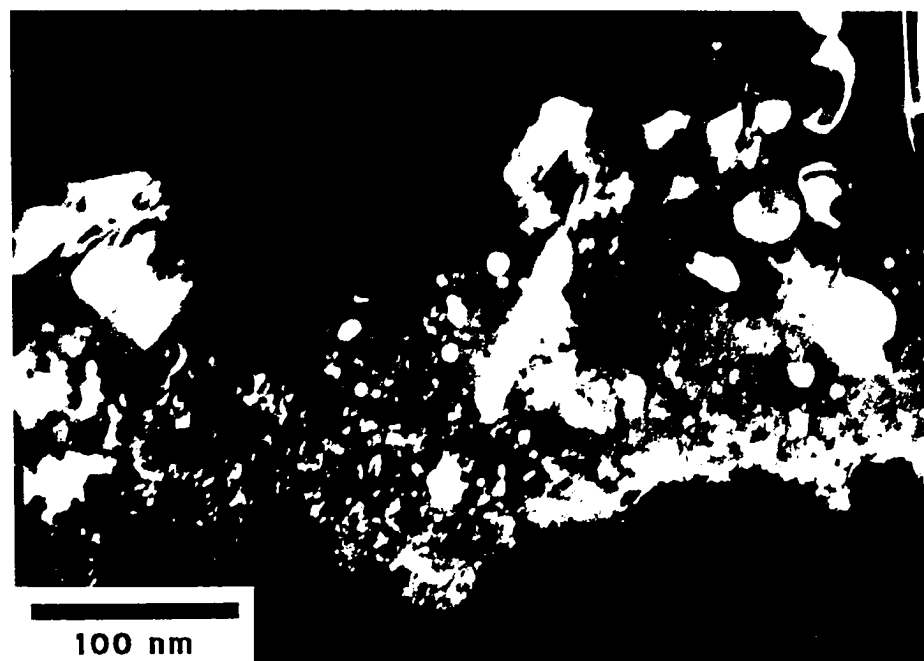


Figure 41. TEM dark field micrograph showing several <20 nm second phase particles on a background of <10 nm particles in specimen {3,2} from run 19 (biased, high Ta) after HIP 1 hour at 900 C and 172 MPa.

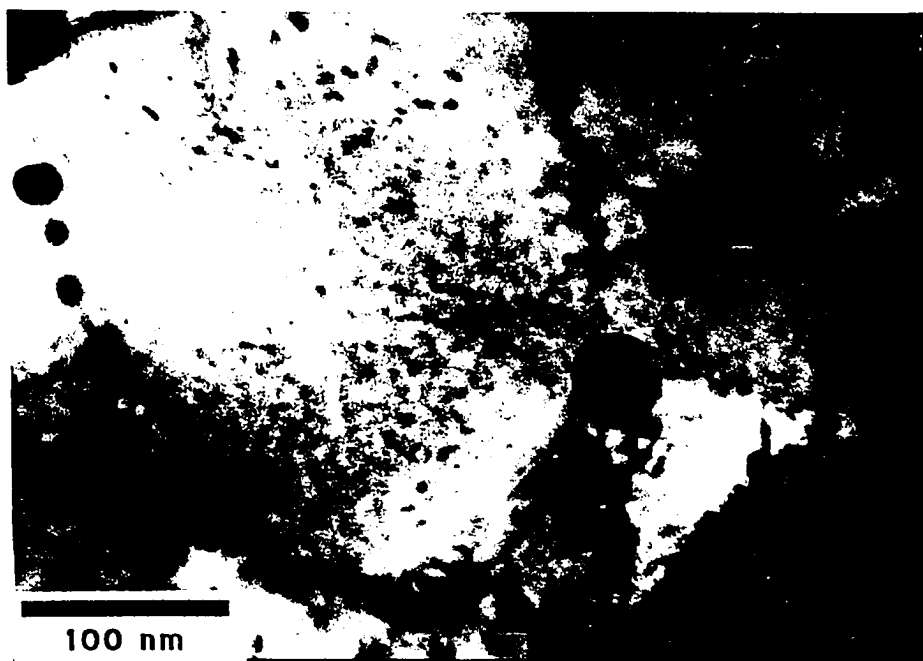


Figure 42. TEM bright field micrograph showing 20 - 50 nm Ta particles at the boundaries of 50 - 300 nm matrix grains and <10 nm second phase particles at the grain interiors in specimen {3,2} from run 19 (biased, high Ta) after HIP 1 hour at 900 C and 172 MPa.



Figure 43. TEM low magnification bright field micrograph showing the slow milling coating material projecting out of the relatively fast milling substrate material in specimen {3,2} from run 19 (high Ta, bias) after HIP 1 hour at 900 C and 172 MPa.

also larger in the HIPped specimens. 2) The Ta rich particles in the alloys deposited without ion bombardment are generally larger than those in the alloys deposited with ion bombardment. 3) Very fine (sub-20 nm)particles are present in HIPped specimens, as observed in figure 41. However, the biased alloy contained a greater volume fraction of small second phase particles after HIPping than did the unbiased alloy. 4) The larger Ta rich particles in the biased alloys were observed to have nearly spherical form (although some facets are visible) and were located preferentially on the Cu grain boundaries, as shown in figure 42. These larger particles appear effective at inhibiting grain growth of the Cu matrix. 5) The differences in sputter yield between Cu and the Cu-Ta coating or individual Ta particles are apparent, respectively, in figures 43 and 39. 6) The largest Ta rich particles in the unbiased alloys had a size approximately one-half that of the Cu grain size and appeared effective at inhibiting Cu grain growth. Similar to the biased alloys, the larger particles were nearly spherical, with some facets, and were located on the Cu grain boundaries. 7) Annealing specimens with time and temperature parameters similar to those for HIPping resulted in structures different from those observed for the HIPped specimens.

IV.D. X-RAY DIFFRACTION

A representative x-ray diffraction (XRD) intensity versus 2Θ (background subtracted) scan for the as-deposited alloys is shown in figure 44 (261801) for the biased, low Ta alloy. The broad diffraction peak centered at 38.5 degrees is the only Ta peak ($\{110\}$ bcc Ta) visible for as-deposited coatings. The remainder of the peaks in this figure are from the Cu matrix and substrate.

XRD scans representative of the heat treated alloys are shown in figures 45 (522305) and 46 (622303). It is important to note that the low Ta specimens used for figures 45 and 46 were essentially identical, in the as-deposited condition, because they came from side-by-side (along an iso-composition contour) substrate holder locations from the same deposition run. Comparing these figures, figure 45 (900 C, 10 hours) shows a taller and narrower Ta (110)

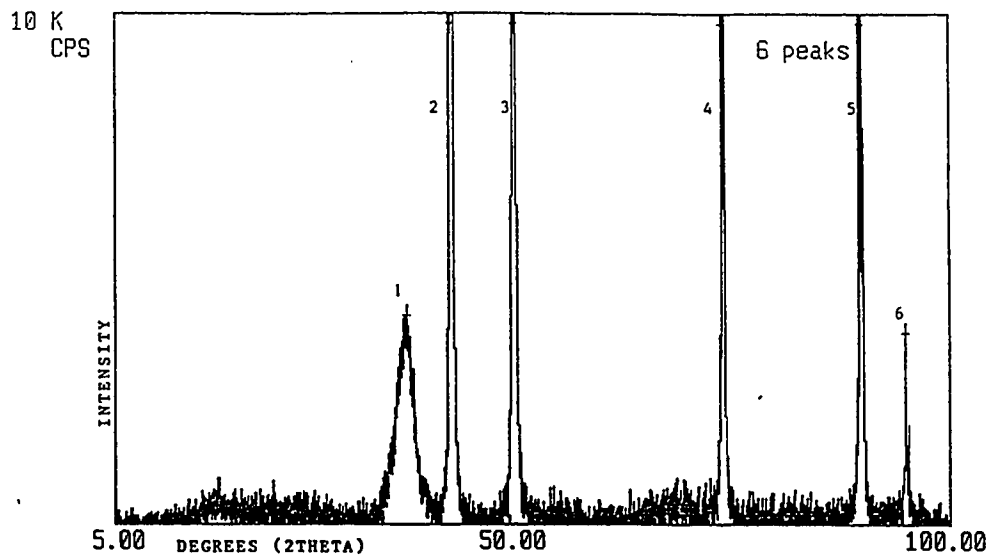


Figure 44. X-ray diffraction scan of as-deposited specimen {2,6} from run 18 (biased, high Ta). Numbered peaks correspond to: 1) (110) bcc Ta; 2) (111) Cu; 3) (200) Cu; 4) (220) Cu; 5) (311) Cu; 6) (222) Cu.

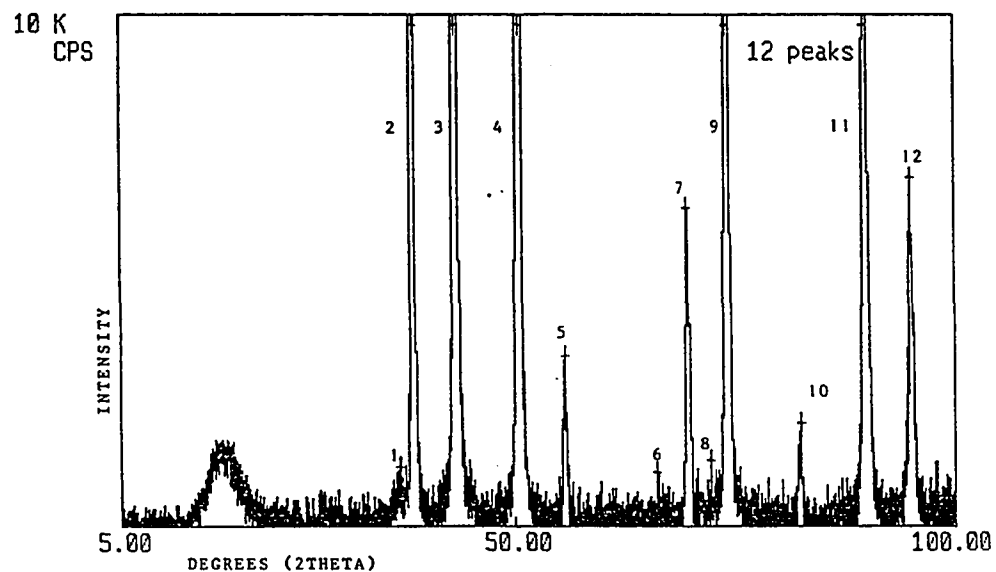


Figure 45. X-ray diffraction scan of specimen {5,2} from run 23 (unbiased, low Ta) after 10 hours at 900 Celsius. Numbered peaks correspond to: 1) (111) fcc Ta or Ta oxide; 2) (110) bcc Ta; 3) (111) Cu; 4) (200) Cu; 5) (200) bcc Ta; 6) Ta oxide; 7) (211) bcc Ta; 8) (311) fcc Ta or Ta oxide; 9) (220) Cu; 10) (220) bcc Ta; 11) (311) Cu; 12) (222) Cu.

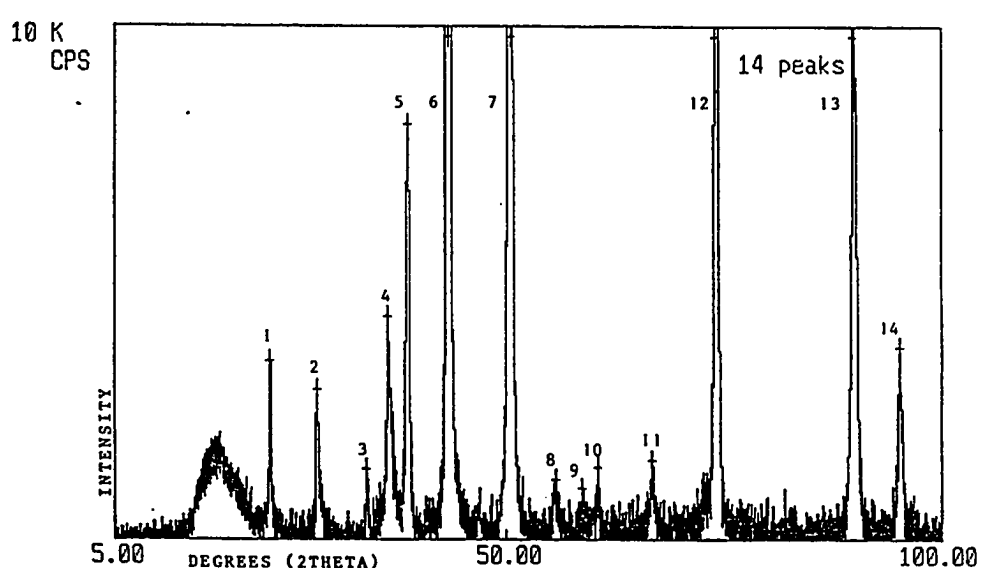


Figure 46. X-ray diffraction scan of specimen {6,2} from run 23 (unbiased, low Ta) after 10 hours at 800 Celsius. Numbered peaks correspond to: 1) Ta oxide; 2) Ta oxide; 3) Ta oxide; 4) (111) fcc Ta or Ta oxide; 5) (110) bcc Ta 6) (111) Cu; 7) (200) Cu; 8) (200) bcc Ta; 9) Ta oxide; 10) Ta oxide; 11) Ta oxide; 12) (220) Cu; 13) (311) Cu; 14) (222) Cu.

peak and fewer oxide peaks (most peaks below Ta (110) are Ta oxide) than does figure 46 (800 C, 10 hours). Because the specimen used for figure 46 was the only unbiased, low Ta specimen which showed significant levels of Ta oxide, it must have been partially oxidized during the encapsulation and heat treatment steps. A complete set of XRD scans, along with corresponding tables of diffraction peak and powder file data for Cu, Ta, and their oxides, are shown in the Appendix.

Significant features of the x-ray data include: 1) The intensities of the Ta and Ta oxide diffraction peaks increase with increasing Ta content. 2) The Ta peak widths are broadest for the as-deposited alloys and decrease with increasing annealing time and temperature. Numerical peak width data for Ta(110) as a function of annealing time and temperature are listed in table 2 and plotted in figure 47, which shows the peak width fitting parameter, *s*, versus time for 800 and 900 C anneals. Particle sizes calculated from the peak width data are listed in table 3 and plotted in figure 48, as a function of annealing time for both temperatures and bias conditions. The variation of the calculated Ta particle sizes relative to the particle sizes observed directly by TEM suggests that the Ta particles are under nonuniform strain after heat treatment. This is reasonable when one considers that the strain on an individual particle is dependent on its local environment (matrix and neighboring particles) and that the thermal expansion coefficient of Ta lies between that of Cu and Ta oxide. The linear expansion on heating from 300 to 1050 K is: for Cu, 1.45%; for Ta, 0.55%; and for Ta_2O_5 , 0.16% [81]. As expected, the XRD-calculated Ta particle sizes for the as-deposited alloys generally decrease after annealing. However, scatter in the data makes development of a quantitative coarsening relationship difficult and of questionable value. 3) The oxide contents of the coatings can be ranked based on the intensities of the oxide peaks for all heat treatments. The low Ta, unbiased coatings have little or no oxide content; the low and high Ta, biased coatings have intermediate oxide contents; and, the high Ta, unbiased coatings have the highest oxide content. 4) Some of the oxide content may be an artifact of the encapsulation process, as indicated with figure 46 (none of the other heat treated, unbiased, low Ta specimens showed

Table 2. X-RAY PEAK WIDTH DATA: PEAK FITTING PARAMETER "S (degrees)"

<u>Heat Treatment</u>	Biased Low Ta	Biased High Ta	Unbiased Low Ta	Unbiased High Ta
as-deposited	0.37-1.0	0.93	1.2	0.34-0.40
1 hour, 800 C	0.33	0.47	0.12	0.18
10 hours, 800 C	0.32	0.23-0.33	0.21	0.25
100 hours, 800 C	0.35-0.37	0.17	0.12	0.17
1 hour, 900 C	0.35	0.23	0.17	0.27
10 hours, 900 C	0.29	0.24	0.17	0.21

Table 3. CALCULATED TANTALUM PARTICLE SIZES (nm)

<u>Heat Treatment</u>	Biased Low Ta	Biased High Ta	Unbiased Low Ta	Unbiased High Ta	Average
as-deposited	34-12	13	10	37-31	23
1 hour, 800 C	38	26	106	72	61
10 hours, 800 C	39	55-38	60	50	45
100 hours, 800 C	36-34	75	108	75	65
1 hour, 900 C	36	55	77	47	54
10 hours, 900 C	44	53	77	61	58
average of HTs	38	50	86	61	57

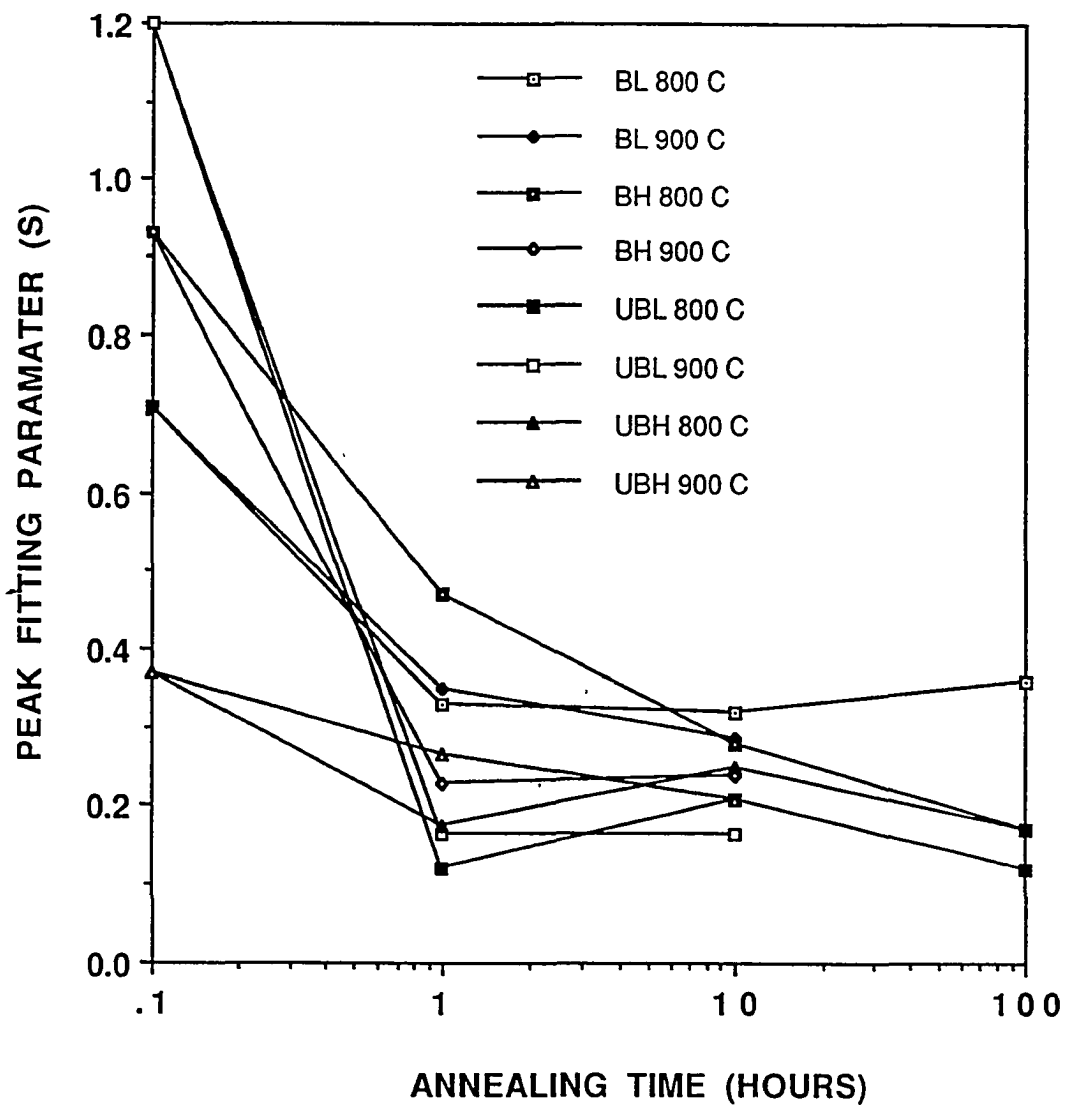


Figure 47. Plot of x-ray peak width versus heat treat time.

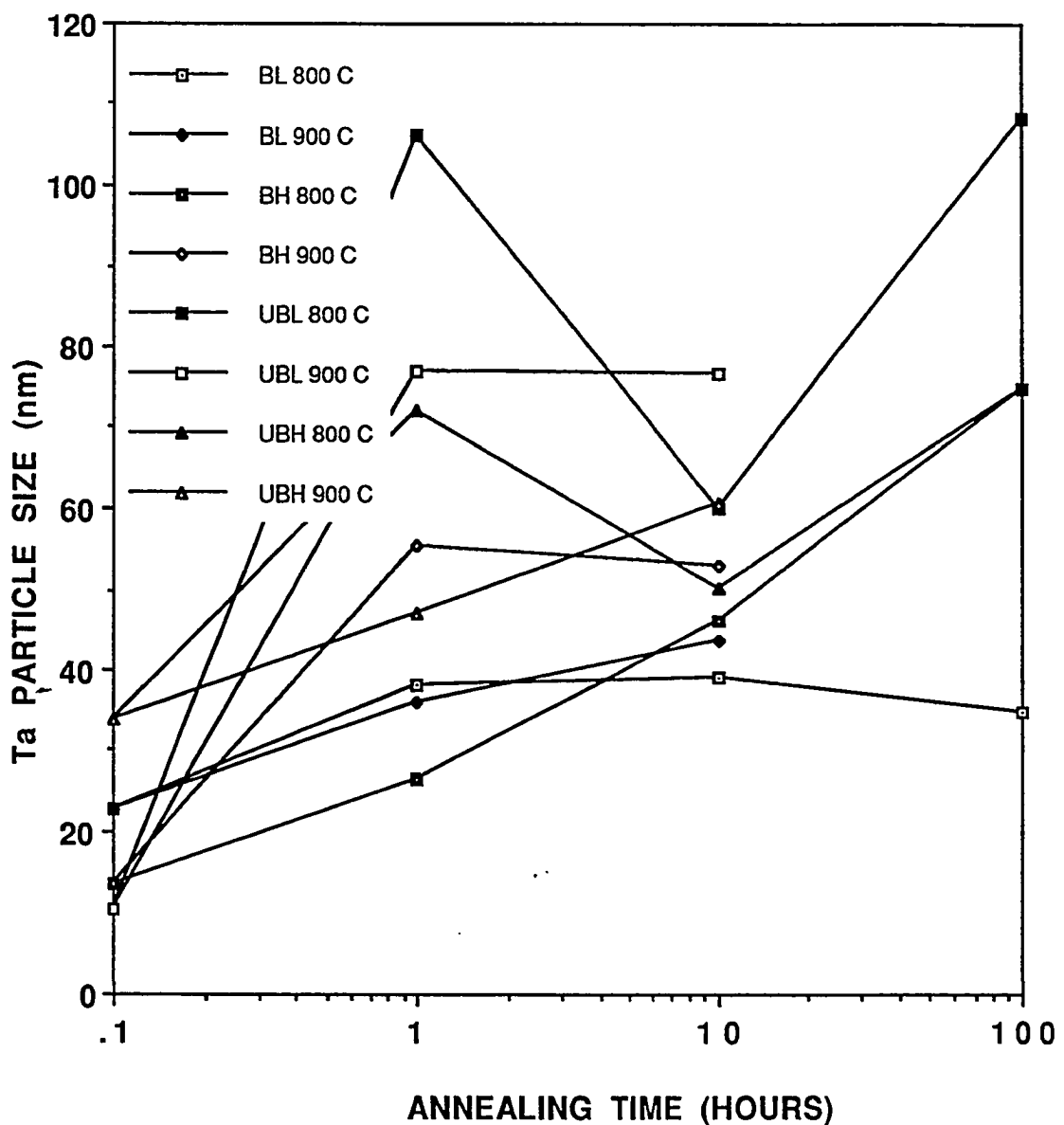


Figure 48. Plot of calculated Ta particle size versus heat treat time.

significant oxide peaks, figure 45). 5) The presence of fcc Ta could not be conclusively established by x-ray diffraction due to nearly identical interplanar spacings with the Ta oxides.

IV.E. MICROHARDNESS

Microhardness measurements on hot isostatic pressed specimens indicate that the strength of the materials after consolidation is dependent on the use of substrate bias during deposition. Many indentations were required as it was difficult to "hit" the thin, consolidated coating so that all of the indent was on the coating. Knoop microhardness values for the hot isostatic pressed specimens are tabulated in table 4. As would be expected, indents that overlapped the coating (Knoop hardness about 170 (biased) and 140 (unbiased)) and the substrate (Knoop hardness about 70) gave intermediate hardness values. From the data it is clear that the biased material is stronger than the unbiased material. The microhardness data for these Cu-Ta alloys should be interpreted as minimum values since the coating width is only slightly greater than the indent width. Under this condition, plastic deformation of the coating is influenced by deformation of the much softer Cu substrate.

Table 4. TABLE OF KNOOP MICROHARDNESS VALUES FOR HIPPED SPECIMENS

<u>Run#</u>	<u>Condition</u>	<u>Load (P)</u>	<u>Knoop</u>
1 9	biased	1 0	1 7 6
1 9	biased	2 5	1 6 4
2 0	unbiased	1 0	1 3 8
2 0	unbiased	2 5	1 4 6

Although microhardness measurements were attempted on the as-deposited coatings, the openness of the coating structure caused the measured hardnesses to be below that of the Cu substrate. Microhardness measurements were not attempted on the annealed coatings.

IV F. SHEET RESISTANCE

Sheet resistance maps made as functions of substrate location (in the same manner as for the previously discussed composition maps) and deposition bias indicate that the as-deposited coating sheet resistance is dependent on both composition and deposition bias. Sheet resistance contour maps for deposition runs 18 and 23 are shown in figures 49 (biased) and 50 (unbiased). Significant features of the sheet resistance contour maps include: 1) Sheet resistance increases with increasing Ta content (compare with composition maps in figures 3 and 4). Tantalum increases along a line running roughly from position {4,1} to position {4,7}. 2) Sheet resistance increases with the use of substrate bias during deposition. 3) Sheet resistance increases from center to edge of the substrate holder along Ta isocomposition lines, which run roughly perpendicular to the line of increasing Ta content.

IV.G. COMPUTER MODELING

Composition profiles calculated as discussed in section III.C. give good qualitative agreement with composition profiles experimentally determined over the substrate holder area. Representative composition profiles and their corresponding thickness profiles are shown in figures 51 (no bias, composition), 52 (no bias, mass), 53 (bias, composition), 54 (bias, mass). Significant results shown by these profiles include: 1) Ion bombardment during deposition causes enhanced enrichment of the coating with the material having the lower sputter yield (due to local variations in the depositing coating flux superimposed on a constant ion bombardment flux). 2) Ion bombardment causes a shift to lower deposited mass over the entire substrate holder for the same reason as above.

The computer programs developed to calculate mass and composition profiles have significant capabilities beyond the above calculations. These capabilities include: 1) Visualization of the effects of system geometry (substrate holder height, source spacing, and source positions) on the mass and composition profiles. 2) Visualization of the effects of relative evaporation rates from two sources on the mass and composition profiles. and, 3)

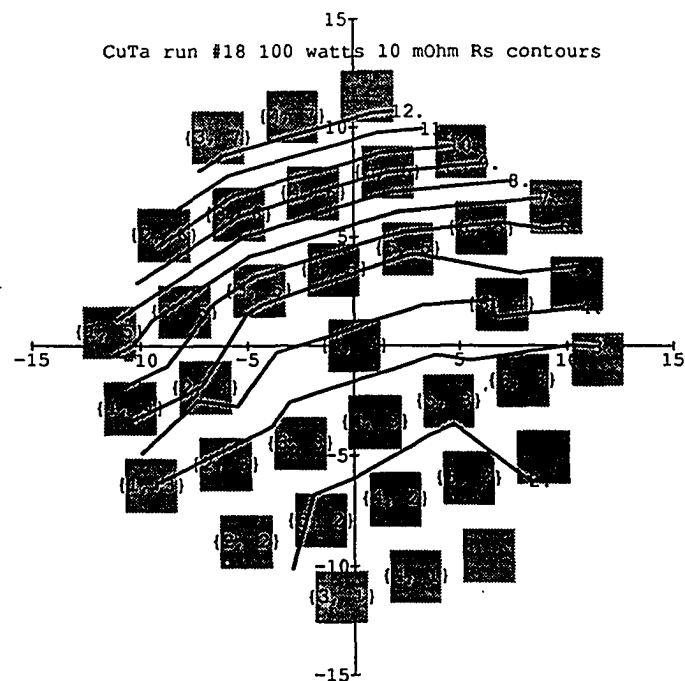


Figure 49. Sheet resistance contour map for run 18 (substrate bias)(axes in cm). The Ta source was located ~below position {4,7} and the Cu source was located ~below position {4,1}.

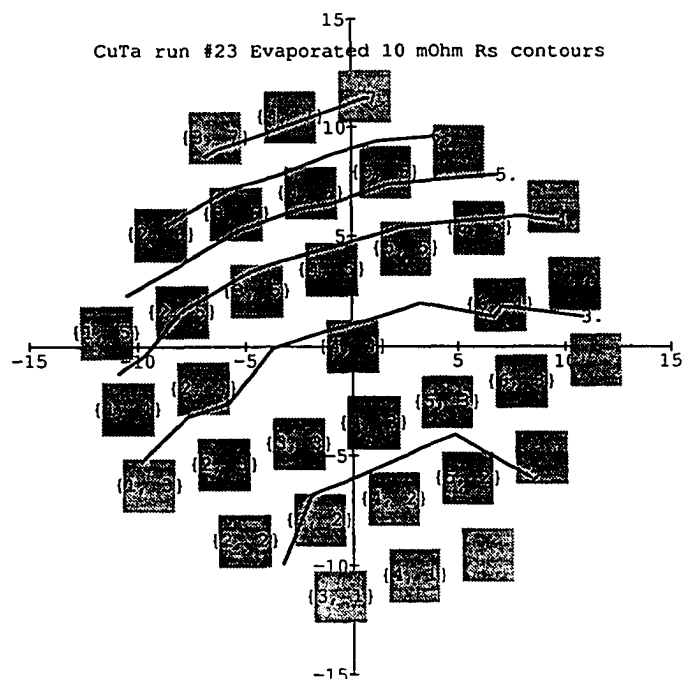


Figure 50. Sheet resistance contour map for run 23 (no substrate bias)(axes in cm). The Ta source was located ~below position {4,7} and the Cu source was located ~below position {4,1}.

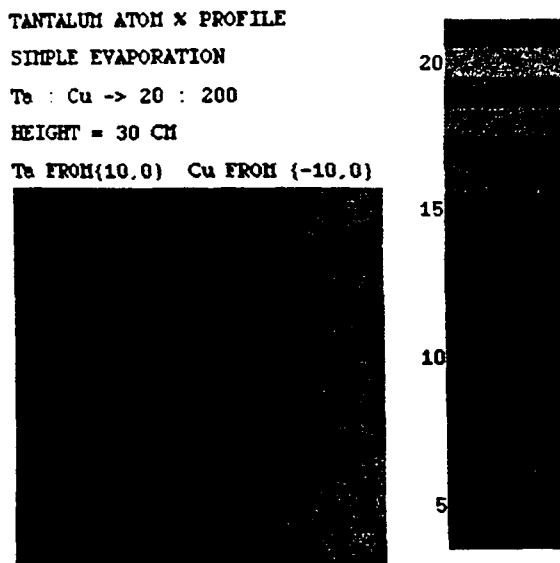


Figure 51. Calculated composition profile for deposition without substrate bias.

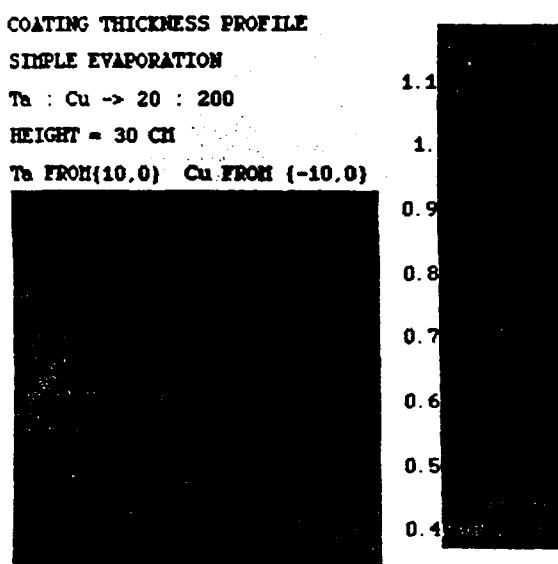


Figure 52. Calculated deposited mass (thickness) profile for deposition without substrate bias.

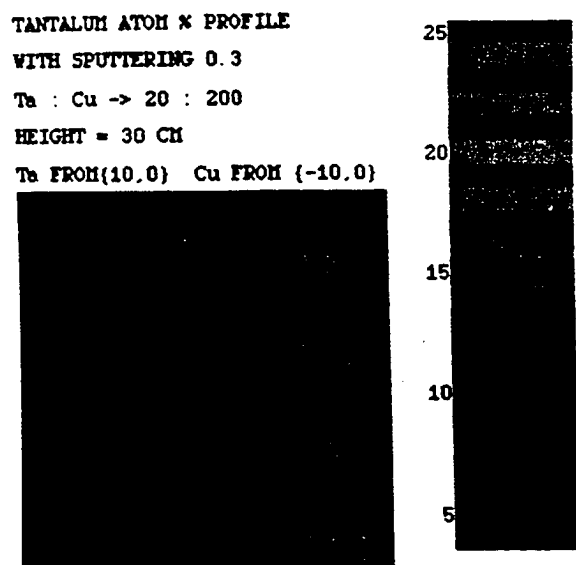


Figure 53. Calculated composition profile for deposition with substrate bias.

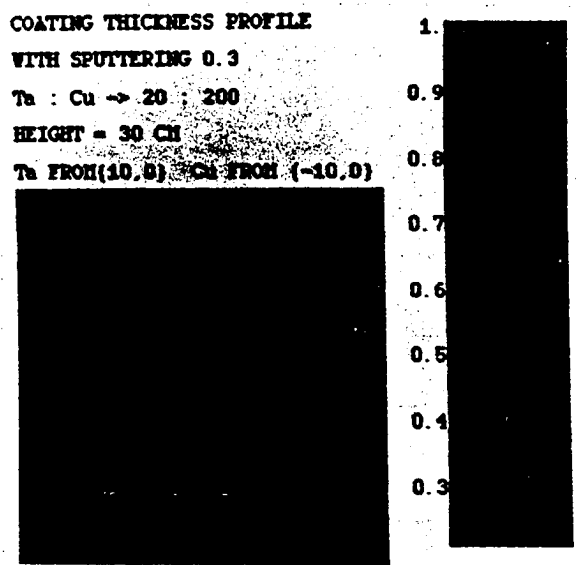


Figure 54. Calculated deposited mass (thickness) profile for deposition with substrate bias.

Visualization of the effects of ion bombardment on mass and composition profiles in systems where the two components have different sputter yields.

V. DISCUSSION OF RESULTS

The results show that nonequilibrium Cu-Ta alloys with discrete, nanoscale Ta and Ta oxide second phase particles can be produced using physical vapor deposition techniques. The compositions, sizes, and distributions of these nanoscale second phase particles may be directly related to the deposition parameters, particularly substrate bias. These second phase particles are highly resistant to coarsening and are effective at inhibiting grain growth at temperatures within 200 C of the melting point of Cu. Building upon the previously detailed results, the following sections discuss relationships between the structure and high temperature behavior of the Cu-Ta alloys and the PVD processing parameters.

V.A. ION BOMBARDMENT INDUCED MORPHOLOGY CHANGES

V.A.1. MATRIX RESPONSE TO BIASED DEPOSITION

Ion bombardment during deposition promoted morphology changes in both the matrix and the second phase. In the Cu matrix, the most visible effect of ion bombardment was to promote the formation of dense, faceted columnar structures with heavily voided intercolumnar regions (compare figures 5 and 7 and figures 6 and 8). This effect increased as the ratio of bombarding ions to depositing atoms increased and as the Ta content increased. Chapman [24] reported similar results for Cu surfaces that were sputter etched while simultaneously depositing a low sputter yield material (W). This suggests that the coating morphologies observed in this thesis arise because of the sputter yield differences between Cu and Ta.

Preliminary studies for this thesis included the Cu-Cr and Cu-Nb and the morphological relationships described above for Cu-Ta were also found for these systems. The atoms per ion sputter yields, for 600 eV argon ions, are: Cu, 2.30 ; Cr, 1.30; Nb, 0.65; Ta, 0.62). For Nb, which has a sputter yield very close to Ta, the Cu-Nb structures were very similar (at the same deposition rates, substrate power density, and refractory metal content) to the Cu-Ta structures. For Cr, which has a sputter yield much closer to that of Cu, similar structures

were produced for the Cu-Cr system only when the substrate power density (hence, ratio of bombarding ions to depositing atoms) was increased by ~10 x that required for Cu-Ta.

A secondary reason for columnar structure evolution with increasing Ta content can be inferred from figure 2, which suggests that coating structure is dependent on adatom surface diffusivity. If we consider the effective alloy melting point as that calculated using a rule of mixtures of the components, we would predict an increased tendency for lower temperature structures with increasing refractory metal content at constant substrate temperature. The difference between the Cu-Cr and Cu-Ta structures could then be interpreted partially in light of the relative melting points of Cr (1857 C) and Ta (2996 C).

Experimentally, there was not strong evidence for the evolution of an open columnar structure in the unbiased alloys over the range of compositions studied (compare figures 7 and 8). However, there was strong evidence for an increase in coating void content (porosity) with increasing Ta content, in agreement with the previously discussed rule of mixtures melting point argument. In the biased alloys, the average column width decreased with increasing Ta content (compare figures 5 and 6), also suggesting an increase in coating void content and a corresponding shift to lower temperature structures. This may also be due to a shift in the bombarding ion to depositing atom ratio with substrate position as shown in the thickness contours in the computer simulations (figures 52 and 54). The deposition conditions to give the experimentally observed composition range result in lower deposition rates in areas richest in Ta, with higher bombarding ion to depositing atom ratios, and higher deposition rates in areas richest in Cu, with lower bombarding ion to depositing atom ratios. This agrees with the preliminary Cu-Nb and Cu-Cr work for this thesis where it was observed that the column widths decreased with increasing substrate bias. Some of this argument may be negated by considering that the substantially higher power required to evaporate Ta may result in more radiative heating and higher substrate surface temperatures on Ta rich areas of the substrate holder.

Ion bombardment appears to promote a denser coating in terms of surface area of the coating per unit surface area of the substrate, especially at higher Ta contents. This was evident in the SEM where for the as-deposited coatings the faceted grains in the biased, high Ta alloy (figure 6) are clearly larger than the largest grains in the unbiased, high Ta alloy (figure 8). This effect was also evident in the consolidated specimens where large second phase particles preferentially outlined the previously open column boundaries because they were the sites of maximum plastic deformation during HIPping of the biased alloy (figure 13). Because the "prior-to-HIP" morphology of the unbiased alloy contained a more uniform distribution of porosity throughout the coating, the second phase particles after HIPping were larger and more uniformly distributed throughout the coating thickness (figure 14). This result implies that extensive plastic deformation occurred in the unbiased alloy throughout the coating thickness as internal porosity collapsed without the presence of large, dense columns. The biased alloy, which had a well developed columnar morphology, underwent less homogeneous plastic deformation during HIP consolidation and consequently a greater volume fraction of large second phase particles were found in the former intercolumnar sites. Deformation-induced particle coalescence mechanisms are discussed in section V.C.

Ion bombardment increases the matrix grain size distribution in the as-deposited coatings. Although the SEM images in figures 5 and 6 show faceted columns in the biased alloys which appear to be single grains, TEM results shown in figures 28 and 27 indicate that the columns are actually polycrystalline. The smallest grains in the biased alloy are the same size as the smallest grains in the unbiased alloy (several tens of nm). However, the largest grains in the biased alloys (~1 micron) appear to be larger than the largest grains in the unbiased alloys (~0.3 microns). This agrees with observations by other investigators, for single and multielement coatings, where the differences in sputter yields are small, that ion bombardment during deposition promotes the formation of elevated temperature, equiaxed structures at reduced substrate temperatures due to enhanced adatom mobilities [20, 28, 29]. This observation agrees qualitatively with previous work by Shin [26] for the Cu-Cr system which

indicated that the average grain size for bias sputter deposited coatings increased with increasing substrate bias and decreasing Cr (refractory metal) content.

V.A.2. SECOND PHASE RESPONSE TO BIASED DEPOSITION

The primary effect of ion assisted deposition on the second phase particles in as-deposited coatings is to promote the development (growth) of the second phase particles, as demonstrated in the TEM analyses (compare figures 15, 19, 21, and 22). This, again, is most likely due to ion bombardment enhanced adatom mobility [20, 28, 29]. This observation is in agreement with previous work by Shin [26] which indicates that the extent of metastable solid solution of Cr in Cu is decreased with increasing applied substrate bias during sputter deposition. Previous work by Savage [20] in the Al-Cu system (using DC bias) showed an ion bombardment enhanced diffusion zone extending to a depth approximately 200 nm below the surface of the growing aluminum film. The work by Savage [20] on the ion assisted deposition of aluminum on aluminum showed large concentrations of defects at depths as great as 700 nm into the substrate. Within 100 nm of the substrate surface the defect densities were so high as to prevent resolution of individual defects even at high TEM magnifications. It appears that the bombardment enhanced diffusion is largely due to migration of vacancies produced by collision cascades and not to collisional displacements (ballistic redistribution) since the range of relevant ions in the energy range of interest is only on the order of 5 nm and the extent of the observed effects is ~40x greater [20]. Further, in recent work by Anderson [15] on neutron irradiated dispersions of aluminum oxides in Cu and dispersions of chromium oxides in Cu where ballistic redistribution of material is believed to be significant, it was observed that larger oxide particles were redistributed into smaller, less distinct particles. Thus, if ballistic redistribution was the dominant mechanism in the present work, most of the motion would be done in the top 5 to 10 nm of the growing coating. Assuming ballistic mixing, the expected result would be that the second phase particles should be less developed in alloys deposited with ion bombardment than without; this was not the case. The enhanced development (growth) of the

second phase particles in the biased alloys as compared with the unbiased alloys is most likely due to ion bombardment enhanced diffusion associated with vacancies created by collision cascades in the near surface region of the growing coating.

Ion bombardment during coating deposition also influenced the second phase morphology after HIP consolidation. The observed effect was that, after consolidation, the biased alloy (figure 13) had smaller and less uniformly distributed second phase particles than the unbiased alloy (figure 14). As explained below, the origin of this difference is believed to have mechanical and chemical components.

The chemical component of the difference arises from the enhanced incorporation of residual oxygen into coatings deposited with a substrate bias. The ion bombardment-induced surface and near surface defect structures (enhanced reactivity) have been described elsewhere [20-23]. The supply of oxygen available for incorporation into the growing coating may also be increased by desorption of water molecules from the chamber walls due to the glow discharge [20]. In the present work, oxygen incorporated into some of the coatings results in a dispersion of fine Ta oxide particles, which appear more resistant to coarsening than the pure Ta particles. Outlining of the column boundaries (figures 13 and 27) with second phase particles in the biased alloy suggests that more extensive oxidation occurs in regions that had longer exposure to ion bombardment. The idea of ion assisted oxide incorporation occurs is also supported by the x-ray data (see Appendix) which shows that all biased coatings have about the same amount of oxide. This result suggests that the oxygen incorporation was proportional to some uniform flux to the surface during deposition.

The mechanical component for the second phase morphology differences arises from the porous nature of the as-deposited coatings. Coatings deposited without bias (figures 7 and 8) had a uniform void structure which causes extensive plastic deformation throughout the material during HIP consolidation (compare figures 8 and 14). Coatings deposited with bias (figures 5 and 6) had dense columnar structures with voided intercolumnar regions, suggesting that plastic deformation would occur primarily at the column tops and the intercolumnar

regions during consolidation (figure 13). The distribution of second phase particles after consolidation suggests that enhanced second phase particle growth in localized regions of relatively large plastic deformation is reasonable and in agreement with a plausible combination of coarsening by diffusional Ostwald ripening and collisional coalescence as discussed in the background section [54, 63]. In the dense column regions where little plastic deformation occurs during consolidation (figure 13), coarsening occurs by the Ostwald diffusional ripening mechanism. Conversely, in regions where extensive plastic deformation occurs during consolidation, coarsening occurs by a combination of collisional coalescence and Ostwald diffusional ripening enhanced by the plastic deformation line defect structure.

The effects of ion bombardment on the second phase particle distributions in coatings heat treated without applied stress were not as pronounced as for the HIPped specimens. The largest second phase particles observed after the heat treatments (~80 nm) were ~5x smaller than the largest second phase particles observed in the HIPped specimens (>400 nm). TEM observations gave limited information on the particle sizes in the biased alloys due to the effects of the coating topography on thinning during sample preparation. An attempt at quantitative TEM data would probably result in oversampling of the voided intercolumnar regions (thin, fine grained matrix material, figure 5) and undersampling of the columns interiors. X-ray peak width data (figure 47) indicated that the biased alloys generally had a smaller average Ta particle size after the heat treatments than did the corresponding unbiased alloys (the x-ray results for the as-deposited alloys were mixed). The increased oxygen content in the biased alloys will tie up some of the Ta as Ta oxide, making less Ta available to coarsen. Another possibility is that the oxygen may effectively modify (decrease) the interfacial tension between the matrix and precipitate so as to reduce the coarsening rate as discussed in the coarsening kinetics section of the background; the actual mechanism for this may be reduced solubility of Ta associated with stable compound (Ta oxide) formation. This latter possibility will be discussed further in a later section.

In summary, the effects ion bombardment on morphology in the Cu-Ta system appear to be: 1) The promotion of a faceted columnar structure with voided intercolumnar regions due to differences in the Cu and Ta sputter yields (figures 5 - 8). 2) A general reduction in coating void content (coating surface area per unit substrate area) which is more pronounced at higher Ta contents (compare figures 5 and 7 and figures 6 and 8) due to increased adatom mobility which results in a shift to denser elevated temperature structures. 3) An increase in the range of the grain size distribution for the Cu matrix (from a maximum of ~300 nm without bias to a maximum of ~1 micron with bias) due to the shift to larger grained elevated temperature structures under the influence of ion bombardment. 4) Generally larger second phase particles form in the as-deposited coatings due to ion bombardment enhanced diffusion (compare figures 15, 19, 21, and 22). 5) Increased resistance of the second phase to coarsening during consolidation during hot isostatic pressing due to morphology differences in the as-deposited alloy (figures 13 and 14). 6) Increased resistance to second phase particle coarsening in the absence of applied stress; possibly due to incorporated oxygen (figure 47).

V.B. DEPENDENCE OF SECOND PHASE COARSENING ON MATRIX MORPHOLOGY

The observed effects of morphology on second phase coarsening fall into the following categories: 1) the influence of Cu matrix grain size and coating void content; 2) the mechanical effects of a dense columnar versus noncolumnar voided morphology during consolidation (discussed previously in section V.A.2.); and, 3) the effects of oxygen incorporation into biased coatings and the subsequent formation of second phase oxide particles. These points are discussed in the following paragraphs.

Grain size and coating porosity influenced second phase coarsening in proportion to the ratio of coating surface area per unit area of substrate. It is believed that atmospheric exposure of the coatings prior to heat treatment resulted in the formation of a thin Cu oxide on the coating surfaces and adsorption of water vapor. When the specimens were annealed, oxygen at the surface could diffuse into the coating, react with the Ta, and produce stoichiometric Ta oxide

particles. The high surface area to volume ratios and the smaller diffusion distances of very small grains would lead to a greater volume fraction and more uniform distribution of second phase oxide particles. In the larger grains, the diffusing oxygen may combine completely with Ta in the near surface region, leaving the center of the grain relatively oxide free. Support for this idea comes from the TEM results which show that the largest second phase particles were present in the interiors of the largest matrix grains and the edges of these grains generally contained no large second phase particles and many more small second phase particles, see figure 27. Support for the idea of a contaminating surface oxide also comes from the x-ray data which indicate that second phase oxide content increases with increasing coating void content. From the bottom row of table 3 for heat treated, unbiased alloys, the average dense, low Ta alloy has a Ta particle size 40% larger than the average voided, high Ta alloy. However, it should be noted that no Cu oxide peaks were present in the XRD scans of the as-deposited alloys; thus indicating that the surface oxide is very thin and/or the surface source of oxygen is water vapor.

~ Matrix grain size in a voided structure may also limit coarsening when the second phase particles grow to a size such that particle spacing in a fully dense material would approach the dimensions of the dense matrix grain in the voided structure. This effect was not observed in the current work, probably due to oxygen contamination and insufficient coarsening time.

In biased alloys, the XRD data suggests that oxygen incorporation was enhanced by the plasma during the deposition process, the result being formation of a fine dispersion of second phase (Ta oxide) particles. TEM analyses (figure 26) of larger second phase particles with a background of much smaller second phase particles support the XRD results . XRD peak width data (table 3) supports the belief that oxygen incorporation leads to a decrease in Ta particle size through reduction of the amount of uncombined Ta and the stability of the Ta oxide particles.

The Ta-O phase diagram indicates that the oxygen solubility in Ta is ~2 atomic percent at 900 C, suggesting that O present in the alloy readily forms Ta oxide [6]. This research did not attempt to determine Ta oxide nucleation sites or preferred lattice sites for O in solid solution in

the second phase particles. However, if O locates in or near the Cu-Ta interface it should have an effect on the particle/matrix interfacial energy. From the LSW coarsening theory (Section II.G.1.), a decrease in interfacial energy results in a decrease in the particle coarsening rate. This effect applies generically to other coarsening theories since the fundamental driving force for coarsening is reduction of the chemical potential associated with the particle/matrix interfacial curvature. Experimental evidence in this study indicates that O reduces the coarsening rate and therefore O appears to reduce the matrix/particle interfacial energy. This evidence includes: 1) The particle sizes in the near surface regions of the matrix grains were smaller than in the grain interiors, figure 27. Oxygen from the surface is consumed during annealing by Ta near the grain surface and is unavailable to the grain interior. 2) The average second phase particle size in the material with more uniformly incorporated oxygen (substrate bias) is smaller than that in the material with less uniformly incorporated oxygen (table 3). 3) The existence of faceted and nonfaceted second phase particles over the entire range of sizes completely overlap, which suggests a variation in interfacial chemistry and/or a variation in second phase particle composition. Work by Batawi and Morris [82] and Morris, Batawi and Morris [83] on rapidly solidified Cu-B alloys indicated that the presence of a boron compound former (yttrium) and the formation of an insoluble compound (YB_6) resulted in improved coarsening resistance. This occurred due to the low diffusivity Y and its low solubility induced by the stability of the YB_6 phase. This correlates well with the present research where Ta is the low diffusivity/solubility element and Ta oxide has good stability.

The above paragraph suggests that development of a bimodal second phase particle size distribution can be the result of a nonuniform distribution of O from matrix grain exterior to interior. For alloys in the present study, other possible causes for multimodal second phase particle size distributions include: 1) macro particles (> average coating thickness) ejected from the evaporation sources; 2) nonuniform plastic deformation during HIP consolidation (figure 13); and, 3) variations in particle sizes between various lattice sites, e.g., particles on a grain boundary or in a grain interior (figure 42).

In summary, the effects of morphology on second phase coarsening appear to be: 1) A decrease in Cu matrix grain size and an increase in coating void content results in a decreased coarsening rate during annealing in the absence of applied stress. This is probably due to availability of oxygen in the near surface region during heat treatment, which may reduce the matrix/second phase interfacial energy. 2) An increase in initial coating void content prior to HIP consolidation results in increased coarsening and, due to coalescence of second phase particles during plastic flow of the matrix, uniformity of the second phase particle distribution (size and spatial) is dependent on the uniformity of the void content in the coating prior to consolidation. 3) Dispersed O, associated with biased alloys, inhibits second phase particle coarsening, probably through the effect of O on the matrix/second phase interfacial energy.

V.C. COARSENING MECHANISMS

The mechanism for second phase particle coarsening in this study is a combination of Ostwald ripening and collisional coalescence. In the static (encapsulated) heat treatments, particle coarsening occurs by a purely diffusional mechanism, Ostwald ripening. During HIP consolidation, relative motion of the second phase particles occurs during elevated temperature plastic deformation, thus allowing coarsening to occur both by coalescence of "colliding" particles and by Ostwald ripening.

The static encapsulated and HIP coarsening treatments each displayed significantly nonuniform coarsening rates, depending on the matrix morphology. In the static heat treatments, the coarsening rate of an individual second phase particle was influenced by its proximity to a grain or column surface, which is believed to act as a source of O contamination (figure 27). In the HIPped specimens the coarsening rate of an individual second phase particle was influenced by its proximity to regions of extensive plastic deformation during consolidation (figure 13). For HIPped specimens, where both the fundamental coarsening mechanisms were active, a nonuniformity in the preconsolidated microstructure results in spatial nonuniformity of the dominant mechanism. In bias deposited and HIPped material, coarsening in the dense

column regions that underwent little or no plastic deformation was dominantly Ostwald ripening and coarsening at the column tips, column boundaries, and powdery regions that underwent extensive plastic deformation was dominantly by collisional coalescence and dislocation assisted diffusional coarsening.

Coarsening in the dense, columnar regions of the bias deposited and HIPped material was more extensive than in a similar specimen vacuum encapsulated (no applied stress) and heat treated identically. This is possibly due to accelerated diffusion due to dislocations introduced and moved by the plastic strain occurring during HIP consolidation [74]. Experimentally, few dislocations were visible in the interiors of the grains after consolidation (figure 42), they were likely annealed "out" between the initially extensive consolidation early in the HIP cycle and the end of the thermal cycle. This assumes that at 900 C the bulk of the deformation occurs in the first few minutes and very little deformation occurs during the remainder of the hour. Another possibility is that the hydrostatic pressure influences the coarsening by influencing the interfacial energy between the matrix and the particle and/or influencing the diffusivity of the second phase constituents through the matrix. Three components of the hydrostatic effect are discussed in the following paragraphs.

The first component is the effect of pressure on the matrix/particle interfacial energy. The second phase can be approximated as an isotropic liquid sphere (droplet) in a matrix, where pressure in the droplet arises from the surface tension (interfacial energy) as shown by

$$P = 2 T/r \quad (18)$$

where P is the pressure, T is the surface tension, and r is the droplet radius [2]. From this approximation, an increase in pressure requires a corresponding increase in surface tension (interfacial energy) at constant radius. Recalling that the LSW coarsening theory [52, 53] indicates that an increase in interfacial energy corresponds to an increase in coarsening rate, an increase in pressure corresponds to an increase in coarsening rate.

The second component is the effect of pressure on the diffusivity. Since substitutional diffusion is largely a vacancy controlled process, we can consider the effect of pressure on the

number of vacancies and infer an effect on diffusivity. Physically, removal of vacancies decreases the volume of the material and this suggests that a material will lose vacancies in an effort to relieve an applied pressure. Shewmon [84] has shown thermodynamically that an increase in pressure results in a decrease in self-diffusion in pure metals. Experimentally, Hudson and Hoffman [85] observed a 10-fold decrease in Pb self-diffusivity for a 980 MPa pressure increase in pressure of about 980 MPa. Recalling that the LSW coarsening theory shows that the coarsening rate decreases with a decrease in diffusivity of the second phase components [52, 53], an increase in pressure would be expected to decrease the coarsening rate through a decrease in diffusivity of the second phase components.

The third component is the effect of pressure on the substitutional solubility of Ta in the Cu matrix. This effect would arise due to the increase in atom size (~3 % [77]) as a Ta atom goes from a bcc coordination in a second phase particle to fcc coordination in solid solution in the Cu matrix. From the argument in the above paragraph, we can infer that the system will resist changes that increase volume when it is subjected to a hydrostatic pressure so the solubility of Ta in the Cu matrix will be reduced. Further, since the volume per Ta atom increases from 143.5 Å³ to 144.4 Å³ if the bcc second phase is converted completely to fcc second phase, this argument says that the HIP hydrostatic pressure would encourage sufficiently large, metastable fcc Ta particles to transform to the stable bcc form. This argument also implies that it is easier to get Ta into solid solution in the Cu from the fcc Ta particles, where there would be no coordination-induced volume change, than from the bcc Ta particles. Recalling that coarsening rate decreases with a decrease in the concentration of the particle atoms in the matrix, an increase in pressure would result in a decrease in the coarsening rate based on a decrease in Ta solubility with increasing pressure.

The above three components of the HIP hydrostatic pressure argument predict conflicting effects of pressure on coarsening. Although the magnitude of response for each component to pressure is not known, this research has found enhanced particle growth in low strain regions of the HIPped material. If the original argument that hydrostatic pressure can

increase coarsening is correct, then the dominant effect of pressure must be to increase the matrix/particle interfacial energy. In reality, the enhanced particle growth (HIP versus encapsulated and annealed) probably results from of a combination of dislocations introduced by the plastic strain and the effects of pressure on the diffusion of Ta through the Cu lattice.

Summarizing this section, the coarsening mechanisms for the second phase particles in this work appear to be: 1) Diffusional Ostwald ripening in specimens heat treated without applied stress. 2) Diffusional Ostwald ripening in the low strained (dense columns) of the HIPped material with accelerated coarsening due to the effects of dislocations and/or hydrostatic pressure. and 3) A combination of diffusional Ostwald ripening and collisional coarsening in the previously heavily voided regions of material in the HIPped specimens.

V.D. VARIATION OF COMPOSITION WITH SUBSTRATE POSITION

The effects of substrate position on coating composition are visible in figures 3 and 4. These agree reasonably well with profiles calculated using the cosine law (figures 53 and 51). Reasons for the small differences between calculated and experimental composition profiles would include the following: 1) Experimental errors probably occurred in the coating composition measurements. 2) No adjustment in the compositions was made to account for the presence of oxygen in the coatings. 3) Linear extrapolation was used to get the experimental contours from the data points. 4) Shadowing effects of the source crucible walls, which vary with the source charge height and the dimension of the source area, were not accounted for. The shadowing effect is illustrated in figure 55. 5) No allowance was made for coating atom scattering between evaporation and deposition.

Figures 3 and 4 provide more understanding of the deposition process than is immediately apparent. The distribution in deposition rates from the evaporation sources that gives rise to a variation in composition also gives rise to a variation in thicknesses, with a mirror line that lies approximately along the line from {4,1} to {4,7}. This feature of the PVD process can be seen in the calculated mass profiles in figures 52 and 54. An important

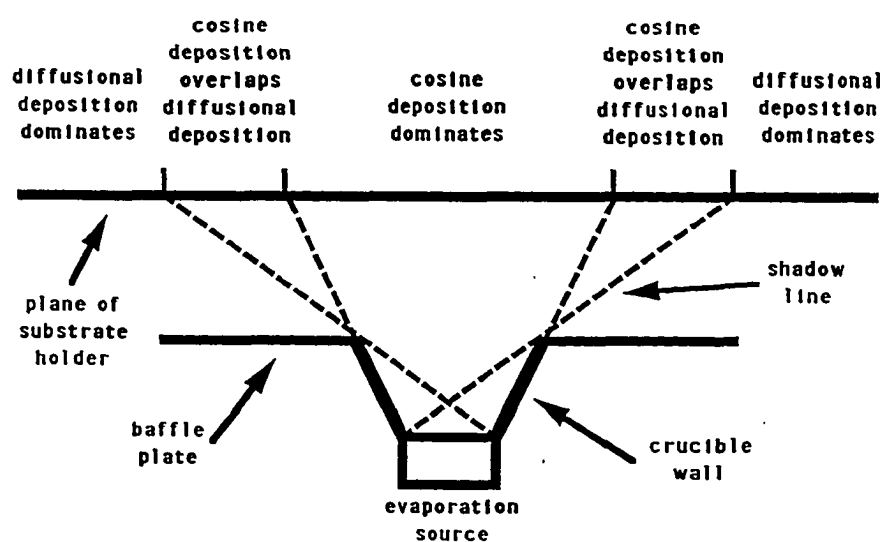


Figure 55. Schematic illustration of evaporation source geometry giving rise to nonuniformities in deposition due to shadowing effects.

conclusion of this data is that the deposition rates and, in the case of deposition with substrate bias, the ratio of bombarding ions (and other energetic species) to depositing atoms are not uniform across the substrate holder. In a similar manner, incorporation of residual gasses in the coating varies from location to location across the substrate holder. Experimentally, the XRD data indicated that the coating oxide content had a positional dependence such that: 1) The heavily voided, unbiased, high Ta coating had the highest oxide content. 2) The dense, unbiased, low Ta coating had the lowest oxide content. 3) The mixed structure coatings (high and low Ta) deposited with substrate bias have intermediate and approximately equal oxide contents. Some considerations for the incorporation of residual gases are presented in the following paragraph.

It is easily recognized that the fraction of residual gas incorporated during deposition is proportional to the relative fluxes of the residual gas and the depositing coating atoms. Less obvious, but equally important, is the fact that residual gas incorporation is also dependent on coating structure and on deposition parameters such as substrate temperature, substrate bias, and system geometry [20]. Ideally, coating growth is planar and the flux of residual gas is constant across the substrate holder so that its concentration in the coating varies with position only as the relative flux of depositing coating atoms varies with position. Glang [35] gives equations for calculating relative fluxes of coating atoms and residual gas atoms at the substrate surface. Using these relationships and assuming the deposition rate to be ~5 microns per hour (1.18×10^{16} atoms/cm²/sec) and the residual gas (~20% O) pressure is less than 10^{-6} torr (1.3×10^{-4} Pa), the impinging O flux is $<7.17 \times 10^{13}$ molecules/cm²/sec and the O content of the coating should be <1 atomic percent if we ignore the presence of the Ar working gas. Al coatings deposited by the author under similar conditions and in the same deposition system had <1 atomic percent incorporated argon [20]. Nonuniform incorporation of residual gasses (aside from the relative flux dependence) is promoted by nonuniformity in structure as illustrated by the differing oxide contents for coatings deposited without substrate bias (the dense, low Ta structure had an oxide content lower than that of the heavily voided, high Ta structure)

As discussed in section V.B., a variation in O content with position may be observed due to formation of a thin surface oxide after coating deposition. Assuming that the oxide forms as a continuous, uniformly thick layer over the entire exposed surface, this variation in O content will be strongly coupled to the Ta content since a high Ta content has been found to produce a high void content in the coating. Experimentally, the oxide may not be of uniform thickness at every coating exposed surface due to: 1) The conditions most favorable for oxide growth are when the metal surface (Cu and/or Ta) is at elevated temperature. 2) The coating is at an elevated temperature when coating deposition ceases and during the cooldown period after deposition. 3) The coating is under vacuum during cooldown so the flux of O to the exposed surface is limited by the partial pressure of O. 4) The interior surfaces are not line of site to the outer surface and the open vacuum (source of O), so oxide growth on the interior surfaces is likely limited by the shortage of oxygen. Experimental support for this reasoning is found in the heat treated, unbiased, high Ta alloy where it was observed that after heat treatment the more ductile portion of the coating is that adjacent to the substrate (figure 12). If the presence of oxygen inhibits bonding of individual particles of the powdery structure during heat treatment, then it seems apparent that there is more oxygen in the near surface region of the coating and since the deposition process would have caused otherwise uniform incorporation of oxygen, the oxide must have been formed during the cooldown in a manner similar to that described above.

Summarizing this section, the effects of substrate position on coating composition appear to be: 1) A reasonably smooth variation in the Ta content with position on the substrate holder, which can be approximated by calculations using the cosine law. 2) A qualitatively evaluated oxygen content which appears to vary with position on the substrate holder with components depending on both the local relative fluxes of impinging residual gas atoms and depositing coating atoms and the positional variation in coating structure associated with the positional variations in coating Ta content.

V.E. MICROSTRUCTURAL VARIATION WITH COMPOSITION

The effects of composition on morphology have been included in the previous Discussion sections and can be summarized as follows: 1) An increase in Ta content results in an increase in coating void content for coatings deposited without substrate bias; due to the increased "rule of mixtures" melting point of the alloy. 2) An increase in Ta content results in a decrease in the width of the dense, columnar structures observed in bias deposited coatings; this effect is coupled to the relative sputter yields of Cu and Ta. 3) The sum effect of (1) and (2) is that an increase in Ta content increases the "rule of mixtures" melting point of the depositing material and results in a lower homologous deposition temperature. This is in agreement with a transition to a voided, low temperature structure as shown in the structure zone models of Movchan and Demchishin [86] and Thornton [25]. 4) Oxygen in the material reduces the second phase particle coarsening rate and nonuniform O distribution of between the interior and exterior regions of larger grains appears to result in nonuniform second phase particle sizes in those regions after heat treatment.

V.F. MICROSTRUCTURAL RESPONSE TO HEAT TREATMENT

The effects of heat treatments on second phase morphology were discussed previously in this Discussion section. The effects of heat treatments on matrix morphology appear to be relatively minor. The only really visible effect that the heat treatments had on matrix morphology was to increase the apparent ductility of the coatings deposited without substrate bias, implying that some degree of sintering occurred between the granular structures of the coatings, as shown in figures 7, 8, 11, and 12. The effects of heat treatments on matrix morphology were not readily distinguishable in the TEM due to a large variability in matrix grain sizes in the as-deposited and heat treated alloys.

Sintering of the matrix particles is driven by the chemical potential associated with the radius of curvature of the interface between the particles; this is very similar to the driving

force for grain growth of large grains at the expense of smaller grains. Verhoeven [48] gives the chemical potential gradient as:

$$\Delta\mu = V g (1/r_1 + 1/r_2) \quad (19)$$

where $\Delta\mu$ is the chemical potential gradient, V is the atomic volume, g is the interfacial tension, and r_1 and r_2 are the principal radii of curvature of the boundary between the particles.

Using an interfacial tension of 1150 ergs/cm² for Cu [2], the chemical potentials for Cu grain sizes representative of that found in the present study were calculated to be 33.9 μ eV/atom for 10 micron grains, 1.7 meV per atom for 200 nm grains, and 6.8 meV per atom for 50 nm grains. 40 microns (8.5 μ eV/atom) is a typical size for "powder metallurgy" Cu powder. Cu powder 43-73 microns in size is substantially sintered in 10 hours at 815 Celsius [87]. Although the calculated driving force (chemical potential) for sintering in the small Cu grains observed in the present work is orders of magnitude more than that required for sintering in the conventional powder material, sintering did not occur. Explanation for the observed lack of sintering lies in the Ta and O contents of the alloys.

Impurities in solid solution are well known to segregate to internal interfaces, including grain boundaries, and to slow boundary motion by a process called solute drag. Work by Aust and Rutter [88] in the Pb-Sn system indicated that increasing the Sn content from less than 1 ppm to 60 ppm decreased grain boundary mobility by a factor of 10^5 . When the grain boundary solute (Ta) concentration becomes sufficient to form well defined precipitates, the grain boundaries would be pinned by second phase particles according to the Zener model [13]. Using the Zener relation (Equation (4)) and assuming a uniform Ta particle size, the stabilized matrix grain size may be calculated. For the low (~6 at.%) Ta alloys, 10 nm particles give 150 nm matrix grains, 20 nm particles give 300 nm matrix grains, and 40 nm particles give 600 nm matrix grains. For the high (~18 at.%) Ta alloys, 10 nm particles give 53 nm matrix grains, 20 nm particles give 106 nm matrix grains, and 40 nm particles give 212 nm matrix grains. From the measured Cu matrix grain sizes in the heat treated, high Ta alloys, regions were found with grain sizes which agreed with the predictions of the Zener model. Experimental

observations of significantly coarsened particles on the Cu grain boundaries of the HIPped materials (figure 42) indicate that the second phase particles are able to pin the grain boundaries and thus inhibit grain growth related morphology changes during heat treatment.

In summary, the microstructural responses to heat treatment appear to be: 1) an increase in second phase particle size through coarsening at a rate which appears to decrease with an increase in the local O concentration; 2) transition from an fcc and bcc second phase particle mixture in the as-deposited alloys toward a bcc structure for the larger, coarsened second phase Ta particles in the heat treated alloys (note that fcc Ta was also present in the heat treated alloys); and, 3) inhibited by the effectiveness of the small, second phase Ta particles at reducing grain boundary mobility and thus grain growth related morphological changes.

V.G. MICROSTRUCTURAL RESPONSE TO CONSOLIDATION BY HIP

The effects of HIP on coating morphology differs in several aspects to annealing without applied stress: 1) HIPping results in an apparent reduction in the oxide content of the unbiased alloy. 2) HIPping more effectively reduces the coating void content. 3) HIPping increases the matrix grain size. The details of these effects are presented in the following paragraphs.

V.G.1. REDUCTION IN OXIDE CONTENT

The reduction in oxide content apparent for the HIPped, unbiased alloy in comparison to the annealed alloy may arise for the following reasons:

1) The as-deposited alloys came from different deposition runs. Different deposition runs may give differing coating residual gas contents due to normal run to run variations in the deposition conditions. As an example, the substrate position on the substrate holder is a factor since the radiant heating for a substrate above the Ta evaporation source will be greater than that for a substrate above the Cu source. This temperature difference should, according to the structure zone models [25], result in coatings with different densities and morphologies. Also, since the deposition rate is higher over the Cu source, the lower residual gas to depositing

coating flux ratio in this area would result in reduced residual gas incorporation. A denser structure presents less available surface area for adsorption of residual gasses and water vapor. Runs also may have varied in the temperature of the substrate holder when the deposition chamber was vented to allow substrate changes.

2) The alloys had slightly different compositions. The alloy that was HIPped has ~3 at. % less Ta than did the annealed, high Ta alloy. The slight shift toward a more dense coating morphology would result in a reduction of surface area for pickup of residual gasses and a correspondingly lower final oxide content. This was verified by the XRD which showed that the annealed, unbiased, high Ta alloys had higher oxide contents than did the annealed, unbiased, low Ta alloys (produced on the same deposition runs).

3) The encapsulation processes for HIP and for vacuum annealing were different and these differences may give rise to different oxide contents. Encapsulation in quartz may have allowed partial specimen oxidation when the tube was heated in air for necking and may have allowed incorporation of water vapor due to efforts to minimize specimen heating. Contrasting, encapsulation for HIP used a Cu tube that was loaded and evacuated before heating to close the tube. The tube was heated and closed under vacuum and the high conductivity of the Cu tube may have allowed sufficient specimen heating under vacuum to allow desorption of water vapor from the coating surfaces and an overall reduction in the amount of oxygen present for oxide formation during the consolidation. The reduction of oxide content was determined by the increased Ta particle size in the unbiased alloys versus the same composition biased alloys.

The apparent reduction of oxide content in the HIPped unbiased alloy is probably due to some combination of the factors discussed above. This effect on HIPped morphology versus vacuum heat treated morphology is more a function of the specimen preparation than of the actual consolidation of the HIP.

V.G.2. REDUCTION IN VOID CONTENT

The reduction of void content in the HIPped morphology, as compared to the vacuum heat treated alloys, was a direct consequence of the applied stress. During HIPping the hydrostatic pressure applied on the tube-encapsulated material causes the voids within the material to be collapsed. It should be noted that the sample/support block/tube geometry used in this study constrained the initial plastic deformation to mainly a planar compression-mode. Void content of the HIPped specimens was near zero (no voids were observed using either SEM or TEM). Any residual gasses from the encapsulation were apparently absorbed during the consolidation.

V.G.3. INCREASE IN MATRIX GRAIN SIZE

Hot isostatic pressing resulted in an increase in the matrix grain size. This was probably the result of a combination of factors:

1) Consolidation resulted in an increase in the dimension of the continuous matrix phase. This is a simple consequence of the effect of the surfaces of the material; a grain in the material can grow no larger than the dimensions of the free surfaces that contain it. For example the largest diameter of a grain in a wire is normally no larger than the diameter of the wire. When the alloy films for this study were consolidated, the free surfaces associated with the column boundaries and the powdery grains were eliminated and the matrix grains could grow beyond their previously limited dimensions.

2) Plastic deformation resulted in enhanced coarsening of the second phase particles and the accompanying grain growth is a direct consequence of the Zener grain size model [13]. When the particles coarsen, then at a constant particle volume fraction the matrix grain size stabilized by these particles would increase.

V.H. COMPOSITIONAL SHIFT DUE TO ION BOMBARDMENT

Ion bombardment effects alloy composition for the following reasons:

1) Ion bombardment during deposition results in enrichment of the coating with the lower sputter yield component, with the extent of this enrichment dependent on the local ratio of bombarding ions to depositing atoms. This was illustrated graphically with the computer simulations shown in figures 51 and 53. The extent of the sputter enrichment effect measured experimentally was complicated by geometrical shadowing effects and by instabilities in the evaporation sources.

2) Ion bombardment during coating deposition increased incorporation of residual O. As previously discussed, the increased O level is related to enhanced release of adsorbed water vapor from the chamber walls and enhanced incorporation of O into the growing coating due ion bombardment.

3) Ion bombardment affected composition through its influence on coating morphology. This appears to be related to the coating surface area per unit substrate area of the coatings. SEM observations indicate that the rank of the coating surface areas per unit substrate area from least to greatest are as follows: unbiased, low Ta; biased, low Ta; biased, high Ta; and unbiased, high Ta. A low to high ranking of the XRD-derived oxide contents gives the identical order, suggesting a strong correlation between coating surface area and annealed alloy oxide content. TEM observations of variations of second phase coarsening rates in the near surface and core regions of large matrix particles also suggest a surface related chemistry difference. Apparently, ion bombardment can influence composition by influencing the specific surface area of the material available for adsorption of atmospheric gasses prior to heat treatments.

V.I. COMPOSITIONAL INFLUENCE ON COARSENING

The effects of composition on second phase coarsening can be inferred from XRD peak width data, figure 47, and Ta grain size data, table 3. For biased alloys, the average second phase particle size is larger in the annealed, higher Ta alloy. For unbiased alloys, the average second phase particle size is larger in the annealed, lower Ta alloy. The second phase particle size is generally larger in the annealed, unbiased alloys. These effects, which appear to be

related to the residual gas content and surface area of the coatings, may be explained as follows:

1) The incorporated gas contents and surface areas of all biased alloys should be about equal, so the observed direct correlation between Ta particle size and Ta content is consistent with the premise that the reduced particle spacing leads to increased overlap of Ta diffusion fields. 2) In unbiased alloys, the incorporated gas contents should be about equal but the surface area of the high Ta alloy is much greater than that of the low Ta alloy. Under these conditions the Ta particle size should be correlated to both the Ta content of the coating and the potential for oxidation of the Ta particles by adsorbed O during annealing. Apparently the influence of the surfaces on particle coarsening is dominant since the second phase particle size is generally smaller in the high Ta alloy. 3) The bias deposited alloy has a higher content of uniformly incorporated O and so should (and does) have a consistently smaller second phase particle size after annealing. Briefly, the strongest compositional influence on second phase particle coarsening appears to be residual O incorporated during coating growth or absorbed from the coating surface during annealing.

V.J. INFLUENCE OF BIAS ON TANTALUM SOLUBILITY

Since second phase particles (Ta rich) were found in the low Ta alloys before annealing (independent of bias), the metastable solid solubility of Ta is less than the 6 atomic percent in these alloys. The TEM-imaged second phase particles were larger in the as-deposited, biased alloys, it is reasonable to assume that substrate bias reduces the metastable solid solubility of Ta in Cu. This result, which is in agreement with the work of Shin [26] for bias-sputter deposited Cu-Cr where it was observed that the metastable solid solubility of Cr in Cu decreases with increasing substrate bias during deposition, may be explained by the enhanced adatom mobility created by the ion bombardment.

V.K. MECHANICAL PROPERTIES

The mechanical properties for these alloys were evaluated using Knoop microhardness measurements. Porosity in the as-deposited and heat treated coatings resulted in hardness measurements below those for the Cu substrate, ~70. Measurements on the HIPped material indicated that the biased alloy, Knoop hardness of ~170, was somewhat harder (stronger) than the unbiased alloy, Knoop hardness of ~140. This was expected from the Hall-Petch relationship since the matrix grain size of the HIPped, biased alloy was smaller than that of the HIPped, unbiased alloy. Because the Knoop indent width was approximately one half the HIPped coating thickness, the coating hardness measurements are believed to be strongly influenced (reduced) by the properties of the surrounding, weak substrate material. The hardness results therefore should be interpreted as "underestimates" of the true values for these materials.

V.L. STABILITY OF FCC TANTALUM

The presence of fcc Ta particles in both the as-deposited and heat treated alloys was conclusively demonstrated using electron diffraction (figures 20, 29 and 30). The lattice of the fcc Ta was oriented identically to that of the Cu matrix. The presence of fcc Ta was anticipated in the as-deposited films because of the work of Denbigh and Marcus [10] and Chopra and co-workers [11], who observed fcc Ta films up to a "critical" thickness of ~50 nm on a variety of substrates at substrate temperatures up to 400 C. At greater thicknesses and temperatures, the films reverted to the normal bcc structure. The observed stability of the fcc Ta particles when annealed at temperatures as high as 900 C is not necessarily in disagreement with references [10] and [11] due to the small particle sizes and the three-dimensional restraint of the surrounding Cu matrix. In the manner previously observed for stabilized fcc Fe particles in a bcc Fe matrix, the average Ta particle diameters are sufficiently small so as to be stabilized by the surrounding Cu matrix [89]. In addition, the lattice parameters (Cu < Ta) and thermal expansion coefficients (Cu > Ta) of Cu and Ta are such that on heating the misfit strain at the particle/matrix interface is decreased, providing a further stabilizing influence.

VI. CONCLUSIONS

This research has successfully demonstrated that physical vapor deposition processes can "design" at the near-atomic scale the microstructures of metastable Cu_{1-x}Ta_x alloys. These alloys consist of an essentially pure Cu matrix with a dispersion of discrete, nanoscale second phase particles. The Ta and Ta oxide second phase particles were in the 2 to 10 nm size range and were found to be highly resistant to coarsening during annealing at temperatures as high as 900 C. Specific conclusions of this research, such as relationships between PVD processing parameters and the film morphology, are listed below.

As-Deposited Alloys

- 1) The morphology of the Cu matrix was dependent on Ta content and ion bombardment, both of which affect adatom mobility. Film densities generally increased with decreasing Ta content and increasing ion bombardment.
- 2) Ta content varied with substrate holder position, in agreement with computer generated composition profiles based on the cosine law and on the sputter rates of Cu and Ta.
- 3) Second phase particle size was dependent on Ta content and ion bombardment. The "second phase" consisted of discrete fcc Ta, bcc Ta, and Ta oxide particles, the majority of which are smaller than 10 nm. Increasing Ta content and ion bombardment promotes the formation of a larger volume fraction of 10 - 20 nm particles.

Annealed Alloys

- 4) The matrix morphology was changed little by annealing, even at 900 C for 10 hours. TEM results indicated that the second phase particles are effective at inhibiting Cu grain boundary motion, consistent with the predictions of the Zener model.
- 5) The second phase particles after annealing also consisted of bcc Ta, fcc Ta, and Ta oxide. The stability of fcc Ta is attributed to the influence of the surrounding fcc Cu matrix.

Even after the 800 or 900 C annealing cycles, the average second phase particle size was <20 nm, most particles <10 nm.

6) Second phase particle sizes after annealing were strongly coupled to the matrix morphology, with particles near a grain surface being generally smaller than those in the grain interior or within a particularly dense coating. This non-uniform particle size distribution occurred because of O incorporation (enhanced by ion bombardment) into the near surface regions of the grains.

7) The matrix and second phase morphologies in HIPped alloys were dependent on the as-deposited alloy morphology. Ta second phase particle sizes remained small after HIPping, <10 to 20 nm in the grain interiors, 20 to 50 nm at matrix grain boundaries in regions which underwent small plastic strains, and 100 to 400 nm at matrix grain boundaries in regions which underwent large plastic strains. Because of the uniformity of plastic deformation during HIPping, dense coatings with uniform void structures promoted the formation of spatially uniform distributions of Ta particles with narrow size distributions. The HIPped alloys exhibited greater second phase coarsening than did the encapsulated and annealed alloys. The bias deposited alloys showed superior resistance to particle coarsening, during annealing and HIP consolidation.

8) Coarsening of the Ta particles in the annealed alloys was by the Ostwald diffusion-based and surface energy-driven mechanism. Coarsening of the Ta particles in the HIPped alloys was by a combination of the Ostwald mechanism and collisional coalescence. The degree of coalescence was directly dependent on the extent of local plastic strain. It is believed that HIPping accelerated diffusional coarsening in regions of low plastic strain by increasing the local defect density relative to that present in the alloys annealed without applied stress.

APPENDIX

DEPOSITION DATA AND SPANNING COMPOSITIONS

This appendix presents the deposition data for all the coatings made in conjunction with those used in generating data for this thesis.

Run # 01 X = Cr Substrate bias = 1000 W
Cu source power = 4.0 kW X source power = 1.0 kW
minimum X content = 57.2 at. % maximum X content = 92.6 at. %
Comments: Nonstandard substrate holder orientation.

Run # 02 X = Cr Substrate bias = 0 W
Cu source power = 4.0 kW X source power = 0.5 kW
minimum X content = 16.3 at. % maximum X content = 59.8 at. %
Comments: Nonstandard substrate holder orientation.

Run # 03 X = Cr Substrate bias = 1000 W
Cu source power = 4.0 kW X source power = 0.5 kW
minimum X content = at. % maximum X content = at. %
Comments: Nonstandard substrate holder orientation. Near zero net deposition.

Run # 04 X = Cr Substrate bias = 200 W
Cu source power = 4.0 kW X source power = 0.5 kW
minimum X content = 9.1 at. % maximum X content = 52.7 at. %
Comments: Nonstandard substrate holder orientation.

Run # 05 X = Nb Substrate bias = 200 W
Cu source power = 4.0 kW X source power = 3.0 kW
minimum X content = 3.3 at. % maximum X content = 19.1 at. %
Comments: Nonstandard substrate holder orientation.

Run # 06 X = Nb Substrate bias = 0 W
Cu source power = 4.0 kW X source power = 3.0 kW
minimum X content = 4.0 at. % maximum X content = 24.4 at. %
Comments: Nonstandard substrate holder orientation.

Run # 07 X = Ta Substrate bias = 200 W
Cu source power = 4.0 kW X source power = 9.0 kW
minimum X content = 94.8 at. % maximum X content = 100.0 at. %
Comments: Nonstandard substrate holder orientation.

Run # 08 X = Ta Substrate bias = 200 W
Cu source power = 4.0 kW X source power = 6.0 kW
minimum X content = 0.7 at. % maximum X content = 14.4 at. %
Comments: Nonstandard substrate holder orientation.

Run # 09 X = Ta Substrate bias = 0 W
Cu source power = 4.0 kW X source power = 6.0 kW

minimum X content = 1.2 at. % maximum X content = 11.6 at. %
Comments: Nonstandard substrate holder orientation.

Run # 10 X=Ta Substrate bias = 50 W
Cu source power = 4.0 kW X source power = 6.0 kW
minimum X content = 9.6 at. % maximum X content = 29.9 at. %
Comments: Beginning of runs aligned on a standard substrate holder orientation.

Run # 11 X=Ta Substrate bias = 0 W
Cu source power = 4.0 kW X source power = 6.0 kW
minimum X content = 5.5 at. % maximum X content = 26.4 at. %

Run # 12 X=Ta Substrate bias = 95 W
Cu source power = 4.0 kW X source power = 6.0 kW
minimum X content = 30.5 at. % maximum X content = 64.9 at. %

Run # 13 X=Ta Substrate bias = 72 W
Cu source power = 4.0 kW X source power = 6.0 kW
minimum X content = 63.0 at. % maximum X content = 75.8 at. %

Run # 14 X=Ta Substrate bias = 0 W
Cu source power = 4.0 kW X source power = 6.0 kW
minimum X content = at. % maximum X content = at. %
Comments: Layered structure; 4 minute pulses with 1 minute overlaps.

Run # 15 X=Ta Substrate bias = 100 W
Cu source power = 4.0 kW X source power = 6.0 kW
minimum X content = at. % maximum X content = at. %
Comments: Layered structure; 4 minute pulses with 1 minute overlaps.

Run # 16 X=Ta Substrate bias = 0 W
Cu source power = 4.0 kW X source power = 6.0 kW
minimum X content = at. % maximum X content = at. %
Comments: Layered structure; 8 minute layers with 1 minute overlaps.

Run # 17 X=Ta Substrate bias = 100 W
Cu source power = 4.0 kW X source power = 6.0 kW
minimum X content = at. % maximum X content = at. %
Comments: Layered structure; 8 minute layers with 1 minute overlaps.

Run # 18 X=Ta Substrate bias = 100 W
Cu source power = 4.0 kW X source power = 6.0 kW
minimum X content = 4.3 at. % maximum X content = 21.2 at. %

Run # 19 X=Ta Substrate bias = 100 W
Cu source power = 4.0 kW X source power = 6.35 kW
minimum X content = 8.3 at. % maximum X content = 34.8 at. %

Run # 20 X=Ta Substrate bias = 0 W
Cu source power = 4.0 kW X source power = 6.35 kW
minimum X content = 7.9 at. % maximum X content = 30.5 at. %

Run # 21 X=Ta Substrate bias = 0 W
Cu source power = 4.0 kW X source power = 6.0 kW

minimum X content = 8.8 at. % maximum X content = 35.2 at. %

Run # 22 X = Ta Substrate bias = 0 W
Cu source power = 4.2 kW X source power = 6.0 kW
minimum X content = 2.9 at. % maximum X content = 14.4 at. %

Run # 23 X = Ta Substrate bias = 0 W
Cu source power = 4.2 kW X source power = 5.8 kW
minimum X content = 5.7 at. % maximum X content = 22.8 at. %

Run # 24 X = Ta Substrate bias = 0 W
Cu source power = 4.4 kW X source power = Ta kW
minimum X content = 1.2 at. % maximum X content = 6.4 at. %

Run # 25 X = Ta Substrate bias = 0 W
Cu source power = 4.0 kW X source power = 6.6 kW
minimum X content = 14.1 at. % maximum X content = 44.3 at. %

Run # 26 X = Cr Substrate bias = 100 W
Cu source power = 4.2 kW X source power = 0.4 kW
minimum X content = 0.3 at. % maximum X content = 6.8 at. %

Run # 27 X = Cr Substrate bias = 100 W
Cu source power = 4.2 kW X source power = 0.45 kW
minimum X content = 3.4 at. % maximum X content = 24.7 at. %

Run # 28 X = Cr Substrate bias = 100 W
Cu source power = 4.2 kW X source power = 0.6 kW
minimum X content = 10.0 at. % maximum X content = 46.8 at. %

Run # 29 X = Cr Substrate bias = 100 W
Cu source power = 4.2 kW X source power = 0.5 kW
minimum X content = 4.4 at. % maximum X content = 35.7 at. %

Run # 30 X = Cr Substrate bias = 100 W
Cu source power = 4.2 kW X source power = 0.4 kW
minimum X content = 0.5 at. % maximum X content = 3.1 at. %

Run # 31 X = Cr Substrate bias = 100 W
Cu source power = 4.2 kW X source power = 0.4 kW
minimum X content = 0.2 at. % maximum X content = 2.0 at. %

Run # 32 X = Cr Substrate bias = 100 W
Cu source power = 4.2 kW X source power = 0.6 kW
minimum X content = 1.4 at. % maximum X content = 16.0 at. %

Run # 33 X = Cr Substrate bias = 100 W
Cu source power = 4.2 kW X source power = 0.6 kW
minimum X content = 11.5 at. % maximum X content = 50.1 at. %

Run # 34 X = Cr Substrate bias = 0 W
Cu source power = 4.2 kW X source power = 0.6 kW
minimum X content = 6.1 at. % maximum X content = 30.6 at. %

Run # 35 X = Cr Substrate bias = 0 W
Cu source power = 4.2 kW X source power = 0.6 kW
minimum X content = 1.8 at. % maximum X content = 14.6 at. %

Run # 36 X = Cr Substrate bias = 0 W
Cu source power = 4.2 kW X source power = 0.4 kW
minimum X content = 0.2 at. % maximum X content = 0.5 at. %

Run # 37 X = Cr Substrate bias = 0 W
Cu source power = 4.2 kW X source power = 0.6 kW
minimum X content = 0.2 at. % maximum X content = 0.8 at. %

Run # 38 X = Cr Substrate bias = 0 W
Cu source power = 4.2 kW X source power = 0.5 kW
minimum X content = 3.0 at. % maximum X content = 14.2 at. %

Run # 39 X = Cr Substrate bias = 0 W
Cu source power = 4.2 kW X source power = 0.4 kW
minimum X content = 2.7 at. % maximum X content = 14.2 at. %

Run # 40 X = Cr Substrate bias = 0 W
Cu source power = 4.2 kW X source power = 0.4 kW
minimum X content = 0.3 at. % maximum X content = 2.2 at. %

Run # 41 X = Cr Substrate bias = 0 W
Cu source power = 4.2 kW X source power = 0.45 kW
minimum X content = 0.4 at. % maximum X content = 1.6 at. %
Comments:

Run # 42 X = Cr Substrate bias = 100 W
Cu source power = 4.2 kW X source power = 0.5 kW
minimum X content = at. % maximum X content = at. %
Comments: Layered structure; 4 minute layers with 1 minute overlap.

Run # 43 X = Cr Substrate bias = 0 W
Cu source power = 4.2 kW X source power = 0.5 kW
minimum X content = at. % maximum X content = at. %
Comments: Layered structure; 4 minute layers with 1 minute overlap.

Run # 44 X = Cr Substrate bias = 100 W
Cu source power = 4.2 kW X source power = 0.5 kW
minimum X content = at. % maximum X content = at. %
Comments: Layered structure; 8 minute layers with 1 minute overlap.

Run # 45 X = Cr Substrate bias = 0 W
Cu source power = 4.2 kW X source power = 0.5 kW
minimum X content = at. % maximum X content = at. %
Comments: Layered structure; 8 minute layers with 1 minute overlap.

Run # 46 X = Ta Substrate bias = 100 W
Cu source power = 4.2 kW X source power = 6.0 kW
minimum X content = 1.2 at. % maximum X content = 8.7 at. %
Comments: Aborted run attempted to incorporate nitrogen.

Run # 47 X = Ta Substrate bias = 100 W
 Cu source power = 4.2 kW X source power = 6.0 kW
 minimum X content = at. % maximum X content = at. %
 Comments: Aborted run multilayer, multithickness.

Run # 48 X = Ta Substrate bias = 100 W
 Cu source power = 4.2 kW X source power = 6.0 kW
 minimum X content = at. % maximum X content = at. %
 Comments: Multilayer, multithickness.

Run # 49 X = Ta Substrate bias = 100 W
 Cu source power = 4.0 kW X source power = 6.0 kW
 minimum X content = 2.3 at. % maximum X content = 14.4 at. %
 minimum Al content = 1.0 at % maximum Al content = 1.43 at. %
 Comments: Small aluminum addition to the Cu charge.

X-RAY DIFFRACTION SCANS

This appendix is a compilation of representative x-ray diffraction data for the as-deposited and heat treated specimens used in this thesis. Two-theta (2Θ) values are in degrees, maximum intensities (Imax) are in thousands of counts, and d spacings are in angstroms.

Table 5. Table of x-ray diffraction data for as-deposited specimen {2,2} from run 18.

<u>2Θ</u>	Imax	d	comments
38.46	1.620	2.339	(110) Ta bcc
43.32	144.3	2.087	(111) Cu
50.46	218.7	1.807	(200) Cu
74.12	633.5	1.278	(220) Cu
89.94	55.25	1.090	(311) Cu
95.16	5.023	1.043	(222) Cu

Table 6. Table of x-ray diffraction data for as-deposited specimen {2,6} from run 18.

<u>2Θ</u>	Imax	d	comments
38.38	4.032	2.343	(110) Ta bcc
43.34	63.50	2.086	(111) Cu
50.46	103.2	1.807	(200) Cu
71.14	33.58	1.278	(220) Cu
89.96	30.54	1.090	(311) Cu
95.18	3.698	1.043	(222) Cu

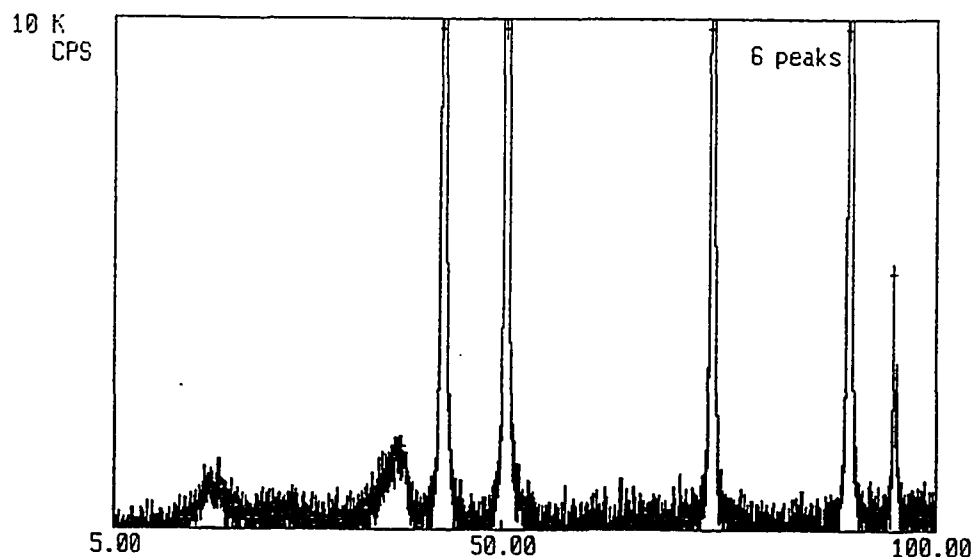


Figure 56. X-ray diffraction scan of as-deposited specimen {2,2} from run 18.

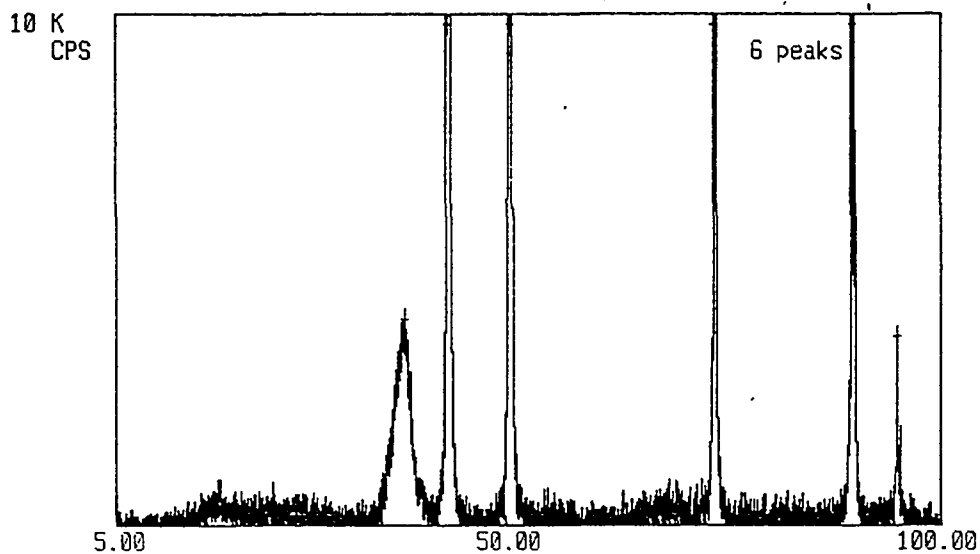


Figure 57. X-ray diffraction scan of as-deposited specimen {2,6} from run 18.

Table 7. Table of x-ray diffraction data for as-deposited specimen {2,2} from run 23.

<u>2Θ</u>	I _{max}	d	comments
38.50	4.233	2.336	(110) Ta bcc
43.30	170.9	2.088	(111) Cu
50.42	182.1	1.808	(200) Cu
74.10	39.30	1.278	(220) Cu
89.90	47.58	1.090	(311) Cu
95.12	8.384	1.044	(222) Cu

Table 8. Table of x-ray diffraction data for as-deposited specimen {2,6} from run 23.

<u>2Θ</u>	I _{max}	d	comments
34.00	1.844	2.635	Ta oxide
36.50	2.268	2.460	Ta oxide
38.58	5.513	2.332	(110) Ta bcc
40.34	31.29	2.234	Ta oxide
43.30	106.1	2.088	(111) Cu
50.44	170.2	1.808	(200) Cu
65.30	1.369	1.428	Ta oxide
74.32	24.67	1.275	(220) Cu
89.92	38.61	1.090	(311) Cu
95.14	5.644	1.044	(222) Cu

Table 9. Table of x-ray diffraction data for specimen {2,2} from run 18 after heat treatment for 1 hour at 800 C.

<u>2Θ</u>	I _{max}	d	comments
22.88	3.600	3.884	Ta oxide
28.50	2.280	3.129	Ta oxide
36.80	2.538	2.440	Ta oxide
38.56	2.268	2.333	(110) Ta
43.26	147.9	2.090	(111) Cu
50.38	72.09	1.810	(200) Cu
55.64	1.238	1.651	(200) Ta or Ta oxide
74.06	116.5	1.279	(220) Cu
89.88	11.21	1.091	(311) Cu
95.06	2.776	1.044	(222) Cu

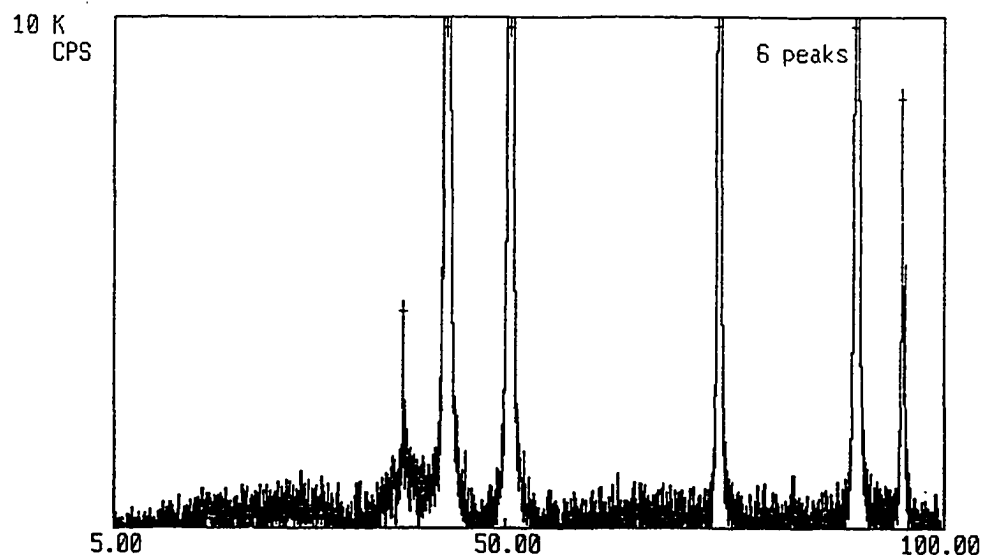


Figure 58. X-ray diffraction scan of as-deposited specimen {2,2} from run 23.

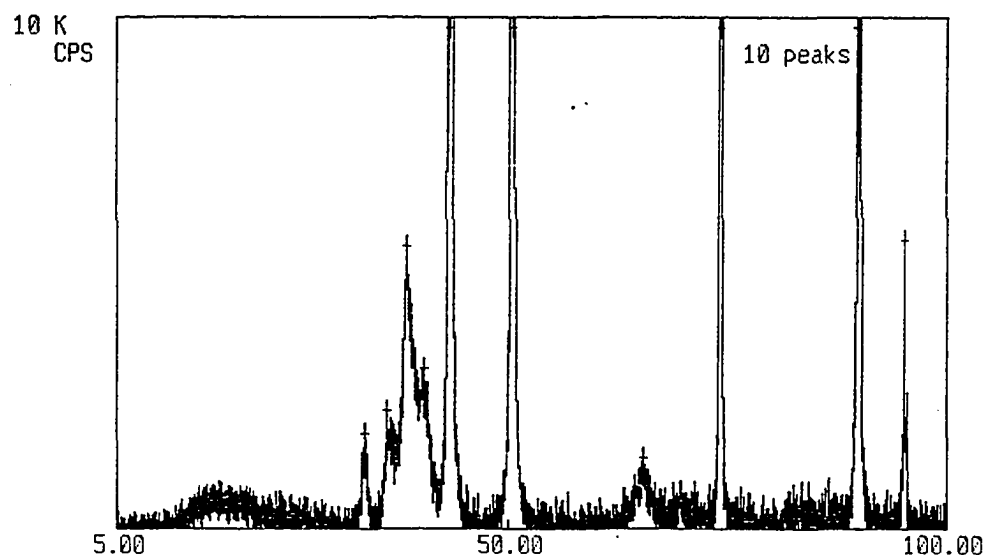


Figure 59. X-ray diffraction scan of as-deposited specimen {2,6} from run 23.

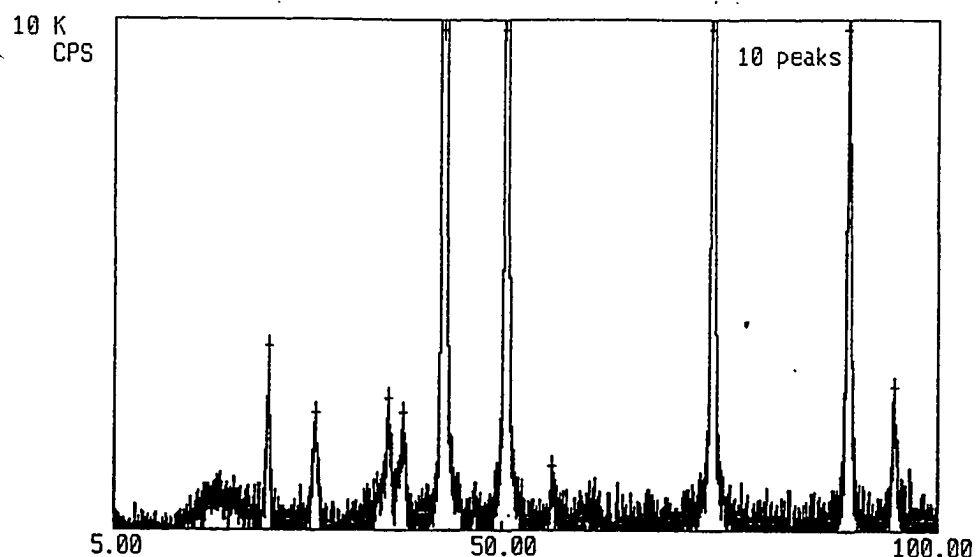


Figure 60. X-ray diffraction scan of specimen {2,2} from run 18 after heat treatment for 1 hour at 800 C.

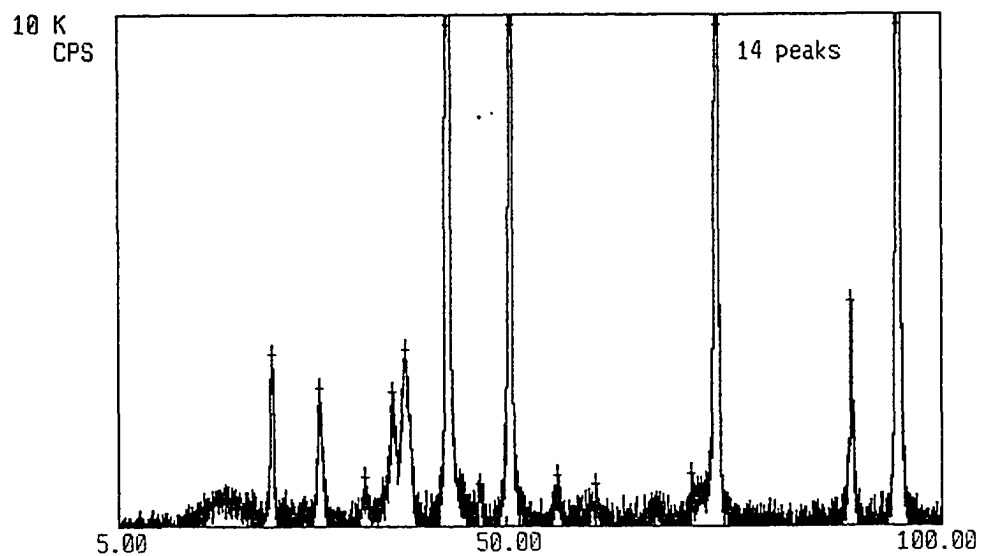


Figure 61. X-ray diffraction scan of specimen {2,6} from run 18 after heat treatment for 1 hour at 800 C.

Table 10. Table of x-ray diffraction data for specimen {2,6} from run 18 after heat treatment for 1 hour at 800 C.

<u>2θ</u>	I _{max}	d	comments
23.00	3.342	3.864	Ta oxide
28.52	2.678	3.127	Ta oxide
33.62	0.942	2.664	Ta oxide
36.90	2.614	2.434	Ta oxide
38.38	3.437	2.343	(110) Ta
43.32	356.3	2.087	(111) Cu
46.96	0.830	1.933	Ta oxide
50.44	27.76	1.808	(200) Cu
55.76	0.996	1.647	Ta oxide
60.10	0.802	1.538	Ta oxide
71.30	1.000	1.322	(311) fcc Ta or Ta oxide
74.30	33.12	1.276	(220) Cu
89.92	4.389	1.090	(311) Cu
95.12	129.3	1.044	(222) Cu

Table 11. Table of x-ray diffraction data for specimen {2,2} from run 23 after heat treatment for 1 hour at 800 C.

<u>2θ</u>	I _{max}	d	comments
28.38	1.416	3.142	Ta oxide
36.66	1.364	2.449	Ta oxide
38.50	19.95	2.336	(110) Ta bcc
43.28	123.2	2.089	(111) Cu
50.42	45.53	1.808	(200) Cu
55.58	2.364	1.652	(200) Ta bcc
69.64	4.001	1.349	(211) Ta bcc
74.08	19.48	1.279	(220) Cu
82.48	1.364	1.169	(220) Ta
89.96	10.99	1.090	(311) Cu
95.14	4.340	1.044	(222) Cu

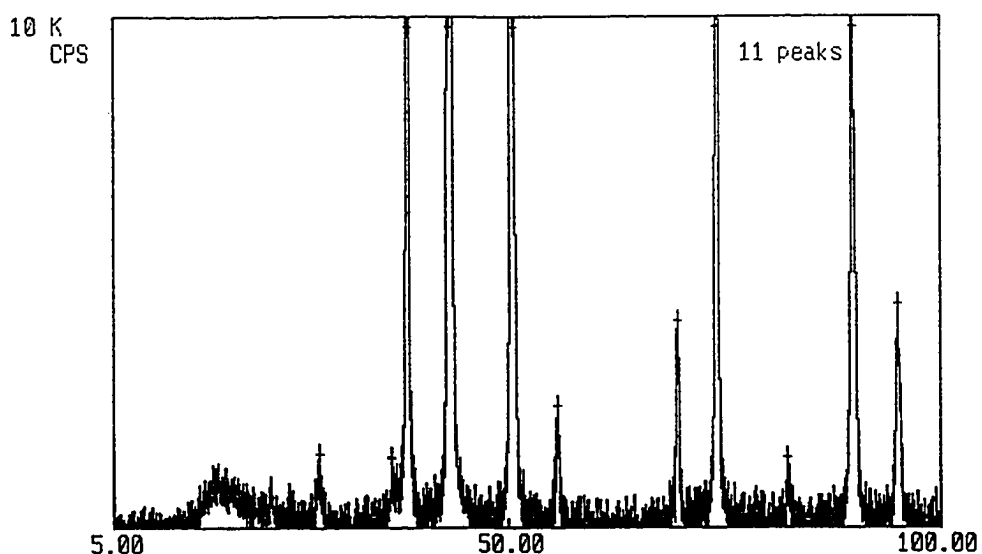


Figure 62. X-ray diffraction scan of specimen {2,2} from run 23 after heat treatment for 1 hour at 800 C.

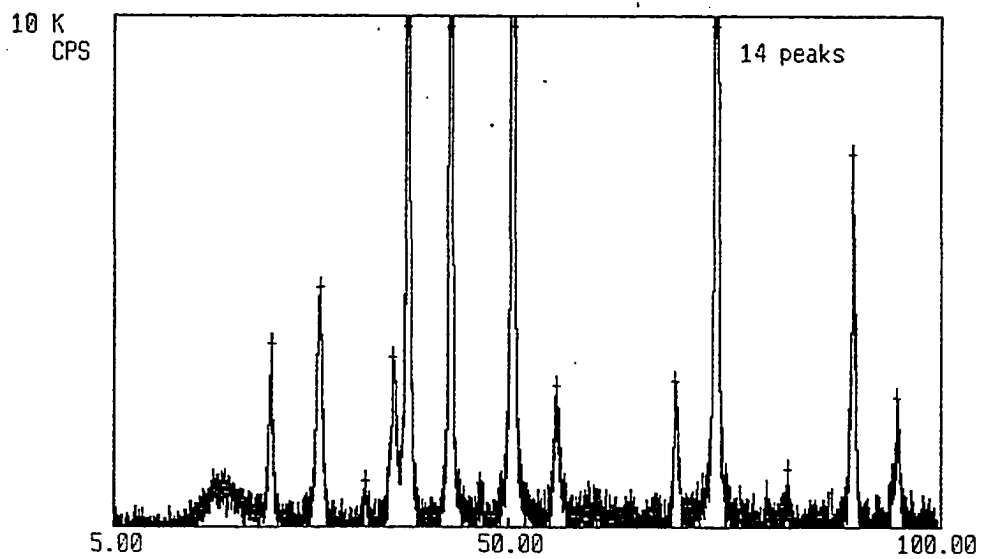


Figure 63. X-ray diffraction scan of specimen {2,6} from run 23 after heat treatment for 1 hour at 800 C.

Table 12. Table of x-ray diffraction data for specimen {2,6} from run 23 after heat treatment for 1 hour at 800 C.

<u>2θ</u>	I _{max}	d	comments
22.88	3.600	3.884	Ta oxide
28.38	4.692	3.142	Ta oxide
33.50	0.881	2.673	Ta oxide
36.68	3.306	2.448	(111) Ta fcc or Ta oxide
38.40	17.13	2.342	(110) Ta bcc
43.26	55.99	2.090	(111) Cu
46.76	0.837	1.941	Ta oxide
50.42	155.9	1.808	(200) Cu
55.44	2.763	1.656	(200) Ta bcc or Ta oxide
69.38	2.849	1.353	(211) Ta bcc
74.02	104.5	1.280	(220) Cu
82.46	1.106	1.169	(220) Ta bcc
89.90	72.89	1.090	(311) Cu
95.04	2.531	1.044	(222) Cu

Table 13. Table of x-ray diffraction data for specimen {6,2} from run 18 after heat treatment for 10 hours at 800 C.

<u>2θ</u>	I _{max}	d	comments
22.90	2.292	3.880	Ta oxide
28.40	2.093	3.140	Ta oxide
35.38	1.251	2.535	(111) Ta fcc or Ta oxide
36.82	2.116	2.439	(111) Ta fcc or Ta oxide
38.38	1.364	2.343	(110) Ta bcc
43.28	70.26	2.089	(111) Cu
50.42	30.10	1.808	(200) Cu
55.60	1.040	1.652	(200) Ta bcc
74.06	26.57	1.279	(220) Cu
89.96	7.364	1.090	(311) Cu
95.10	1.876	1.044	(222) Cu

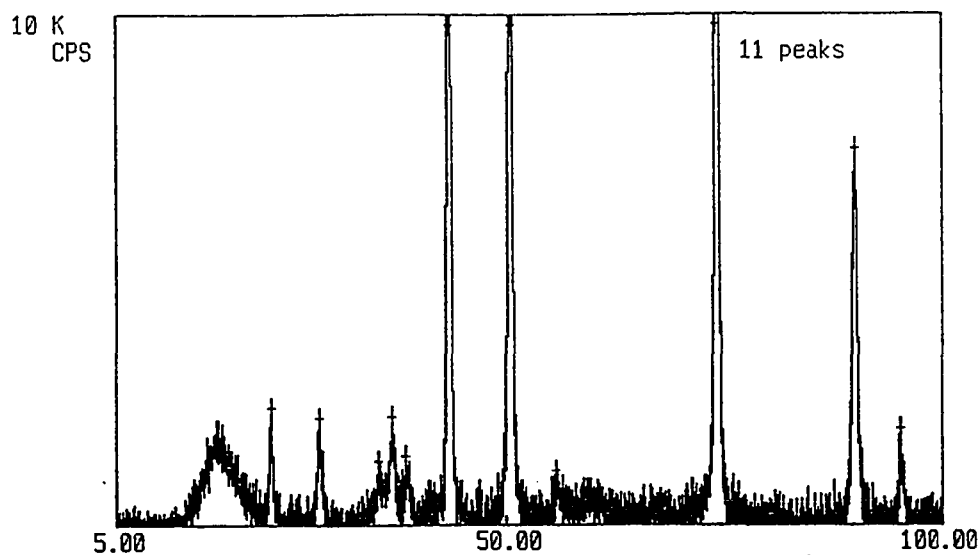


Figure 64. X-ray diffraction scan of specimen {6,2} from run 18 after heat treatment for 10 hours at 800 C.

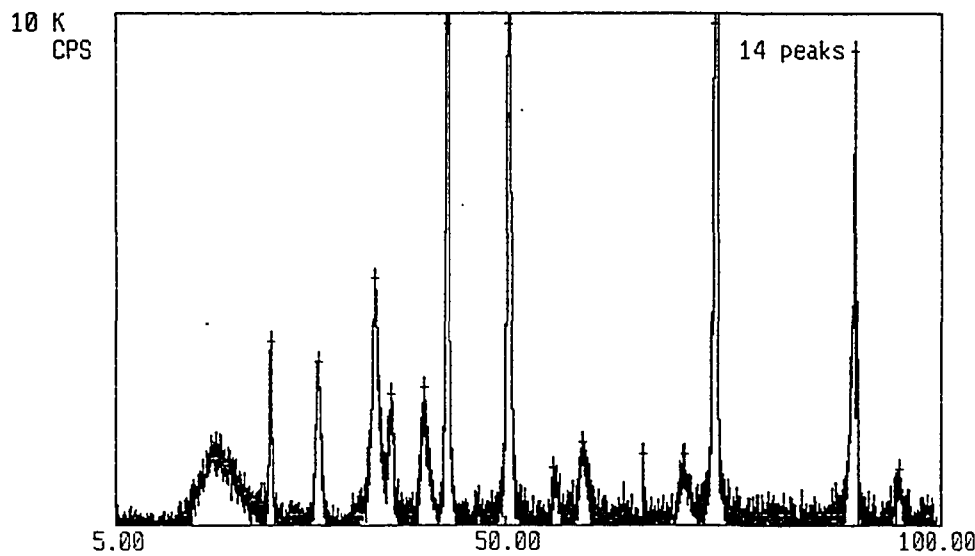


Figure 65. X-ray diffraction scan of specimen {6,6} from run 18 after heat treatment for 10 hours at 800 C.

Table 14. Table of x-ray diffraction data for specimen {6,6} from run 18 after heat treatment for 10 hours at 800 C.

<u>2θ</u>	I _{max}	d	comments
22.86	3.570	3.887	Ta oxide
28.40	3.199	3.140	Ta oxide
34.96	4.813	2.564	Ta oxide
36.78	2.544	2.442	(111) Ta fcc or Ta oxide
40.56	2.678	2.222	(200) Ta fcc or Ta oxide
43.26	33.90	2.090	(111) Cu
50.30	41.00	1.813	(200) Cu
55.52	1.118	1.654	(200) Ta bcc or Ta oxide
58.86	1.630	1.568	(220) Ta fcc or Ta oxide
65.96	1.378	1.415	Ta oxide
70.58	1.378	1.333	(311) Ta fcc or Ta oxide
74.08	117.6	1.279	(220) Cu
90.16	9.264	1.088	(311) Cu
95.18	1.068	1.043	(222) Cu or (310) Ta bcc

Table 15. Table of x-ray diffraction data for specimen {6,2} from run 23 after heat treatment for 10 hours at 800 C.

<u>2θ</u>	I _{max}	d	comments
22.84	3.466	3.890	Ta oxide
28.24	2.882	3.158	Ta oxide
33.84	1.351	2.647	Ta oxide
36.30	4.331	2.473	(111) Ta fcc or Ta oxide
38.56	8.100	2.333	(110) Ta bcc
43.28	135.5	2.089	(111) Cu
50.42	51.13	1.808	(200) Cu
55.56	1.143	1.653	(200) Ta bcc
58.76	0.973	1.570	Ta oxide
60.54	1.369	1.528	Ta oxide
66.88	1.506	1.398	Ta oxide
74.10	25.24	1.278	(220) Cu
89.92	12.66	1.090	(311) Cu
95.08	3.729	1.044	(222) Cu or (310) Ta bcc

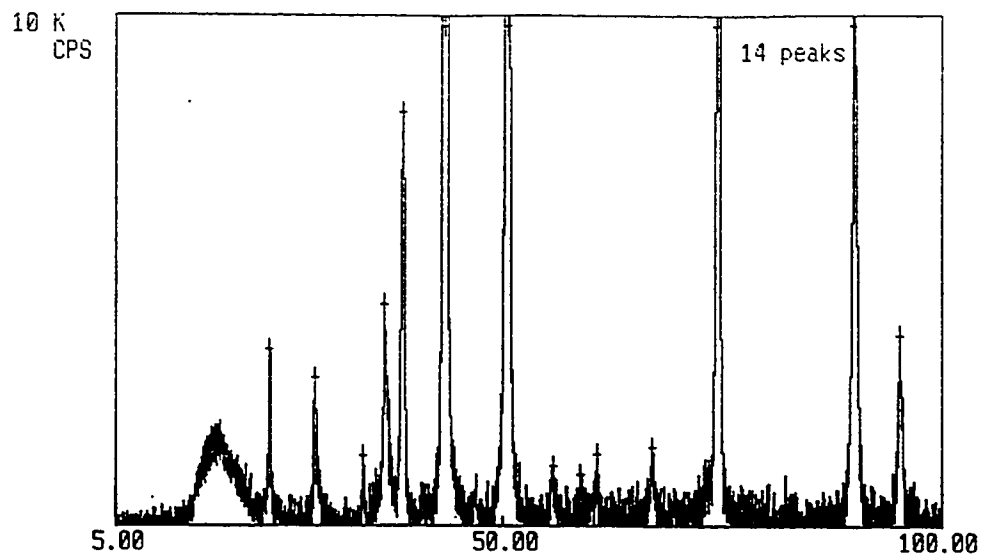


Figure 66. X-ray diffraction scan of specimen {6,2} from run 23 after heat treatment for 10 hours at 800 C.

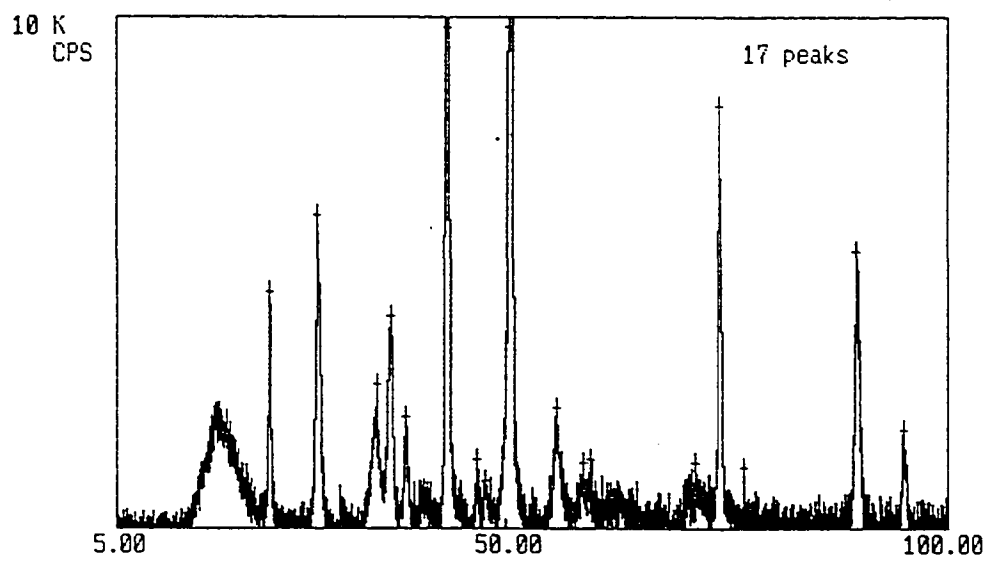


Figure 67. X-ray diffraction scan of specimen {6,6} from run 23 after heat treatment for 10 hours at 800 C.

Table 16. Table of x-ray diffraction data for specimen {6,6} from run 23 after heat treatment for 10 hours at 800 C.

<u>2θ</u>	I _{max}	d	comments
22.82	4.624	3.894	Ta oxide
28.28	6.104	3.153	Ta oxide
35.26	2.802	2.543	(111) Ta fcc or Ta oxide
36.82	4.144	2.439	(111) Ta fcc or Ta oxide
38.52	2.197	2.335	(110) Ta bcc
43.28	95.60	2.089	(111) Cu
46.62	1.346	1.947	Ta oxide
47.56	0.911	1.910	Ta oxide
50.40	46.98	1.809	(200) Cu
55.58	2.352	1.652	(200) Ta bcc
58.74	1.287	1.571	Ta oxide
59.52	1.337	1.552	(220) Ta fcc or Ta oxide
71.28	1.287	1.322	(311) Ta fcc or Ta oxide
74.06	8.258	1.279	(220) Cu
76.84	1.186	1.240	(222) Ta fcc or Ta oxide
89.90	5.411	1.090	(311) Cu
95.06	1.920	1.044	(222) Cu or (310) Ta bcc

Table 17. Table of x-ray diffraction data for specimen {6,2} from run 18 after heat treatment for 100 hours at 800 C.

<u>2θ</u>	I _{max}	d	comments
22.92	1.615	3.877	Ta oxide
28.22	1.411	3.160	Ta oxide
33.54	1.097	2.670	Ta oxide
36.44	1.969	2.464	(111) Ta fcc or Ta oxide
38.58	4.168	2.332	(110) Ta bcc
43.28	84.75	2.089	(111) Cu
50.40	26.69	1.809	(200) Cu
67.12	1.182	1.393	Ta oxide
74.06	17.91	1.279	(220) Cu
79.36	34.74	1.206	(222) Ta fcc or Ta oxide
89.90	611.3	1.090	(311) Cu
95.06	1.686	1.044	(222) Cu or (310) Ta bcc

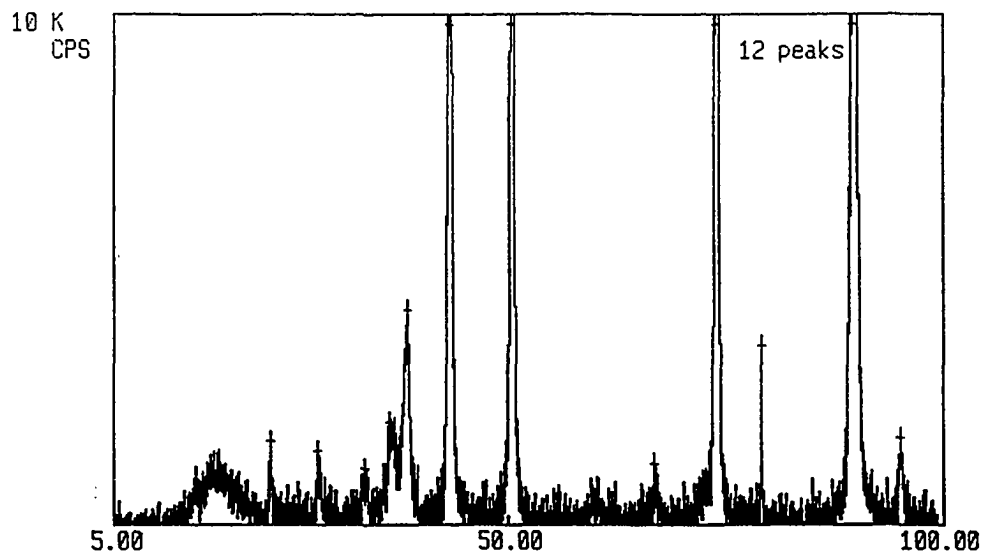


Figure 68. X-ray diffraction scan of specimen {6,2} from run 18 after heat treatment for 100 hours at 800 C.

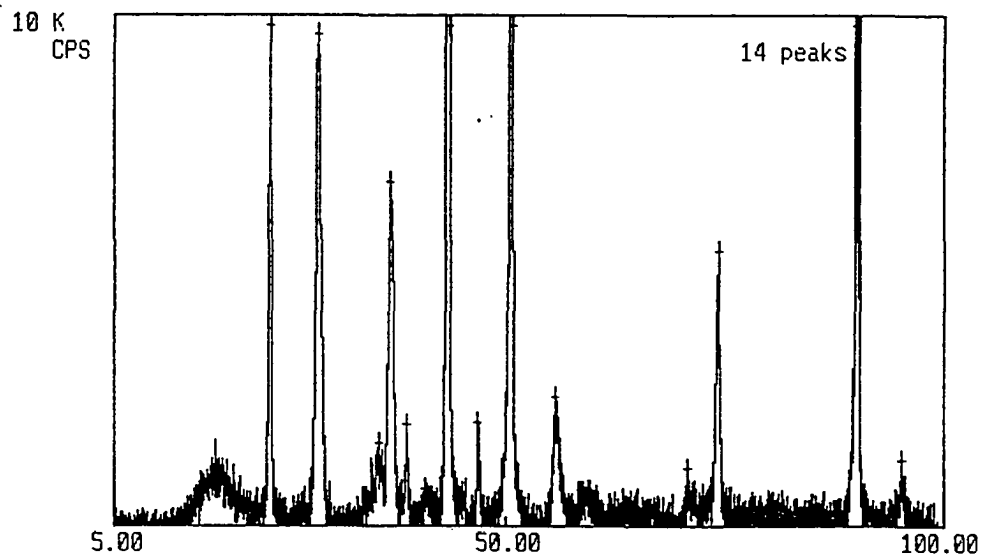


Figure 69. X-ray diffraction scan of specimen {6,6} from run 18 after heat treatment for 100 hours at 800 C.

Table 18. Table of x-ray diffraction data for specimen {6,6} from run 18 after heat treatment for 100 hours at 800 C.

<u>2θ</u>	I _{max}	d	comments
22.96	9.851	3.870	Ta oxide
28.46	9.604	3.134	Ta oxide
35.46	1.620	2.529	(111) Ta fcc or Ta oxide
36.82	6.704	2.439	(111) Ta fcc or Ta oxide
38.72	1.986	2.324	(110) Ta bcc
40.72	0.726	2.214	(200) Ta fcc or Ta oxide
43.38	45.29	2.084	(111) Cu
46.78	2.003	1.940	Ta oxide
50.64	18.70	1.801	(200) Cu
55.64	2.506	1.651	(200) Ta bcc or Ta oxide
70.84	1.106	1.329	(311) Ta fcc or Ta oxide
74.20	5.375	1.277	(220) Cu
89.96	60.58	1.090	(311) Cu
95.22	1.287	1.043	(310) Ta bcc or (222) Cu

Table 19. Table of x-ray diffraction data for specimen {6,2} from run 23 after heat treatment for 100 hours at 800 C.

<u>2θ</u>	I _{max}	d	comments
28.22	1.283	3.160	Ta oxide
37.16	1.278	2.418	(111) Ta fcc or Ta oxide
38.50	26.37	2.336	(110) Ta bcc
43.32	117.6	2.087	(111) Cu
45.34	1.615	1.999	Ta oxide
50.48	271.1	1.806	(200) Cu
55.64	2.395	1.651	(200) Ta bcc
69.66	3.721	1.349	(211) Ta bcc
74.16	11.25	1.278	(220) Cu
82.50	1.287	1.168	(220) Ta bcc
89.96	9.025	1.090	(311) Cu
95.12	3.752	1.044	(222) Cu

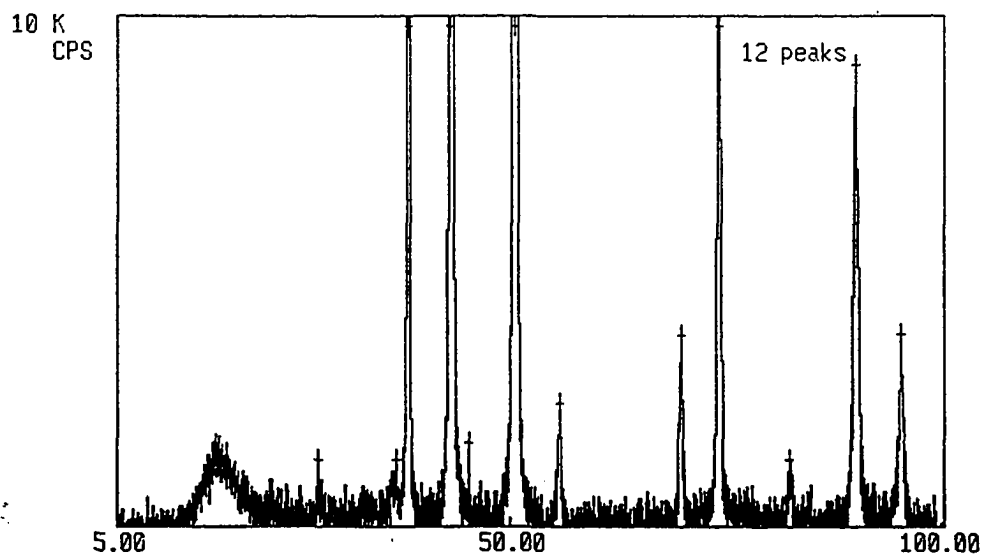


Figure 70. X-ray diffraction scan of specimen {6,2} from run 23 after heat treatment for 100 hours at 800 C.

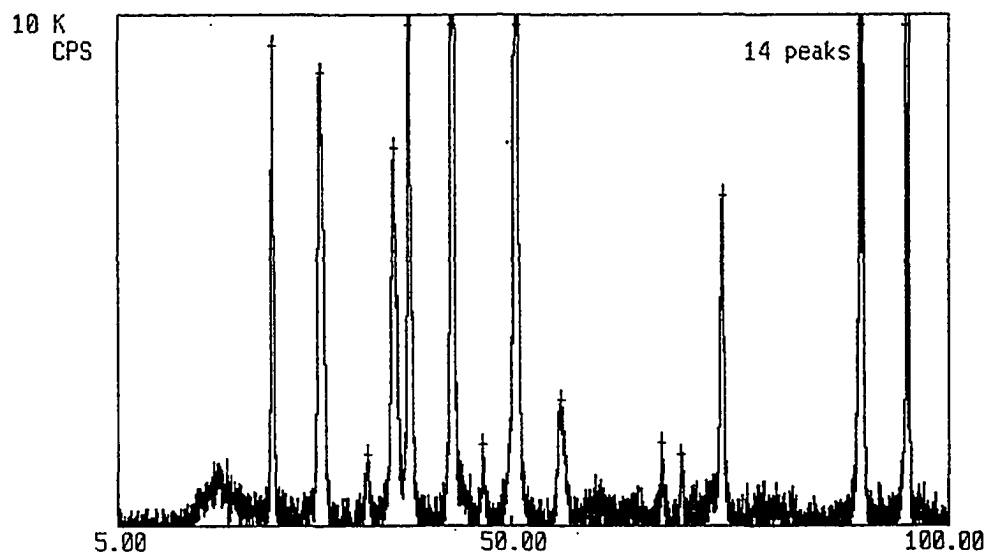


Figure 71. X-ray diffraction scan of specimen {6,6} from run 23 after heat treatment for 100 hours at 800 C.

Table 20. Table of x-ray diffraction data for specimen {6,6} from run 23 after heat treatment for 100 hours at 800 C.

<u>2θ</u>	I _{max}	d	comments
22.90	9.385	3.880	Ta oxide
28.44	8.836	3.136	Ta oxide
33.70	1.397	2.657	Ta oxide
36.76	7.396	2.443	(111) Ta fcc or Ta oxide
38.42	11.72	2.341	(110) Ta bcc
43.30	57.39	2.088	(111) Cu
46.76	1.590	1.941	Ta oxide
50.50	46.06	1.806	(200) Cu
55.56	2.450	1.653	(200) Ta bcc
67.10	1.610	1.394	Ta oxide
69.40	1.369	1.353	(211) Ta bcc
74.16	6.450	1.278	(220) Cu
89.96	37.10	1.090	(311) Cu
95.18	24.12	1.043	(222) Cu or (310) Ta bcc

Table 21. Table of x-ray diffraction data for specimen {5,2} from run 18 after heat treatment for 1 hour at 900 C.

<u>2θ</u>	I _{max}	d	comments
22.88	4.323	3.884	Ta oxide
28.32	5.814	3.149	Ta oxide
36.72	4.160	2.446	(111) Ta fcc or Ta oxide
43.34	72.56	2.086	(111) Cu
46.74	1.696	1.942	Ta oxide
50.50	105.0	1.806	(200) Cu
55.60	2.685	1.652	Ta oxide
74.14	169.6	1.278	(220) Cu
89.98	10.97	1.090	(311) Cu
95.12	31.08	1.044	(222)Cu or (310) Ta bcc

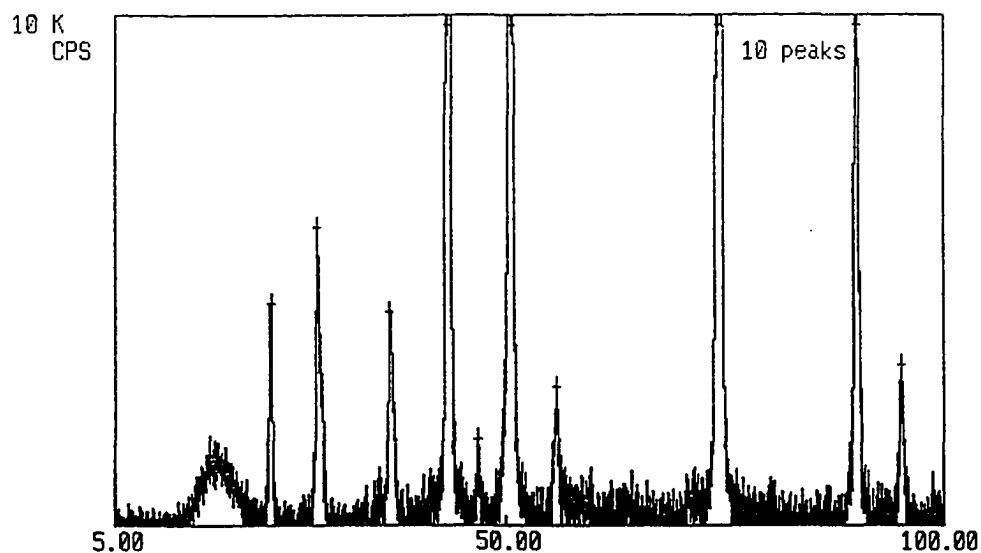


Figure 72. X-ray diffraction scan of specimen {5,2} from run 18 after heat treatment for 1 hour at 900 C.

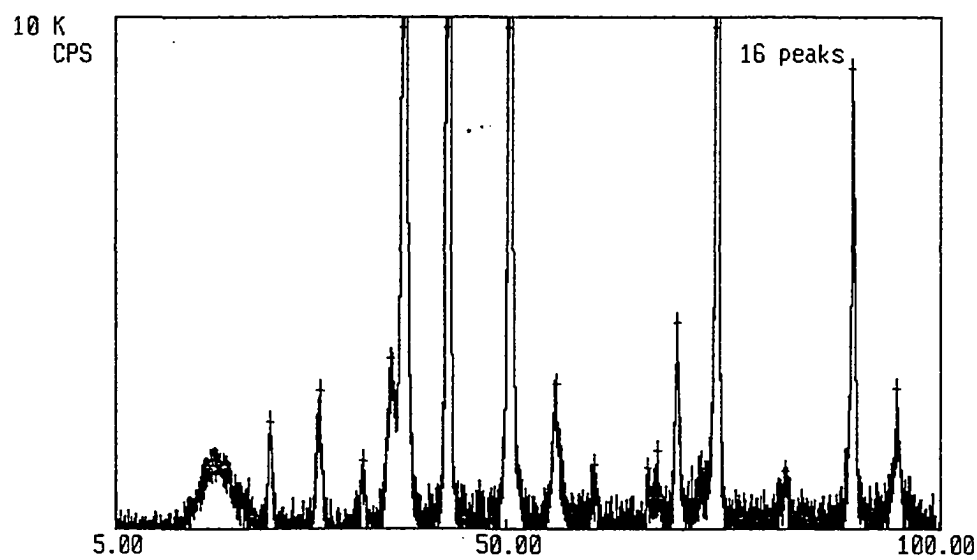


Figure 73. X-ray diffraction scan of specimen {5,6} from run 18 after heat treatment for 1 hour at 900 C.

Table 22. Table of x-ray diffraction data for specimen {5,6} from run 18 after heat treatment for 1 hour at 900 C.

<u>2θ</u>	I _{max}	d	comments
23.02	2.070	3.860	Ta oxide
28.58	2.672	3.121	Ta oxide
33.54	1.301	2.670	Ta oxide
36.86	3.328	2.437	(111) Ta fcc or Ta oxide
38.40	22.95	2.342	(110) Ta bcc
43.28	40.00	2.089	(111) Cu
50.40	24.03	1.809	(200) Cu
55.58	2.809	1.652	(200) Ta bcc
60.06	1.256	1.539	Ta oxide
66.12	1.195	1.412	Ta oxide
67.16	1.531	1.393	Ta oxide
69.54	4.032	1.351	(211) Ta bcc
74.14	24.73	1.278	(220) Cu
82.26	1.110	1.171	(220) Ta bcc
89.88	8.989	1.091	(311) Cu
95.00	2.724	1.045	(310) Ta bcc

Table 23. Table of x-ray diffraction data for specimen {5,2} from run 23 after heat treatment for 1 hour at 900 C.

<u>2θ</u>	I _{max}	d	comments
28.12	0.777	3.171	Ta oxide
38.52	23.99	2.335	(110) Ta bcc
43.36	102.7	2.085	(111) Cu
50.46	96.88	1.807	(200) Cu
55.74	3.533	1.648	(200) Ta bcc
69.74	6.440	1.347	(211) Ta bcc
74.16	16.85	1.278	(220) Cu
82.56	2.328	1.168	(220) Ta bcc
89.96	14.64	1.090	(311) Cu
92.88	1.073	1.063	Ta oxide ?
95.10	6.261	1.044	(222) Cu

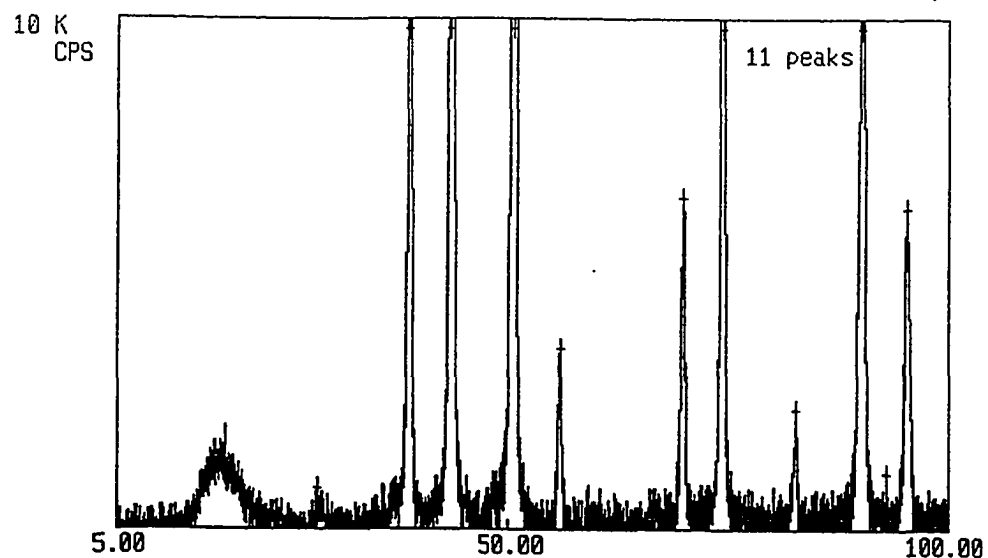


Figure 74. X-ray diffraction scan of specimen {5,2} from run 23 after heat treatment for 1 hour at 900 C.

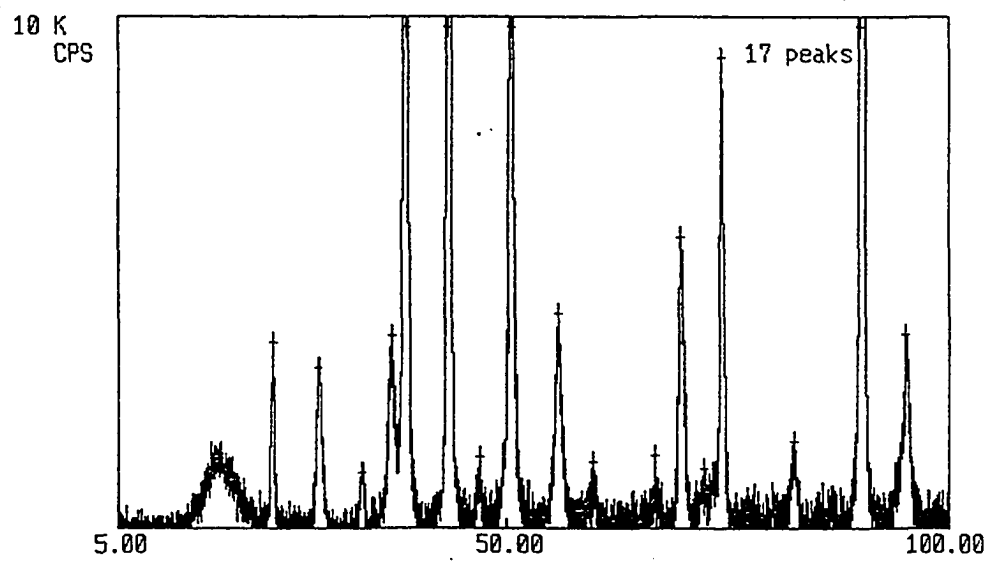


Figure 75. X-ray diffraction scan of specimen {5,6} from run 23 after heat treatment for 1 hour at 900 C.

Table 24. Table of x-ray diffraction data for specimen {5,6} from run 23 after heat treatment for 1 hour at 900 C.

<u>2θ</u>	I _{max}	d	comments
22.98	3.615	3.867	Ta oxide
28.32	3.129	3.149	Ta oxide
33.38	1.073	2.682	Ta oxide
36.76	3.744	2.443	(111) Ta fcc or Ta oxide
38.46	26.53	2.339	(110) Ta bcc
43.34	56.23	2.086	(111) Cu
46.90	1.388	1.936	Ta oxide
50.50	20.27	1.806	(200) Cu
55.54	4.193	1.653	(200) Ta bcc
59.66	1.287	1.549	(220) Ta fcc or Ta oxide
66.64	1.402	1.402	Ta oxide
69.50	5.681	1.351	(211) Ta bcc
72.20	1.156	1.307	Ta oxide
74.12	9.168	1.278	(220) Cu
82.38	1.676	1.170	(220) Ta bcc
89.86	57.00	1.091	(311) Cu
95.02	3.798	1.045	(310) Ta bcc or (222) Cu

Table 25. Table of x-ray diffraction data for specimen {5,2} from run 18 after heat treatment for 10 hours at 900 C.

<u>2θ</u>	I _{max}	d	comments
23.02	2.042	3.860	Ta oxide
28.44	1.822	3.136	Ta oxide
33.62	1.165	2.664	Ta oxide
36.82	2.672	2.439	(111) Ta fcc or Ta oxide
38.40	4.456	2.342	(110) Ta bcc
43.36	66.95	2.085	(111) Cu
47.02	1.114	1.931	Ta oxide
50.46	31.51	1.807	(200) Cu
55.58	1.420	1.652	(200) Ta bcc
60.32	1.296	1.533	Ta oxide
67.10	1.341	1.394	Ta oxide
74.16	18.77	1.278	(220) Cu
90.04	15.75	1.089	(311) Cu
95.18	3.087	1.043	(222) Cu or (310) Ta bcc

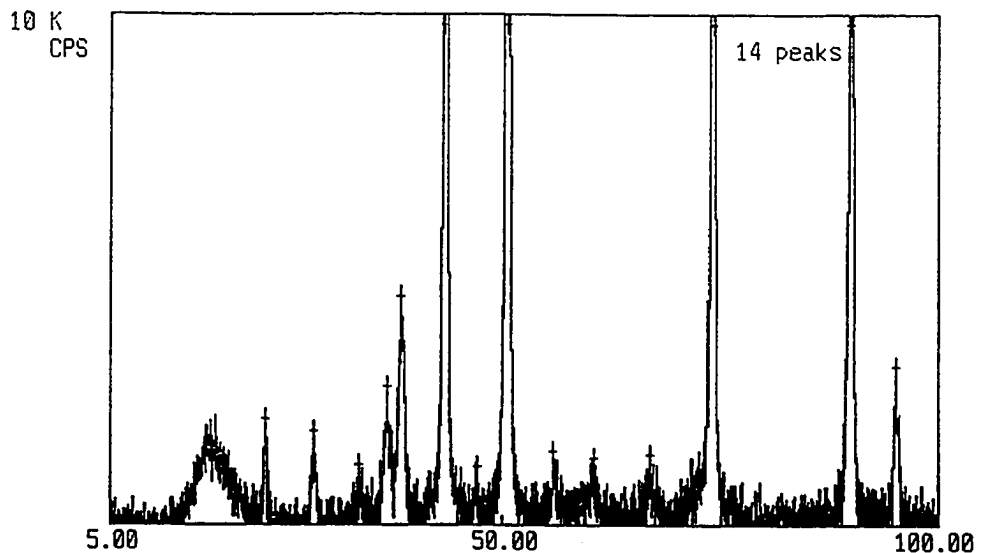


Figure 76. X-ray diffraction scan of specimen {5,2} from run 18 after heat treatment for 10 hours at 900 C.

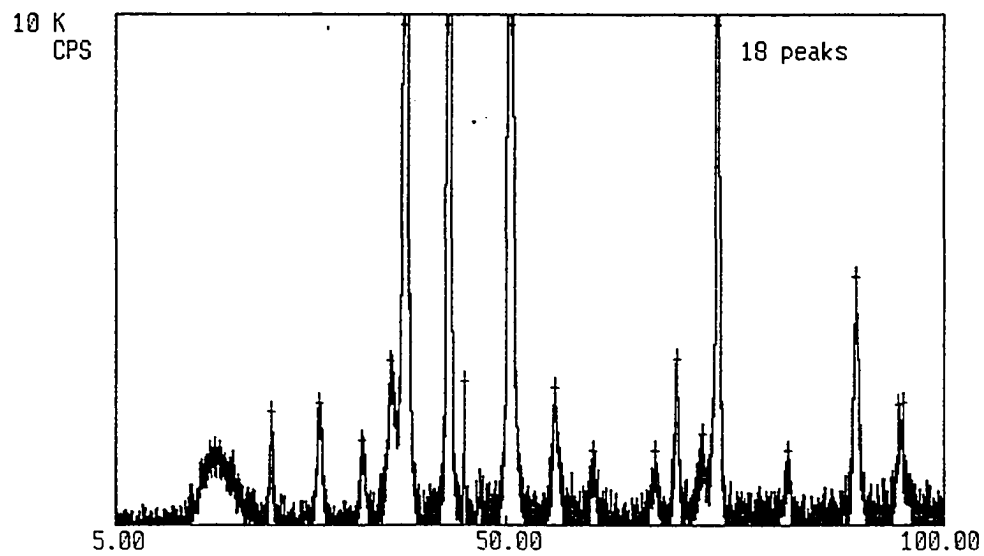


Figure 77. X-ray diffraction scan of specimen {5,6} from run 18 after heat treatment for 10 hours at 900 C.

Table 26. Table of x-ray diffraction data for specimen {5,6} from run 18 after heat treatment for 10 hours at 900 C.

<u>2θ</u>	I _{max}	d	comments
22.94	2.209	3.874	Ta oxide
28.50	2.389	3.129	Ta oxide
33.38	1.661	2.682	Ta oxide
36.62	3.213	2.452	(111) Ta fcc or Ta oxide
38.42	23.68	2.341	(110) Ta bcc
43.36	45.85	2.085	(111) Cu
45.14	2.802	2.007	Ta oxide
50.44	150.2	1.808	(200) Cu
55.38	2.691	1.658	Ta oxide
59.88	1.444	1.543	(220) Ta fcc or Ta oxide
67.00	1.458	1.396	Ta oxide
69.42	3.249	1.353	(211) Ta bcc
72.38	1.796	1.305	(311) Ta fcc or Ta oxide
74.02	14.48	1.280	(220) Cu
82.28	1.463	1.171	(220) Ta bcc
89.82	4.839	1.091	(311) Cu
94.86	2.352	1.046	(310) Ta bcc
95.26	2.395	1.043	(222) Cu or (310) Ta bcc

Table 27. Table of x-ray diffraction data for specimen {5,2} from run 23 after heat treatment for 10 hours at 900 C.

<u>2θ</u>	I _{max}	d	comments
36.92	1.160	2.433	(111) Ta fcc or Ta oxide
38.46	26.20	2.339	(110) Ta bcc
43.32	129.2	2.087	(111) Cu
50.48	49.40	1.806	(200) Cu
55.54	3.321	1.653	(200) Ta bcc
66.16	1.052	1.411	Ta oxide
69.58	6.211	1.350	(211) Ta bcc
72.22	1.287	1.307	(311) Ta fcc or Ta oxide
74.04	61.44	1.279	(220) Cu
82.56	2.025	1.168	(220) Ta bcc
89.88	15.07	1.091	(311) Cu
95.12	6.806	1.044	(222) Cu

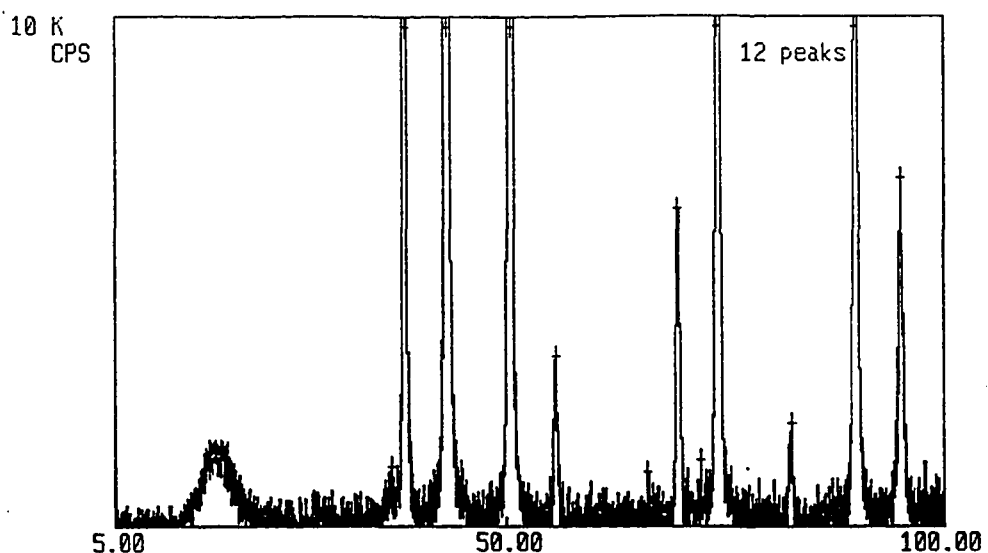


Figure 78. X-ray diffraction scan of specimen {5,2} from run 23 after heat treatment for 10 hours at 900 C.

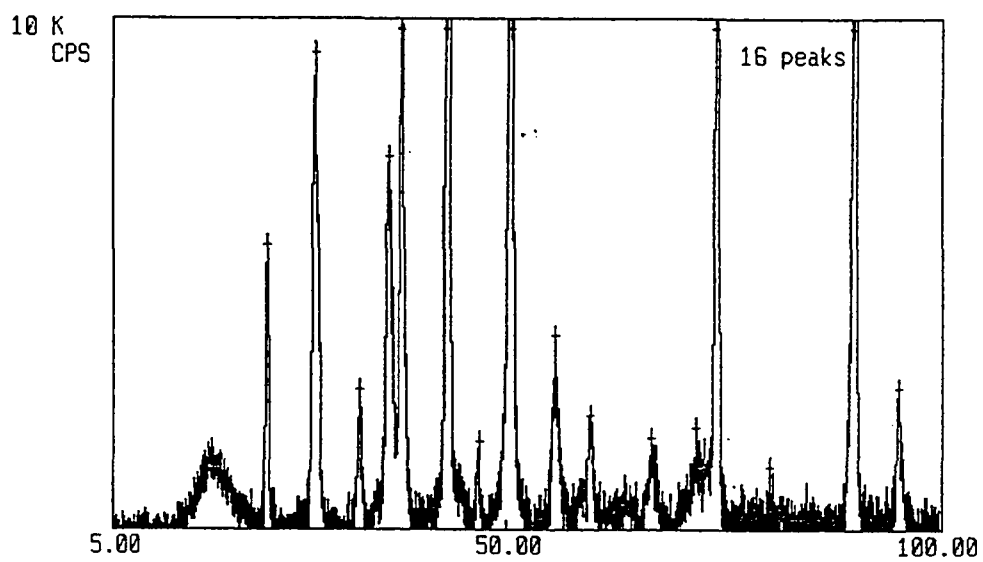


Figure 79. X-ray diffraction scan of specimen {5,6} from run 23 after heat treatment for 10 hours at 900 C.

Table 28. Table of x-ray diffraction data for specimen {5,6} from run 23 after heat treatment for 10 hours at 900 C.

<u>2θ</u>	I _{max}	d	comments
22.88	5.560	3.884	Ta oxide
28.38	9.312	3.142	Ta oxide
33.38	2.724	2.682	Ta oxide
36.78	7.289	2.442	(111) Ta fcc or Ta oxide
38.14	10.03	2.358	(110) Ta bcc or Ta oxide
43.34	78.26	2.086	(111) Cu
46.82	1.712	1.939	Ta oxide
50.42	23.64	1.808	(200) Cu
55.58	3.798	1.652	(200) Ta bcc
59.58	2.233	1.550	(220) Ta fcc or Ta oxide
66.66	1.796	1.402	Ta oxide
71.78	1.980	1.314	(311) Ta fcc or Ta oxide
74.12	14.70	1.278	(220) Cu
80.26	1.225	1.195	(220) Ta bcc or Ta oxide
90.04	32.51	1.089	(311) Cu
95.06	2.756	1.044	(222) Cu

Table 29. Table of x-ray diffraction data for specimen {2,2} from run 19 after heat treatment for 1 hour at 900 C.

<u>2θ</u>	I _{max}	d	comments
22.94	6.765	3.874	Ta oxide
28.42	7.766	3.138	Ta oxide
33.76	1.126	2.653	Ta oxide
35.34	1.796	2.538	(111) Ta fcc or Ta oxide
36.96	6.602	2.430	(111) Ta fcc or Ta oxide
38.56	3.306	2.333	(110) Ta bcc
40.98	1.314	2.201	(200) Ta fcc or Ta oxide
43.38	81.37	2.084	(111) Cu
46.76	2.048	1.941	Ta oxide
50.50	32.63	1.806	(200) Cu
55.64	3.767	1.651	(200) Ta bcc
59.08	1.337	1.562	(220) Ta fcc or Ta oxide
60.86	1.278	1.521	(220) Ta fcc or Ta oxide
67.24	1.221	1.391	Ta oxide
70.78	1.328	1.330	(311) Ta fcc or Ta oxide
74.12	13.25	1.278	(220) Cu
89.94	9.963	1.090	(311) Cu
95.10	3.400	1.044	(222) Cu

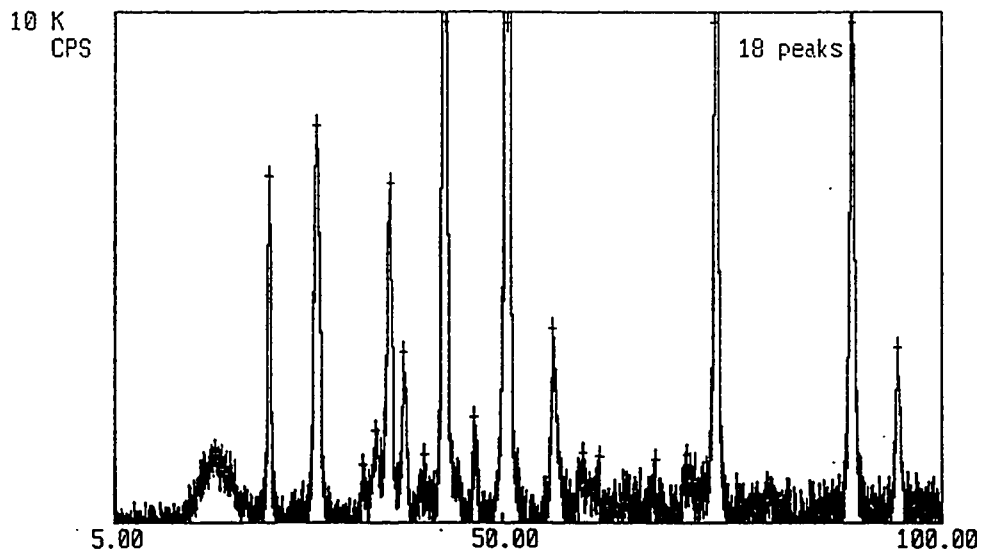


Figure 80. X-ray diffraction scan of specimen {2,2} from run 19 after heat treatment for 1 hour at 900 C.

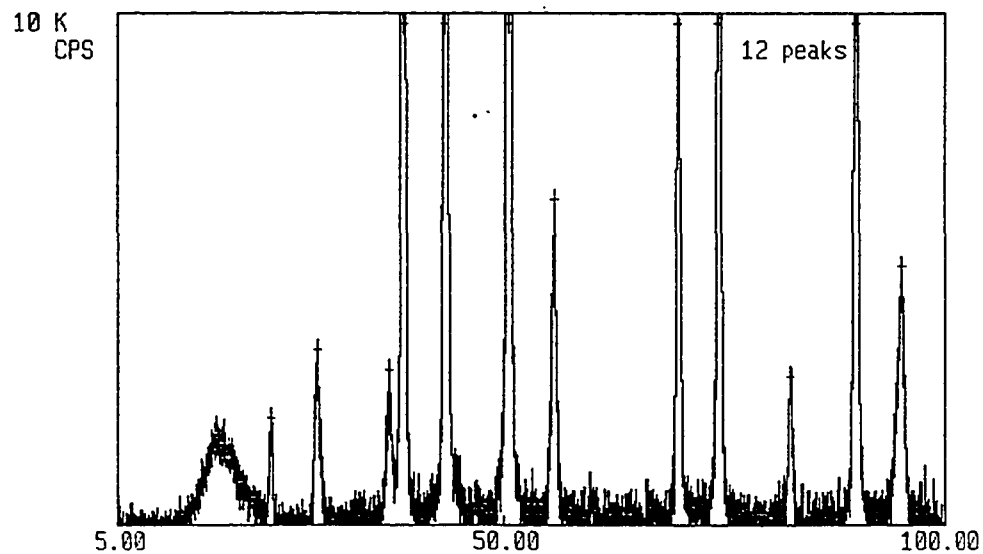


Figure 81. X-ray diffraction scan of specimen {2,2} from run 20 after heat treatment for 1 hour at 900 C.

Table 30. Table of x-ray diffraction data for specimen {2,2} from run 20 after heat treatment for 1 hour at 900 C.

<u>2θ</u>	Imax	d	comments
22.96	2.093	3.870	Ta oxide
28.42	3.422	3.138	Ta oxide
36.88	3.025	2.435	(111) Ta fcc or Ta oxide
38.52	44.36	2.335	(110) Ta bcc
43.36	88.06	2.085	(111) Cu
50.46	37.30	1.807	(200) Cu
55.54	6.340	1.653	(200) Ta bcc
69.58	9.900	1.350	(211) Ta bcc
74.08	33.22	1.279	(220) Cu
82.38	2.896	1.170	(220) Ta bcc
89.96	18.53	1.090	(311) Cu
95.10	5.041	1.044	(222) Cu

Table 31. Table of x-ray diffraction data for large grained Ta wires.

<u>2θ</u>	Imax	d	comments
34.66	1.106	2.586	Ta oxide
38.60	110.0	2.331	(110) Ta bcc
49.76	0.462	1.831	Ta oxide
55.68	14.36	1.649	(200) Ta bcc
62.08	0.340	1.494	Ta oxide
66.16	0.258	1.411	Ta oxide
69.64	381.9	1.349	(211) Ta bcc
73.14	0.433	1.293	Ta oxide
82.54	57.30	1.168	(220) Ta bcc

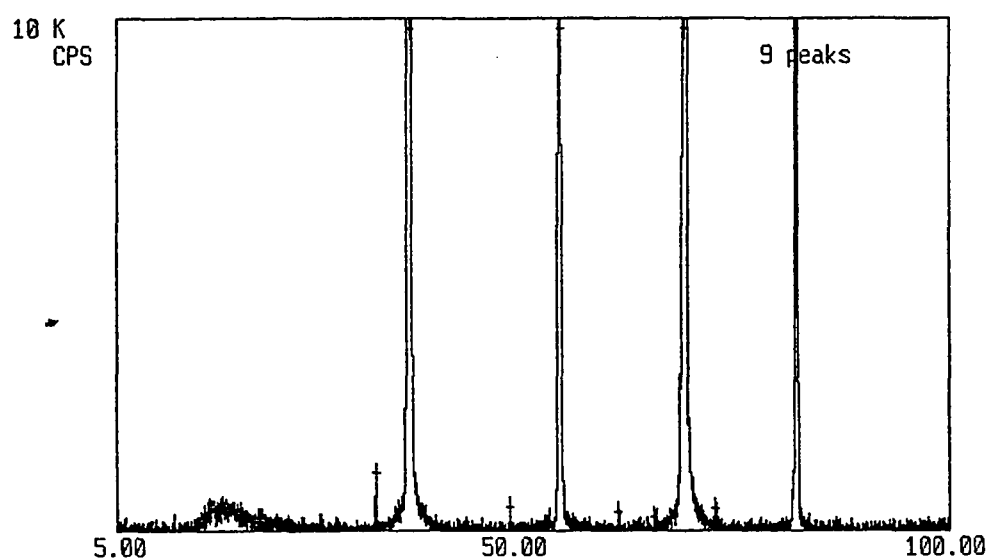


Figure 82. X-ray diffraction scan of large grained Ta wires.

POWDER FILE DATA

This appendix lists all the listed compounds and powder diffraction file numbers [90] for the Cu-Ta-O system and then lists d spacings, 2 theta values (assuming Cu k alpha 1 x-rays) and a label for the most relevant data in order of descending d spacing in table 32.

Table 32. Table of powder diffraction file numbers for Cu, Ta, and O compounds

<u>Compound</u>	<u>File number</u>
Cu ₄ O ₃	3-879
Ta (bcc)	4-788
Cu	4-836
Q ₂ O	5-661
Cu ₂ O	5-667
γ -TaO _x	15-206
γ -TaO _x	15-243
TaO	17-709
TaO ₂	19-297
δ -(Ta, O)	19-1299
α -Ta ₂ O ₅	19-1300
Ta ₂ O	18-1302
δ -Ta ₂ O ₅	18-1304
Ta ₂ O ₅	21-1198
Ta ₂ O ₅	21-1199
Ta ₂ O ₅	25-922 low temp orthorhombic
Ta (tet)	25-1280
H ₁ -Ta ₂ O ₅	27-144
Ta _{0.83} O ₂	28-1277
Ta ₂ O ₅	33-1390
Ta ₂ O ₅	33-1391
TaO	34-977
α -Ta ₂ O ₅	35-1193
Cu _{0.08} Ta ₃ O ₈	36-1208
Ta _{0.97} O ₂	37-117
Ta _{0.8} O ₂	37-118
CuTa ₁₀ O ₂₆	37-205
Cu _{1.05} Ta _{1.98} O ₆	37-896

Interplanar spacings can also be calculated using lattice parameters. The lattice parameter for bcc Ta is 3.298 angstroms [77]. The lattice parameter for fcc Cu is 3.6148 angstroms [77]. The lattice parameter for fcc Ta assuming the reverse of a 3% contraction from coordination 12 to coordination 8 is 2.9443 angstroms [77]. Experimental lattice

parameters for fcc Ta range from a low of 4.39 angstroms from Chopra and co-workers [11] to a high of 4.42 angstroms from Denbigh and Marcus [10]. Interplanar spacings for Cu, Ta, and Ta oxide are tabulated in table 33.

Table 33. Table of interplanar spacings for Cu, Ta, and Ta oxide.

d (angstroms)	2θ (degrees)	I/I100	Label
5.28	16.78	2	(140) Ta_2O_5 25-922
5.04	17.58	1	(080) Ta_2O_5 25-922
3.88	22.90	85	(001) Ta_2O_5 25-922
3.786	23.48	55	α - Ta_2O_5 35-1193
3.618	24.58	15	α - Ta_2O_5 35-1193
3.377	26.37	5	(1 10 0) Ta_2O_5 25-922
3.365	26.47	40	α - Ta_2O_5 35-1193
3.152	28.29	100	(1 11 0) Ta_2O_5 25-922
3.131	28.48	4	(141) Ta_2O_5 25-922
3.098	28.79	40	(200) Ta_2O_5 25-922
3.090	28.87	4	(210) Ta_2O_5 25-922
3.077	28.99	2	(081) Ta_2O_5 25-922
3.039	29.37	15	α - Ta_2O_5 35-1193
2.951	30.26	2	(1 12 0) Ta_2O_5 25-922
2.976	30.00	100	α - Ta_2O_5 35-1193
2.876	31.07	2	(0 14 0) Ta_2O_5 25-922
2.727	32.81	3	(270) Ta_2O_5 25-922
2.639	33.94	3	(280) Ta_2O_5 25-922
2.5519	35.14		(111) fcc Ta calculated from [10]
2.549	35.18	4	(1 10 1) Ta_2O_5 25-922
2.5346	35.38		(111) fcc Ta calculated from [11]
2.449	36.66	75	(1 11 1) Ta_2O_5 25-922
2.449	36.66	20	α - Ta_2O_5 35-1193
2.423	37.07	35	(201) Ta_2O_5 25-922
2.419	37.14	4	(211) Ta_2O_5 25-922
2.4040	37.38		(111) Ta fcc calculated from [77]
2.352	38.23	2	(1 12 1) Ta_2O_5 25-922
2.338	38.47	100	(110) Ta bcc
2.3320	38.58		(110) Ta bcc calculated from [77]
2.254	39.97	60	α - Ta_2O_5 35-1193
2.234	40.34	2	(271) Ta_2O_5 25-922
2.234	40.34	20	α - Ta_2O_5 35-1193
2.2100	40.80		(200) fcc Ta calculated from [10]
2.1950	41.09		(200) fcc Ta calculated from [11]
2.183	41.32	2	(281) Ta_2O_5 25-922
2.105	42.93	3	(1 18 0) Ta_2O_5 25-922
2.092	43.21	2	(330) Ta_2O_5 25-922

Table 33. (continued)

d (angstroms)	2θ (degrees)	I/I100	Label
2.088	43.30	100	(111) Cu
2.0870	43.32		(111) Cu calculated from [77]
2.0820	43.43		(200) Ta fcc calculated from [77]
2.030	44.60	5	(2 15 0) Ta ₂ O ₅ 25-922
2.024	44.74	6	(340) Ta ₂ O ₅ 25-922
2.007	45.14	4	(1 19 0) Ta ₂ O ₅ 25-922
2.002	45.26	4	(350) Ta ₂ O ₅ 25-922
1.953	46.46	10	α-Ta ₂ O ₅ 35-1193
1.944	46.69	25	(002) Ta ₂ O ₅ 25-922
1.894	47.99	20	α-Ta ₂ O ₅ 35-1193
1.851	49.18	3	(1 18 1) Ta ₂ O ₅ 25-922
1.844	49.38	5	α-Ta ₂ O ₅ 35-1193
1.838	49.55	5	(3 10 0) Ta ₂ O ₅ 25-922
1.832	49.73	17	(0 22 0) Ta ₂ O ₅ 25-922
1.824	49.96	3	(142) Ta ₂ O ₅ 25-922
1.808	50.43	46	(200) Cu
1.8074	50.45		(200) Cu calculated from [77]
1.807	50.46	4	(331) Ta ₂ O ₅ 25-922
1.799	50.70	18	(3 11 0) Ta ₂ O ₅ 25-922
1.796	50.79	4	(341) Ta ₂ O ₅ 25-922
1.784	51.16	3	(1 19 1) Ta ₂ O ₅ 25-922
1.780	51.28	2	(351) Ta ₂ O ₅ 25-922
1.760	51.91	3	(3 12 0) Ta ₂ O ₅ 25-922
1.6926	54.14	10	α-Ta ₂ O ₅ 35-1193
1.685	54.41	1	(1 10 2) Ta ₂ O ₅ 25-922
1.661	55.26	7	(3 10 1) Ta ₂ O ₅ 25-922
1.656	55.44	30	(0 22 1) Ta ₂ O ₅ 25-922
1.655	55.48	35	(1 11 2) Ta ₂ O ₅ 25-922
1.653	55.55	21	(200) Ta bcc
1.6494	55.68	5	α-Ta ₂ O ₅ 35-1193
1.6490	55.70		(200) Ta bcc calculated from [77]
1.647	55.77	15	(202) Ta ₂ O ₅ 25-922
1.646	55.81	9	(212) Ta ₂ O ₅ 25-922
1.633	56.29	12	(3 11 1) Ta ₂ O ₅ 25-922
1.632	56.33	8	(2 21 0) Ta ₂ O ₅ 25-922
1.624	56.63	2	(1 12 2) Ta ₂ O ₅ 25-922
1.602	57.48	2	(3 12 1) Ta ₂ O ₅ 25-922
1.6004	57.54	5	α-Ta ₂ O ₅ 35-1193
1.576	58.52	9	(2 22 0) Ta ₂ O ₅ 25-922
1.5627	59.06		(220) fcc Ta calculated from [10]
1.5521	59.51		(220) fcc Ta calculated from [11]
1.549	59.64	4	(400) Ta ₂ O ₅ 25-922
1.548	59.68	4	(410) Ta ₂ O ₅ 25-922
1.545	59.81	3	(420) Ta ₂ O ₅ 25-922

Table 33. (continued)

<u>d</u> (angstroms)	2θ (degrees)	I/I100	Label
1.504	61.61	2	(2 21 1) Ta ₂ O ₅ 25-922
1.481	62.68	3	(480) Ta ₂ O ₅ 25-922
1.480	62.73	3	(3 19 0) Ta ₂ O ₅ 25-922
1.4722	63.10		(220) Ta fcc calculated from [77]
1.464	63.49	2	(490) Ta ₂ O ₅ 25-922
1.461	63.64	10	(2 22 1) Ta ₂ O ₅ 25-922
1.445	64.43	1	(3 17 1) Ta ₂ O ₅ 25-922
1.4410	64.63	5	α-Ta ₂ O ₅ 35-1193
1.439	64.73	3	(401) Ta ₂ O ₅ 25-922
1.438	64.78	3	(411) Ta ₂ O ₅ 25-922
1.435	64.93	1	(421) Ta ₂ O ₅ 25-922
1.408	66.33	1	(332) Ta ₂ O ₅ 25-922
1.402	66.65	3	(342) Ta ₂ O ₅ 25-922
1.396	66.98	2	(471) Ta ₂ O ₅ 25-922
1.383	67.69	3	(481) Ta ₂ O ₅ 25-922
1.350	69.58	38	(211) Ta bcc
1.3464	69.79		(211) Ta bcc calculated from [77]
1.335	70.48	3	(3 10 2) Ta ₂ O ₅ 25-922
1.333	70.60	6	(0 22 0) Ta ₂ O ₅ 25-922
1.3327	70.62		(311) fcc Ta calculated from [10]
1.3236	71.18		(311) fcc Ta calculated from [11]
1.320	71.40	7	(3 11 2) Ta ₂ O ₅ 25-922
1.305	72.35	3	(3 12 2) Ta ₂ O ₅ 25-922
1.296	72.93	4	(003) Ta ₂ O ₅ 25-922
1.278	74.13	20	(220) Cu
1.2780	74.13		(220) Cu calculated from [77]
1.2759	74.27		(222) fcc Ta calculated from [10]
1.269	74.75	2	(0 30 1) Ta ₂ O ₅ 25-922
1.2673	74.86		(222) fcc Ta calculated from [11]
1.2555	75.69		(311) Ta fcc calculated
1.2020	79.71		(222) Ta fcc calculated
1.1687	82.46	13	(220) Ta bcc
1.1660	82.69		(220) Ta bcc calculated from [77]
1.1050	88.39		(400) fcc Ta calculated from [10]
1.0975	89.15		(400) fcc Ta calculated from [11]
1.0900	89.93	17	(311) Cu
1.0899	89.94		(311) Cu calculated from [77]
1.0453	94.94	19	(310) Ta bcc
1.0436	95.14	5	(222) Cu
1.0435	95.15		(222) Cu calculated from [77]
1.0429	95.22		(310) Ta bcc calculated from [77]
1.0410	95.45		(400) Ta fcc calculated from [77]

COMPUTER PROGRAMS

This appendix contains the Mathematica computer code for the programs discussed in the experimental procedure. These programs include those for composition profiles, thickness (mass) profiles, x-ray peak fitting, and composition profile maps.

The program below calculates composition profiles. The variables (real numbers) of interest are: **h** is the height of the substrate holder above the sources in cm. **ma** is the amount of component "a" evaporated. **mb** is the amount of component "b" evaporated. **words** is a list of 5 lines of text for a label and has format **words** = {"line 1 of text", "line 2 of text", "line 3 of text", "line 4 of text", "line 5 of text"}. **srca** is the position of the source of component "a". **srcb** is the position of the source of component "b". **sya** is the sputter yield of component "a" in atoms per ion. **syb** is the sputter yield of component "b" in atoms per ion. **orgrat** is the ratio of bombarding ions to depositing atoms at the center of the substrate holder; this has value zero for evaporation and greater than zero for ion assisted deposition.

TANTALUM ATOM % PROFILE

```

Clear[SputCosDepColor2Mirrortxt];
(*Warning! use only when mirror symmetry applies*)
SputCosDepColor2Mirrortxt[h_Real, ma_Real, mb_Real, words_] :=
Block[{srca = {10, 0, 0}, srcb = {-10, 0, 0}, z, sya = 0.3, syb = 0.6,
refa, refb, ref, orgrat = 0.0, valsout, outpict, label, sa, sb, ic, min,
zeros, max, i},
red[x_] := Which[0.0 <= x <= 0.20, 1.0,
0.20 <= x <= 0.40, 2 - 5 x,
0.40 <= x <= 0.80, 0.0,
0.8 <= x <= 1.0, 5 x - 4] (0.9 + 0.1 Cos[100 Pi x]);
green[x_] := Which[0.0 <= x < 0.20, 5 x,
0.20 <= x <= 0.60, 1.0,
0.60 <= x <= 0.80, 4 - 5 x,
0.80 <= x <= 1.0, 0.0] (0.9 + 0.1 Cos[100 Pi x]);
blue[x_] := Which[0.0 <= x <= 0.4, 0.0,
0.40 <= x <= 0.60, 5 x - 2,
0.60 <= x <= 1.0, 1.0] (0.9 + 0.1 Cos[100 Pi x]);
colorset = Table[RGBColor[N[red[i]], N[green[i]], N[blue[i]]],
{i, 0, 1, 0.01}];
z = h;
depa[x_, y_] := ma h h/ (Pi ((x - srca[[1]])^2 + (y - srca[[2]])^2 +
z^2)^2);
depb[x_, y_] := mb h h/ (Pi ((x - srcb[[1]])^2 + (y - srcb[[2]])^2 +
z^2)^2);
refa = depa[0.0, 0.0];
refb = depb[0.0, 0.0];

```

```

ref = refa + refb;
ic = orgrat ref;
thick[x_, y_] := check = depa[x, y] + depb[x, y];
netdep[x_, y_] := thick[x, y] - ic (sya depa[x, y] +
    syb depb[x, y])/thick[x, y];
acontent[x_, y_] := depa[x,y](1 - ic sya/thick[x, y])/netdep[x, y];
bcontent[x_, y_] := depb[x,y](1 - ic syb/thick[x, y])/netdep[x, y];
min = 1.0;
max = 0.0;
valsout = Table[c = N[acontent[i - 15.5, j-15.5]];
    Which[c < min, min = c, c > max, max = c];
    Which[ic sya/check >= 1 || ic syb/check >= 1,
        RGBColor[0.0, 0.0, 0.0],
        True, colorset[[Round[100 c] + 1]]],
    {j,15}, {i,30}];
Do[AppendTo[valsout, valsout[[16 - i]]], {i,15}];
outpict = Table[{valsout[[j,i]],
    Rectangle[{i-1,j-1}, {i,j}], {i, 30}, {j,30}};
Print["srca = ",srca, " srcb = ",srcb];
Print["sya = ",sya, " syb = ",syb];
Print["refa = ", N[refa], " refb = ", N[refb], " ref = ", N[ref]];
Print["orgrat = ", N[orgrat], " ic = ", N[ic]];
Print["the min acontent is ", min];
Print["the max acontent is ", max];
label = {Text[words[[1]], {0,43.5}, {-1,0}],
    Text[words[[2]], {0,40.5}, {-1,0}],
    Text[words[[3]], {0,37.5}, {-1,0}],
    Text[words[[4]], {0,34.5}, {-1,0}],
    Text[words[[5]], {0,31.5}, {-1,0}}];
rmin = Which[min >= 0, Round[100 min], min< 0, 0];
rmax = Which[max <= 1, Round[100 max], max > 1.0, 100];
ints = rmax - rmin + 1;
fives = Table[i, {i, 0, 100, 5}];
hgt = 42.0;
wid = 10.0;
inc = hgt/ints;
ll = {35.0, 1.5};
rect[x_] := Rectangle[{ll[[1]], ll[[2]] + x inc},
    {ll[[1]] + wid, ll[[2]] + (x + 1) inc}];
textset = {};
barsout = {};
Do[
    If[MemberQ[fives, i],
        AppendTo[textset,
            Text[i, {ll[[1]], ll[[2]] + (i - rmin) inc + inc/2},
                {1,0}]];
        AppendTo[barsout, {colorset[[i+1]], rect[i-rmin]}],
        {i, rmin, rmax}
    ];
    Show[Graphics[{outpict, label, barsout, textset},
        PlotRange->{{0,45}, {0,45}}, AspectRatio->1]]
]

```

The program below calculates thickness (mass) profiles. The variables of interest are:
h is the height of the substrate holder above the sources in cm. **ma** is the amount of component "a" evaporated. **mb** is the amount of component "b" evaporated. **words** is a list of 5 lines of text for a label and has format words = {"line 1 of text", "line 2 of text", "line 3 of text", "line 4 of text", "line 5 of text"}. **srca** is the position of the source of component "a". **srcb** is the position of the source of component "b". **sya** is the sputter yield of component "a" in atoms per ion. **syb** is the sputter yield of component "b" in atoms per ion. **orgrat** is the ratio of bombarding ions to depositing atoms at the center of the substrate holder; this has value zero for evaporation and greater than zero for ion assisted deposition.

```

Clear[SputCosDepColor1Mirrortxt];
(*Warning! use only when mirror symmetry applies*)
SputCosDepColor1Mirrortxt[h_Real, ma_Real, mb_Real, words_] :=
Block[{srca = {10, 0, 0}, srcb = {-10, 0, 0}, z, sya = 0.3, syb = 0.6,
      refa, refb, ref, orgrat = 0.4, sa, sb, ic, min, zeros, max, i},
      red[x_] := Round[1000 Which[0.0 <= x <= 0.20, 1.0,
          0.20 <= x <= 0.40, 2 - 5 x,
          0.40 <= x <= 0.80, 0.0,
          0.8 <= x <= 1.0, 5 x - 4] (0.9 + 0.1 Cos[100 Pi x])/1000];
      green[x_] := Round[1000 Which[0.0 <= x < 0.20, 5 x,
          0.20 <= x <= 0.60, 1.0,
          0.60 <= x <= 0.80, 4 - 5 x,
          0.80 <= x <= 1.0, 0.0] (0.9 + 0.1 Cos[100 Pi x])/1000];
      blue[x_] := Round[1000 Which[0.0 <= x <= 0.4, 0.0,
          0.40 <= x <= 0.60, 5 x - 2,
          0.60 <= x <= 1.0, 1.0] (0.9 + 0.1 Cos[100 Pi x])/1000];
      colorset = Table[RGBColor[N[red[i]], N[green[i]], N[blue[i]]],
      {i, 0, 1, 0.01}];
      z = h;
      depa[x_, y_] := ma h h/ (Pi ((x - srca[[1]])^2 +
          (y - srca[[2]])^2 + z^2)^2);
      depb[x_, y_] := mb h h/ (Pi ((x - srcb[[1]])^2 +
          (y - srcb[[2]])^2 + z^2)^2);
      refa = depa[0.0, 0.0];
      refb = depb[0.0, 0.0];
      ref = refa + refb;
      ic = orgrat ref;
      thick[x_, y_] := check = depa[x, y] + depb[x, y];
      netdep[x_, y_] := thick[x, y] - ic (sya depa[x, y] +
          syb depb[x, y])/thick[x, y];
      acontent[x_, y_] := depa[x,y](1 - ic sya/thick[x, y])/netdep[x, y];
      bcontent[x_, y_] := depb[x,y](1 - ic syb/thick[x, y])/netdep[x, y];
      min = 100.0;
      max = 0.0;

```

```

valsout = Table[c = Round[N[50 netdep[i - 15.5, j-15.5]/ref]];
  Which[c < min, min = c, c > max, max = c];
  Which[c < 0 || ic sya/check >= 1 || ic syb/check >= 1,
    RGBColor[0.0, 0.0, 0.0],
    0 <= c <= 100, colorset[[c + 1]],
    c > 100, RGBColor[1.0, 1.0, 1.0]], {j,15}, {i,30}];
Do[AppendTo[valsout, valsout[[16 - i]]], {i,15}];
outpict = Table[{valsout[[j,i]],
  Rectangle[{i-1,j-1}, {i,j}]}, {i, 30}, {j,30}];
Print["srcA = ",srca," srcB = ",srcb];
Print["sya = ",sya," syb = ",syb];
Print["refa = ", N[refa]," refb = ", N[refb]," ref = ", N[ref]];
Print["orgrat = ", N[orgrat]," ic = ", N[ic]];
label = {Text[words[[1]], {0,43.5}, {-1,0}],
  Text[words[[2]], {0,40.5}, {-1,0}],
  Text[words[[3]], {0,37.5}, {-1,0}],
  Text[words[[4]], {0,34.5}, {-1,0}],
  Text[words[[5]], {0,31.5}, {-1,0}}];
rmin = Which[min >= 0, min, min < 0, 0];
rmax = Which[max <= 100, max, max > 100, 100];
ints = rmax - rmin + 1;
fives = Table[i, {i, 0, 100, 5}];
scaleset = Table[i, {i, 0, 2, 0.1}];
hgt = 42.0;
wid = 10.0;
inc = hgt/ints;
ll = {35.0, 1.5};
rect[x_] := Rectangle[{ll[[1]], ll[[2]] + x inc},
  {ll[[1]] + wid, ll[[2]] + (x + 1) inc}];
textset = {};
barsout = {};
Do[
  If[MemberQ[fives, i],
    AppendTo[textset,
      Text[scaleset[[i/5 + 1]],
        {ll[[1]], ll[[2]] + (i - rmin) inc + inc/2}, {1,0}]]];
    AppendTo[barsout, {colorset[[i+1]], rect[i-rmin]}],
    {i, rmin, rmax}
  ];
  Show[Graphics[{outpict, label, barsout, textset}],
    PlotRange->{{0,45}, {0,45}}, AspectRatio->1]]
]

```

The program below fits a list of ordered pairs of points from an x-ray diffraction peak to a Gaussian curve by considering all the possible combinations of points and then displays the relevant constants and plots the fitted curve onto the data. This program functions best when the data points contain approximately equal intensity on both sides of the peak maximum. The input variables are as follows: **data** is the list of data points and has format **data = {{two theta sub-**

one, intensity sub-one}, {two theta sub-two, intensity sub-two}, etc}. name is a line of text for a label on the graph and has format name = "line of text".

```

Clear[SavageGaussFitA];
SavageGaussFitA[data_, name_] :=
Block[{},
  Id = Length[data];
  mu = 0;
  sumv = 0;
  Do[
    mu += data[[i,1]] data[[i,2]];
    sumv += data[[i,2]],
    {i, Id}
  ];
  mu = N[mu / sumv];
  Print["mu = ", N[mu]];
  sigav = 0;
  divider = 0;
  Do[
    Do[
      testval = data[[i,2]]/data[[j,2]];
      If[0.99 < testval < 1.01,
        sigav += N[Sqrt[Abs[((data[[j,1]] - mu)^2 -
          (data[[i,1]] - mu)^2)/ (2 Log[testval])]]];
      divider += 1
    ],
    {j, i-1}
  ],
  {i, 2, Id}
];
sigav = N[sigav/divider];
Print["sigma av = ", N[sigav]];
cav = 0;
twosigsq = N[2 sigav^2];
Do[
  cav += N[data[[i,2]] sigav Exp[(data[[i,1]] - mu)^2 /twosigsq]],
  {i, Id}
];
cav = N[cav/Id];
Print["average value of c is = ", N[cav]];
picture = {};
step = N[(data[[Id,1]] - data[[1,1]])/15];
place = data[[1,1]];
val[x_] := N[(cav / sigav) Exp[-((x - mu)^2)/twosigsq]];
pointsa = {};
Do[
  a = val[place];
  AppendTo[pointsa, {place, a}];
  place += step,
  {i, 16}
];

```

```

AppendTo[picture, {RGBColor[0.177, 0.150, 1.000], Line[pointsa]}];
AppendTo[picture, {RGBColor[1.000, 0.090, 0.100], Line[data]}];
Print["specimen = ", name];
Show[Graphics[picture], Axes->Automatic];
Print["data points = ", data]
]

```

The following program uses linear interpolation to calculate a contour map and superimposes it onto a schematic image of the substrate holder used for this thesis. The relevant variables are: **data** is a list of real number values with values between 1 and 100 and format **data** = {value at {3,1}, value at {5,1}, value at {1,3}, value at {3,3}, value at {5,3}, value at {7,3}, value at {1,5}, value at {3,5}, value at {5,5}, value at {7,5}, value at {3,7}, value at {5,7}}. The values of **data** must increase with increasing value of the "y" coordinate. **label** is a line of text to identify the plot that is generated and has format **label** = "line of text". The contour lines are drawn and labelled for integer values of the quantity of interest.

```

Clear[SavageComp];
SavageComp[data_, label_] :=
Block[{cords = {{3,1}, {5,1}, {1,3}, {3,3}, {5,3}, {7,3}, {1,5}, {3,5}, {5,5},
{7,5}, {3,7}, {5,7}},
ints = {{1,3}, {1,4}, {1,5}, {1,2}, {2,4}, {2,5}, {2,6}, {3,7}, {3,8}, {3,4},
{4,7}, {4,8}, {4,9}, {4,5}, {5,8}, {5,9}, {5,10}, {5,6}, {6,9}, {6,10},
{7,11}, {7,8}, {8,11}, {8,12}, {8,9}, {9,11}, {9,12}, {9,10},
{10,12}, {11,12}},
kone = 1.375 2.54, ktwo = -0.375 2.54, kthree = 1.375 2.54,
kfour = 0.375 2.54, kxtrans = -4 2.54, kytrans = -7 2.54,
metcords = {{4,1}, {2,2}, {3,2}, {4,2}, {5,2}, {6,2}, {2,3}, {4,3}, {6,3},
{1,4}, {2,4}, {4,4}, {6,4}, {7,4}, {2,5}, {4,5}, {6,5}, {2,6}, {3,6},
{4,6}, {5,6}, {6,6}, {4,7}}},
coords = {};
Do[
  xreal = N[cords[[i,1]] kone + cords[[i,2]] ktwo + kxtrans];
  yreal = N[cords[[i,2]] kthree + cords[[i,1]] kfour + kytrans];
  AppendTo[ccords,{xreal,yreal}],
{i,12}
];
metcords = {};
Do[
  xreal = N[metcords[[i,1]] kone + metcords[[i,2]] ktwo + kxtrans];
  yreal = N[metcords[[i,2]] kthree + metcords[[i,1]] kfour +
kytrans];
  AppendTo[metcoords,{xreal,yreal}],
{i,23}
];

```

```

subsout = {RGBColor[1.000, 0.514, 0.320]};
Do[
    AppendTo[subsout, Rectangle[{metcoords[[i,1]] - 1.2,
        metcoords[[i,2]] - 1.2}, {metcoords[[i,1]] + 1.2,
        metcoords[[i,2]] + 1.2}]],
{i,23}
];
AppendTo[subsout, RGBColor[0.595, 0.730, 1.000]];
Do[
    AppendTo[subsout, Rectangle[{coords[[i,1]] - 1.2,
        coords[[i,2]] - 1.2}, {coords[[i,1]] + 1.2,
        coords[[i,2]] + 1.2}]],
{i,12}
];
subslabs = {};
Do[
    Which[metcoords[[i,1]] == 6 && metcoords[[i,2]] == 6, ,
        metcoords[[i,1]] == 7 && metcoords[[i,2]] == 4, ,
        metcoords[[i,1]] == 6 && metcoords[[i,2]] == 2, ,
        True, AppendTo[subslabs,
            Text[metcoords[[i]], metcoords[[i]]]]],
{i,23}
];
Do[
    Which[cords[[i,1]] == 5 && cords[[i,2]] == 7, ,
        cords[[i,1]] == 7 && cords[[i,2]] == 5, ,
        cords[[i,1]] == 7 && cords[[i,2]] == 3, ,
        cords[[i,1]] == 5 && cords[[i,2]] == 1, ,
        True, AppendTo[subslabs, Text[cords[[i]], coords[[i]]]]],
{i,12}
];
min = Min[data];
lowline = Round[min];
If[lowline < min, lowline += 1, ];
max = Max[data];
highline = Round[max];
If[highline > max, highline -= 1, ];
lines = highline - lowline;
outpoints = Table[{}, {lines + 1}];
line = 1;
comp = lowline;
While[comp <= max,
    Do[
        cone = data[[ints[[i,1]]]];
        ctwo = data[[ints[[i,2]]]];
        If[cone <= comp <= ctwo || ctwo <= comp <= cone,
            fract = (comp - cone)/(ctwo - cone);
            xone = coords[[ints[[i,1]],1]];
            xtwo = coords[[ints[[i,2]],1]];
            delx = xtwo - xone;
            yone = coords[[ints[[i,1]],2]];
            ytwo = coords[[ints[[i,2]],2]];
            dely = ytwo - yone;
            pair = N[{xone + fract delx, yone + fract dely}]];

```

```

AppendTo[outpoints[[line]], pair],
],
{i,30}
];
line += 1;
comp += 1
];
sortset = {};
Do[AppendTo[sortset, Sort[outpoints[[i]] ]], {i,lines +1}];
outpoints = sortset;
graphout = {};
Do[AppendTo[graphout, Line[outpoints[[i]]]], {i, lines+1}];
textout = {};
Do[
AppendTo[textout, Text[N[lowline+i-1],
Last[outpoints[[i]]], {-1,0}]],
{i,lines+1}
];
pictlab = Text[label, {0, 13.5}];
Show[Graphics[{subscut, subslabs, pictlab, textout, graphout},
Axes->Automatic, AspectRatio->1,
PlotRange->{{-15,15}, {-15,15}}]]
]

```

KINETIC DATA

This appendix describes the extraction of kinetic data from the x-ray particle size data in table 3 by using equations 5 and 6. Equation 5 indicates that if the coarsening follows LSW theory, a plot of the particle radius vs. the cube root of the annealing time should be linear and the cubes of the slopes (slopes in table 34) can be used in equation 6 to calculate diffusivities if the other relevant constants are known or can be approximated. From the diffusivities at 800 and 900 C the activation energy for diffusion of Ta through the Cu process was estimated to be ~125 Kcal/mole for the biased, low Ta alloy and ~25 Kcal/mole for the other alloys. The large range of values is probably due to the scatter in the calculated particle sizes. The values are in the same order of magnitude as the activation energies for self diffusion of Cu (~50 Kcal/mole) and Ta (~100 Kcal/mole) discussed in the Background. Better estimates would require better numbers for g, D, and c in equation 6.

Table 34. SLOPES OF PARTICLE RADIUS (\AA) VS. CUBE ROOT OF ANNEALING TIME (HOURS)

T (C)	Biased Low Ta	Biased High Ta	Biased Low Ta	Biased High Ta
800	8.7 *	67	105 *	44 *
900	48	89 *	149	62

* indicates poor linear fit.

REFERENCES

1. L. G. Fritzemeier, "High-Conductivity Ultrafine Microcomposites, Final Report", Rocketdyne Report No. RI/RD 90-169
2. Robert C. Weast, editor, CRC Handbook of Chemistry and Physics, 58th edition, CRC Press, West Palm Beach, 1978.
3. Metals Handbook Ninth Edition, Volume 2 Properties and Selection: Nonferrous Alloys and Pure Metals, American Society for Metals, Metals Park, 1979.
4. R. M. Brick, A. W. Pense, and R. B. Gordon, Structure and Properties of Engineering Materials, McGraw-Hill, New York, 1977.
5. E. G. West, Copper and It's Alloys, John Wiley & Sons, New York, 1982.
6. H. Jehn and E. Olzi, "High Temperature Solid-Solubility Limit and Phase Studies in the System Tantalum-Oxygen", J. Less Common Metals, vol. 27, 1972.
7. N. Terao, "Structure des Oxides de Tantale", Jap. J. Appl. Phys., Vol. 6 No. 1, January, 1967, pgs 21-34.
8. D. B. Butrymowicz, J. R. Manning, and M. R. Read, Diffusion Rate Data and Mass Transport Phenomena for Copper Systems, National Bureau of Standards, Washington, D. C., 1977.
9. W. A. Jesser and J. W. Matthews, "Evidence for Pseudomorphic Growth of Iron on Copper", Phil. Mag., 15, 1097 (1967).
10. P. N. Denbigh and R. B. Marcus, "Structure of Very Thin Tantalum and Molybdenum Films", J. Appl. Phys., vol. 37, no. 12, Nov. 1966.
11. K. L. Chopra, M. R. Randlett, and R. H. Duff, "Face-centred Cubic Modification in Sputtered Films of Tantalum, Molybdenum, Tungsten, Rhenium, Hafnium, and Zirconium", Phil. Mag., 16, 261 (1967).
12. J. Bevk and W. A. Sunder, "Mechanical Properties of Cu-Based Composites with In Situ Formed Ultrafine Filaments", IN SITU COMPOSITES IV, F. D. Lemkey, H. E. Cline, and M. McLean, editors, Elsevier, 1982.
13. C. Zener(1948): see C. S. Smith, Trans. AIME, vol. 175, p47, 1948.
14. Metals Handbook Ninth Edition, Volume 7 Powder Metallurgy, American Society for Metals, Metals Park, 1984.
15. K. R. Anderson, "The Properties of Oxide Dispersed and Spinodally Strengthened Copper Alloys Following High Temperature Neutron Environment Exposure, Ph. D. thesis, University of Illinois at Urbana-Champaign, 1990
16. L. J. Westfall, and D. W. Petrasek, "Fabrication and Preliminary Evaluation of Tungsten Fiber Reinforced Copper Composite Combustion Chamber Liners", NASA Technical Memorandum 100845, May 1988.

17. National Materials Advisory Board Committee on Materials with Submicron-sized Microstructures, "Research Opportunities for Materials with Ultrafine Microstructures", NMAB-454, National Academy Press, 1989.
18. S. K. Ganapathi, M. Aindow, H. L. Fraser and D. A. Rigney, "A Comparative Study of the Nanocrystalline Material Produced by Sliding Wear and Inert Gas Condensation", MRS, Fall 1990, Draft.
19. D. M. Mattox, "Film Deposition Using Accelerated Ions", Electrochemical Technology, Vol. 2, No. 9-10 Sept.-Oct. 1964.
20. H. S. Savage, "Structure and Properties of Ion Plated Aluminum Coatings", M. S. Thesis, UIUC 1988.
21. P. A. Scott, "Analysis of Ion Plated Cu/Cordierite Film and Interface Structure and Chemistry", M. S. Thesis, UIUC 1987.
22. D. M. Leet, Microstructural and Interface Studies of Evaporated and Ion Plated Titanium Coatings", M. S. Thesis, UIUC, 1985.
23. D. M. Mattox, "Fundamentals of Ion Plating", J. Vac. Sci. Tech., 10 (1), 1973.
24. B. N. Chapman, Glow Discharge Processes, John Wiley & Sons, New York, 1980.
25. J. A. Thornton, "Physical Vapor Deposition" in Semiconductor Materials and Process Technologies, ed. by G. E. McGuire, Noyes, 1984.
26. S. M. Shin, "The Growth of Cu-Cr Metastable Alloys by Bias Sputtering: Effect of Substrate Bias and Alloy Composition on Solubility and Morphology", Ph. D. Thesis in Metallurgical Engineering, UIUC, 1987.
27. R. Bland, et al., "Effect of Ion Bombardment During Deposition on Thick Metal and Ceramic Deposits", J. Vac. Sci. Tech., 11 (1), 671, 1974.
28. M. Lardon, et al., "Morphology of Ion-Plated Titanium and Aluminum Films Deposited at Various Substrate Temperatures", Thin Solid Films, 54, 317, 1978.
29. D. Teer and B. Delcea, "Grain Structure of Ion Plated Coatings", Thin Solid Films, 54, 295, 1978.
30. E. Hirsch and I. Varga, "Thin Film Annealing by Ion Bombardment", Thin Solid Films, 69, 99, 1980.
31. C. Egert and D. Scott, "A Study of Ion Plating Parameters, Coating Structure, and Corrosion Protection for Aluminum Coatings on Uranium", J. Vac. Sci. Tech. A, 5(4), Jul/Aug, 1987.
32. M. Lardon, et al., "Morphology of Ion-Plated Titanium and Aluminum Films Deposited at Various Substrate Temperatures", Thin Solid Films, 54, 317, 1978.
33. T. J. Garosshen, et al., "Aluminum Metallization Technology for Semiconductor Devices", J. of Metals, May, 1985.

34. A. G. Dirks and H. J. Leamy, "Columnar Microstructure in Vapor-Deposited Thin Films", *Thin Solid Films*, 47, 219, 1977.
35. R. Glang, Chapter1 in Handbook of Thin Film Technology, ed by L. Maissel, and R. Glang, McGraw-Hill, 1983.
36. A. Pargellis, "Distribution of Copper Deposited inside Holes by Sputtering", *J. Vac. Sci. Tech. A*, 5 (6), Nov/Dec, 1987.
37. R. Bunshah, ed., Deposition Technologies for Films and Coatings, Noyes, Park Ridge, 1982.
38. A. Bessaoudou, J. Machet, and C. Weissmantel., "Transport of Evaporated Material Through Support Gas in Conjunction with Ion Plating: I", *Thin Solid Films*, 149, 225, 1987.
39. A. Bessaoudou, J. Machet, and C. Weissmantel., "Transport of Evaporated Material Through Support Gas in Conjunction with Ion Plating: II", *Thin Solid Films*, 149, 237, 1987.
40. G. E. Dieter, Mechanical Metallurgy, second edition, McGraw-Hill, New York, 1976.
41. R. E. Reed-Hill, Physical Metallurgy Principles, 2nd Edition, Litton, 1973.
42. A. J. Ardell, "Precipitation Hardening", *Met. Trans. A*, 16A, Dec 1985.
43. Che-Yu Li and R. A. Oriani, "Some Considerations on the Stability of Dispersed Systems", *Met. Soc. Conf.*, vol 47, Gordon and Breach, 1968.
44. U. F. Kocks, "Kinetics of Solution Hardening", *Met. Trans. A*, 16A, Dec 1985.
45. Doris Kuhlmann-Wilsdorf, "Theory of Workhardening 1934-1984", *Met. Trans. A*, 16A, Dec 1985.
46. Niels Hansen, "Polycrystalline Strengthening", *Met. Trans. A*, 16A, Dec 1985.
47. J. D. Embury, "Plastic Flow in Dispersion Hardened Materials", *Met. Trans. A*, 16A, Dec 1985.
48. J. D. Verhoeven, Fundamentals of Physical Metallurgy, John Wiley, 1975.
49. H. Hu and B. B. Rath, *Met. Trans. 1*, 3181, 1970.
50. T. Gladman, "On the Theory of the Effect of Precipitate Particles on Grain Growth in Metals", *Proc. Roy. Soc.*, vol. 294A, p. 298, 1966.
51. W. Ostwald, "Uber die vermeintliche Isomerie des roten gelben Quecksilberoxyds und die Oberflächenspannung fester Körper", (in german), *Z. Phys. Chem.*, 34, 1900.
52. I. M. Lifshitz and V. V. Slyozov, "The Kinetics of Precipitation from Supersaturated Solid Solutions", *J. Phys. Chem. Solids*, 19, 1961.
53. C. Wagner, "Theorie der Alterung von Niederschlägen durch Umlösen", in German, *Z. Elektrochemie*, Vol. 65, pgs. 581-591, 1961

54. T. H. Courtney, "Kinetics and Mechanisms of Coarsening", AIME, Proceedings of an International Conference on Solid->Solid Phase Transformations held at Carnegie-Mellon University, Pittsburgh, PA, Aug. 10-14, 1981.
55. P. W. Voorhees, "The Theory of Ostwald Ripening", J. Stat. Phys., vol. 38, 1/2, 1985.
56. G. W. Greenwood, "Particle Coarsening", in The Mechanism of Phase Transformations in Crystalline Solids, Monograph and Report Series No. 33, The Institute of Metals, London, 1969.
57. A. J. Ardell, "Experimental Confirmation of the Lifshitz-Wagner Theory of Particle Coarsening", in The Mechanism of Phase Transformations in Crystalline Solids, Monograph and Report Series No. 33, The Institute of Metals, London, 1969.
58. S. I. Kwun and M. E. Fine, "Coarsening Rate of Beta Precipitates in Al-11Mg Alloy", Met. Trans. A, volume 16A, May 1985.
59. I. M. Lifshitz and V. V. Slyozov, "Kinetics of the Diffusional Decay of Supersaturated Solid Solutions", in Russian, Zh. Eksp. Teor. Fiz. Vol. 35, 2(8), 1958.
60. L. C. Brown, "A New Examination of Classical Coarsening Theory", Acta Metall. Vol. 37, No. 1, pp71-77, 1989.
61. D. G. Morris and M. A. Morris, "Rapid Solidification and Mechanical Alloying Techniques Applied to Cu-Cr Alloys", Mat. Sci. Eng., A104 (1988) 201-213.
62. M. A. Morris and D. G. Morris, "Microstructures and Mechanical Properties of Rapidly Solidified Cu-Cr Alloys", Acta Met. Vol. 35, No. 10, pp. 2511-2522, 1987.
63. Che-Yu Li and R. A. Oriani, "Some Considerations on the Stability of Dispersed Systems", Second Bolton Landing Conference, June 27-29, 1966, Metallurgical Society Conferences, Gordon and Breach, Volume 47, New York, 1968.
64. A. D. Brailsford and P. Wynblatt, Acta. Met. 20:489 (1979).
65. J. A. Marquesee and John Ross, J. Chem. Phys. 64:4551 (1976).
66. M. Tokuyama and K. Kawasaki, Physica 123A:386 (1984).
67. G. K. L. Davies, P. Nash and R. N. Stevens, Acta Met. 28, 179, (1980).
68. W. C. Johnson, P. W. Voorhees, and D. E Zupon, "The Effects of Elastic Stress on the Kinetics of Ostwald Ripening: The Two-Particle Problem", Met. Trans. A, vol. 20A, July 1989.
69. L. A. Bendersky, P. W. Voorhees, W. J. Boettinger, and W. C. Johnson, "The Role of Elastic Energy in the Morphological Development of a Ni-Ti-Al Alloy", Scr. Met. vol. 22, 1988.
70. W. C. Johnson, M. B. Berkenpas, and D. E. Laughlin, "Precipitat Shape Transitions During Coarsening Under Uniaxial Stress", Acta Met., vol 36, no. 12, 1988.
71. W. C. Johnson and P. W. Voorhees, "On the Classification of Phase Transitions Involving Changes in Composition", Acta Met., vol.38, no. 6, 1990.

72. M. J. Kaufman, P. W. Voorhees, W. C. Johnson, and F. S. Biancaniello, "An Elastically Induced Morphological Instability of a Misfitting Precipitate", Met. Trans. A, vol. 20A, Oct., 1989.
73. W. C. Johnson, T. A. Abinandanan, and P. W. Voorhees, "The Coarsening Kinetics of Two Misfitting Particles in an Anisotropic Crystal", Acta Met. Mater., vol. 38, no. 7, 1990.
74. R. W. Balluffi, "Grain Boundary Diffusion Mechanisms in Metals", Met. Trans. A, vol 13A, Dec. 1982.
75. H. B. Huntington, and A. R. Grone, "Current-Induced Marker Motion in Gold Wires", J. Phys. Chem. Solids, 20, 76, 1961.
76. S. Wolfram, Mathematica, Addison-Wesley, Redwood City, CA, 1988.
77. B. D. Cullity, Elements of X-Ray Diffraction, 2nd ed., Addison-Wesley, Reading, 1978.
78. Z. Nishiyama, Sci. Rept. Tohoku Univ. Vol. 23, 368, 1934.
79. G. Wasserman, Arch. Eisenhuttenwesen, Vol. 16, 647, 1933.
80. G. V. Kurdjumov and G. Sachs, Z. Physik, vol. 64, 325, 1938.
81. Thermophysical Properties of High Temperature Solid Materials, Y. S. Touloukian, ed., MacMillan, New York, 1967.
82. E. Batawi and D. G. Morris, "Dispersoid Stability in a Rapidly Solidified Cu-YB6 Alloy", Scr. Met. Vol. 23, pp. 1461-1466, 1989.
83. D. G. Morris, E. Batawi, and M. A. Morris, "Structural Instability in Rapidly-Solidified Copper-Boron Based Alloys on Heat Treating", Int. J. Rapid Solidification, 1989, Vol. 4, pp. 219-229.
84. P. G. Shewmon, Diffusion in Solids, J. Williams Book Co., Jenks, OK, 1983.
85. J. Hudson and R. HOffmah, Trans. Aime, 221: 761 (1961).
86. B. Movchan and A. Demchishin, "Study of the Structure and Properties of Thick Vacuum Condensates of Nickel, Titanium, Tungsten, Aluminum Oxide and Zirconium Dioxide", Phys. Met. Metallogr., 28, 83, (1969).
87. Metals Handbook Ninth Edition, Volume 7 Powder Metallurgy, American Society for Metals, Metals Park, 1984.
88. K. Aust and J. W. Ruter, "Grain Boundary Migration in High-Purity Lead and Dilute Lead-Tin Alloys", Trans. TMS AIME, Vol. 215, Feb. 1959, 119-127.
89. J. M. Rigsbee, "Inhibition of the Martensitic Transformation of Small Austenite Particles in Low-Alloy Steel," Proceedings of the International Conference on Martensitic Transformations ICOMAT 1979, MIT, Cambridge, MA, pp. 381-385 (1980).
90. Powder Diffraction File Search Manual, JCPDS, JCPDS International Centre for Diffraction Data, Swarthmore, 1982.

VITA

Howard Scott Savage was born in Joliet, Illinois on July 2, 1962. He graduated with a Bachelor of Science degree in Metallurgical Engineering from the University of Illinois at Urbana-Champaign in May of 1984. Mr. Savage entered the Graduate School in the Department of Metallurgical Engineering at the University of Illinois at Urbana-Champaign in January of 1984 and has held a research assistantship in the department since then. Mr. Savage completed his Master of Science in Metallurgical Engineering in October of 1988. Mr. Savage is a member of the American Vacuum Society and is a Joint Student Member in the American Society for Metals, and The Metallurgical Society of AIME.